The impacts of Spray Drying on the polymorphism of pharmaceutical and organic compounds

Grace Baaklini

Normandie Université

THESE

Pour obtenir le grade de Docteur

opéré par l'Université de Rouen

Spécialité Chimie

Les effets du Spray Drying sur le polymorphisme des composés pharmaceutiques et organiques

The impacts of Spray Drying on the polymorphism of pharmaceutical and organic compounds

Présentée et soutenue publiquement par

Grace BAAKLINI

Thèse soutenue publiquement le 16 décembre 2015 devant le jury composé de		
M. Pascal CARDINAËL	Professeur, Université de Rouen	Président
M. François GOUTENOIRE	Professeur, Université du Maine	Rapporteur
M. Jean-François WILLART	Directeur de recherche, Université Lille 1	Rapporteur
M. Massimiliano FORCATO	PhD, ZACH system	Examinateur
M. Gérard COQUEREL	Professeur, Université de Rouen	Directeur de thèse

Thèse dirigée par Pr. Dr. Gérard COQUEREL Laboratoire Sciences et Méthodes Séparatives (SMS)

UNIVERSITÉ DE ROUEN

SPMii ECOLE DOCTORALE

SMS Sciences et Méthodes Séparatives

Abstract

The impacts of Spray Drying on the polymorphism of organic and pharmaceutical compounds have been investigated with the following compounds: pyrazinamide, olanzapine, 1,3-dimethylurea and N-methylurea. The experiments carried out by Spray Drying highlighted the flexibility of this crystallization technique to access to metastable forms.

Co-spray drying tests of pyrazinamide with several excipients allowed to bring out the feature of two excipients on the crystallization of the active ingredient:

- A polymer (polyvinylpyrrolidone) has enabled the crystallization of the δ form pyrazinamide.
- 1,3-dimethylurea (Form I) blocked the transition of the γ form of pyrazinamide to other polymorphic stable forms for two years of storage at room temperature. A surface action has been proposed to explain this fact.

This work also presents the phase diagram between 1,3-dimethylurea and water in which several invariants including: metatectic, peritectic and stable and metastable eutectics are detected.

Melt-quenching applied to the N-methylurea serves to characterize two new polymorphic forms at low temperatures, with a similarity in : the space group, the asymmetric unit and intermolecular bonds. A first order mechanism governed by cooperative shear movement was proposed to explain the good reversibility between these two forms despite the low diffusion at low temperatures (≈ -120 °C).

Keywords: Spray Drying, polymorphism, Pyrazinamide, 1,3-dimethylurea, phase diagrams.

Résumé

Les effets du Spray Drying sur le polymorphisme des composés organiques et pharmaceutiques ont été étudiés avec les composés suivant: la pyrazinamide, l'olanzapine, la 1,3-diméthylurée et la N-méthylurée. Les essais menés ont mis en avant la grande flexibilité de cette technique de cristallisation, basée sur le principe d'atomisation-séchage, d'accéder à des formes métastables.

Des essais de co-spray drying de la pyrazinamide avec plusieurs excipients ont permis de mettre en évidence la particuliarité de deux excipients sur la cristallisation de ce principe actif :

- Un polymère (le polyvinylpyrrolidone) a permis la cristallisation de la forme δ de la pyrazinamide.
- La 1,3-diméthylurée (Forme I) a bloqué la transition de la forme γ de pyrazinamide vers d'autres formes polymorphiques stables pendant deux ans de stockage à température ambiante. Une action de surface a été proposée pour expliquer ce fait.

Ce travail présente également le diagramme de phase entre la 1,3-diméthylurée et l'eau mettant en
évidence la présence d'invariants : métatectique, péritectique, eutectiques (stable et métastable).

La fusion trempe appliquée sur la N-méthylurée a permis de caractériser deux nouvelles formes polymorphiques à basses températures, présentant une similitude quant au : groupe d'espace, l'unité asymétrique et les liaisons intermoléculaires. Un mécanisme de premier ordre montrant un mouvement de cisaillement est proposé expliquant la bonne réversibilité entre ces deux formes malgré la faible diffusion aux basses températures (≈ -120°C).

Mots-clés : Spray Drying, polymorphisme, Pyrazinamide, 1,3-dimethylurea, diagrammes de phases.

Table of contents

INTRODUCTION

One of the biggest challenges in the field of crystallization of pharmaceuticals is to be able to control polymorphism. In fact, many problems can arise during crystallization and can alter the physico-chemical properties of the compounds exhibiting polymorphism.
During their productions and/or storages, a large proportion of active pharmaceutical ingredients (APIs) or organic compounds, are susceptible to phase transformations or to recrystallization in the case of amorphous materials. For this reason, an extensive knowledge is required about their stability domains, access by various crystallization-filtration drying processes and conditions of storage.

In this context, various possibilities of co-spray drying of an API, named Pyrazinamide, exhibiting polymorphism with different organic partners is illustrated in chapter II of this thesis.

During the storage or the production process, solids are always in contact with gaseous phase. If the compound exhibits a strong affinity with water in the atmosphere, this contact can give rise to dramatic effects resulting in the alteration of the quality and the physical properties of the powder. For this reason, exploring and understanding heterogeneous equilibria between a compound and gaseous water is essential for the development of an API. In this regard, this thesis deals with a case study of a molecule named 1,3-dimethylurea in chapter III.

Melt crystallization is a technique used for purification. Hence, during the crystallization from the molten liquid, the molecules can crystallize in new arrangements structures resulting in amorphous materials or new polymorphic forms. This technique has been applied to a compound named N-methylurea where relevant results are obtained and discussed in chapter IV.

The thermodynamically stable polymorph is used in the most commercial dosage forms. However, APIs with low solubility in water have an insufficient bioavailability. For this reason, the necessity to develop metastable polymorphs can be an alternative solution. In this context, the access of metastable form of an API named Olanzapine has been investigated by different processes including Spray Drying illustrated in chapter V.

Chapter I

Generalities

I.1 Classification of solids

The three states of matter are solid, liquid and gas. Solid state differs from the other states of matter by the arrangement of molecules and atoms that are tightly packed together and by the strong forces between the particles that remain in a relatively fixed position. Based on the order of molecular packing, solids can be classified into two categories: amorphous or crystalline.

I.1.1 Amorphous solids

An amorphous state is a liquid-like state that exhibits a viscosity. Amorphous solids are characterized by the absence of long-range molecular order and the excess of free enthalpy compared to that of the corresponding crystalline solids [1,2]. As a result of their high energy, amorphous solids tend to crystallize spontaneously. The recrystallization of amorphous solids depends on their glass transition temperature (labelled T_g) which is the physical boundary between the supercooled liquid state and the glassy state. In this regard, when the amorphous solid is stored below its T_g, the molecular mobility is limited and the chance of recrystallization is low. In contrast, when the sample is re-heated to the T_g, the molecular mobility can be high enough to induce recrystallization.

Consequences of amorphous solids in pharmaceuticals

These disordered systems provide advantages in pharmaceutical applications since they exhibit higher dissolution rates [3,4] and bioavailability [5] compared to their crystalline counterparts. Thus, drug formulators would rather select amorphous materials as a final drug substance for pharmaceutical development taking into account their T_g value that should be relatively high to avoid recrystallization issues.

However, these disordered systems also provide some drawbacks: an amorphous solid is considered as an out-of-equilibrium state due to its internal energy storage, consequently it can release its energy excess completely through crystallization associated with $\Delta G < 0$ and return to crystallized matter. Besides, getting access to amorphous materials involves processes with a lot of energy (*e.g* high energy milling) which can result in the chemical degradation of the compound [6].

I.1.2 Crystalline solids

Crystalline solids are long-range-ordered structures obtained through a self-assembly process starting from a disordered state such as a liquid or a gas. Crystalline solids can be further subdivided into polymorphs, hydrates and solvates.

I.1.2.1 Polymorphs

Polymorphism (Greek: *poly* = many, *morphos* = form) is defined as the ability of a substance to crystallize in two or more crystalline phases (denoted as polymorphs) that have different arrangements of the molecules while retaining the same chemical composition [7,8].

Polymorphism concept was introduced for the first time by Martin Heinrich Klaproth in 1788 with the calcium carbonate compound that crystallizes in three different forms: vaterite, aragonite and calcite. The first definition of polymorphism is credited to Mitscherlich (1822), who identified different crystalline forms of sodium phosphate.

Each polymorph has its own domain of stability over temperature and pressure. The change of the temperature or the pressure can induce a modification in the crystal structure. Thus, the structural rearrangement is assigned to a polymorphic transition that can be reversible (enantiotropy) or irreversible (monotropy) in isobaric conditions. Therefore, two polymorphs can be enantropically or monotropically related.

In the enantiotropic system, two forms (a low temperature form and a high temperature form) have their own domain of thermodynamic stability. The two domains are separated by a reversible solid-solid transition temperature located below the melting point. Accordingly, below the defined solid-solid transition temperature, the low temperature form has the lowest free enthalpy (labelled G) compared to that of the high temperature form. Consequently, the low temperature form will be stable in this temperature range. Above the transition temperature, the low temperature form transforms towards the high temperature form.

The monotropic system is characterized by one form that is stable all over temperature ranges. The other form has no stability domain and is considered as metastable. This system exhibits an irreversible solid-solid transition temperature that is kinetically dependent. Upon heating the metastable form, one of the two cases can be observed: a solid-solid transition towards the stable form or the melting of the metastable form followed/or not by a recrystallization and the melting of the stable form respectively.

The relative stability of polymorphic forms in monotropic and enantiotropic systems was discussed by Burger [9] and is illustrated in diagrams in Figure I.1.

Important rules concerning the relative stability of different polymorphic forms were elaborated by Burger and Ramberger [10]. One of these rules stated that if the higher melting

form has the lower heat of fusion, the two forms are enantiotropically related, otherwise they are monotropically related.

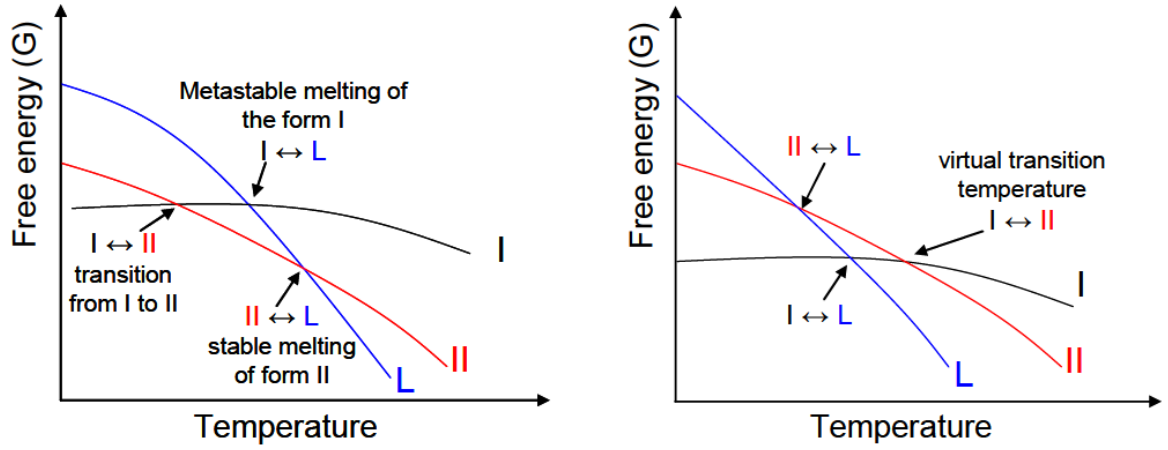

Figure I.1 Isobaric diagrams of the free enthalpy as a function of the temperature for the two polymorphic forms I and II. On the left, an enantiotropic system; on the right, a monotropic system.

Impact of polymorphism on the properties of pharmaceuticals

Polymorphism is very common in pharmaceuticals: approximately 90% of marketed drug substances are small organic molecules with a molecular weight less than 600 g/mol, and at least half of them exhibit polymorphism [(11)]. The awareness of polymorphism in pharmaceuticals has started after the accidental revelation of a new polymorph of Ritonavir® that exhibits a therapeutic property different from the commercial form [(12)]. Afterwards, there has been widespread agreement on the importance of the identification of the solid-state forms of a drug and the determination of the stability relationship between the different polymorphs before marketing any new active pharmaceutical ingredient (API) solid phase. In fact, studies have proven that two polymorphs exhibit different features [(13,14,15)] in terms of thermodynamic properties (including solubility, melting temperature), kinetic properties (including stability, dissolution rate), mechanical properties (including hardness, compactibility), surface properties (including crystal habit, surface free energy). Since polymorphs have different crystal lattices thus different lattice energies, their stability will be altered as well as their bioavailability [(16)].

I.1.2.2 Solvates and hydrates

A solvate is a compound in which solvent molecules are located in one or several crystallographic site(s). It is called hydrate when the solvent molecules are water.

Solvates are considered as intermediate compounds and they can also exhibit polymorphism[17]. Solvates and hydrates can be classified as either stoichiometric (with a well-defined constant ratio water/host *e.g* theophylline monohydrate[18]) or non-stoichiometric (with a continuously variable ratio water/ host *e.g* Crystalline β-cyclodextrin hydrate is non-stoichiometric with 10.5–12 waters per cyclodextrin molecule [19]).

A water molecule can easily get incorporated into a crystalline structure because of its small size and multidirectional hydrogen bonding capability.

A classification system for organic hydrates has been suggested [20]:

Class I are the isolated site hydrates, where water molecules are located at well-defined and isolated crystallographic sites. Most of the hydrates of this class are stoichiometric.

Class II are channel hydrates or planar hydrates where water molecules are included in the crystal next to each other, forming either channels or planar networks. Hydrates of this class are generally non-stoichiometric.

Class III are ion coordinated hydrates. Hydrates of this class can be either stoichiometric or non-stoichiometric.

Pharmaceutical consequences of hydrate and solvate formation

Pharmaceuticals can interact with water during crystallization or upon storage under a wet atmosphere. This interaction may result in hydrated forms (or solvated forms in the case of interaction with solvents). Approximately 1/3 of pharmaceutical molecules are thought to be capable of forming crystalline hydrates [21]. This is of particular relevance because the hydrated/solvated and anhydrous forms of a drug can have melting points and solubility sufficiently different to affect their pharmaceutical behavior [22,23]. Usually anhydrous forms exhibit higher solubility than the solvated materials.

The relative humidity in the atmosphere, storage temperature and drying under different pressures (*e.g* vacuum) are parameters that are involved in the departure of solvent or water molecules from the crystal structure. Consequently, the anhydrous forms obtained after desolvation can give rise to a new crystal structure [24].

I.2 How to get access to new polymorphic forms and amorphous materials?

Several methods including crystallization from solution, melt-crystallization, high energy milling, sublimation, desolvation, confinement and spray drying, are known to crystallize new polymorphic forms or getting access to amorphous materials. In this section, an overview of each method will be presented.

I.2.1 Crystallization from solution

Crystallization from solution is consisted of three steps including supersaturation, nucleation and crystal growth.

I.2.1.1 Supersaturation

The crystallization of a compound A from a solution occurs if there is a driving force that transfers the system to a supersaturated state**.** Supersaturation[25] occurs when the concentration of the compound A (namely C_A) in the solution is higher than the maximum concentration of compound A that can be dissolved in a solvent S at a given temperature defined as the solubility (C_s).

The supersaturation ratio β is defined as:

$$\beta = C_A/C_S$$

If $\beta<1$, the system is undersaturated, thus the crystals will dissolve.

If $\beta=1$ the system is saturated: $C_S= C_A$.

If $\beta>1$ the system is supersaturated, thus the crystals will grow.

In practice, an undersaturated solution reaches a supersaturated state by cooling in standard systems (where the solubility increases with temperature) or heating in retrograde systems, evaporating the solvent, changing the ionic force or pH or adding an anti-solvent.

I.2.1.2 Nucleation

An understanding of nucleation can be gained with the classical nucleation theory (CNT) originally introduced by Gibbs [26,27]. There is always a competition between the free energy ΔG_v involved in creating the volume of the nucleus (negative) and the free energy ΔG_s referring to the nucleus - solution interface energy (positive).

The formation of a nucleus, supposed to be spherical (radius r) requires a variation in the free energy called nucleation free energy $\Delta G_{nucleation}$ defined as:

$\Delta G_{nucleation} = \Delta G_v + \Delta G_s$

$\Delta G_{nucleation} = -4/3\ \Pi r^3 \Delta g_v + 4\ \Pi r^2\ \gamma$

where

k is Bolzmann constant ($1.38\ 10^{-23}$ $J.K^{-1}$) ; γ is the surface tension of the nucleus.
Δg_v is Gibbs free energy variation per unit of volume ; β is supersaturation ratio

The green line in Figure I.2 illustrates the evolution of $\Delta G_{nucleation}$ as function of the nucleus radius in case of homogenous nucleation.

ΔG^* is considered as an energy barrier that nuclei must overcome to grow.

$\Delta G_{nucleation}$ reaches a maximum value (ΔG^*) when the nucleus reaches a critical radius (labelled r*).

Accordingly, if the energy brought to the nuclei is below ΔG^*, the size is below the critical radius size ($r<r^*$), the nuclei won't be stable, thus it will dissolve.

If $\Delta G=\Delta G^*$, the critical radius is reached ($r=r^*$) so the nucleus is stable.

Finally, if the energy brought to the system is above ΔG^* ($\Delta G>\Delta G^*$), the growth is expected ($r>r^*$).

In the CNT, r* and ΔG^* can be derived as following:

$$r^* = \frac{2\gamma}{\Delta g_v}$$

$$\Delta G^* = \frac{16\ \Pi \gamma^3}{3\ (\Delta g_v)^2}$$

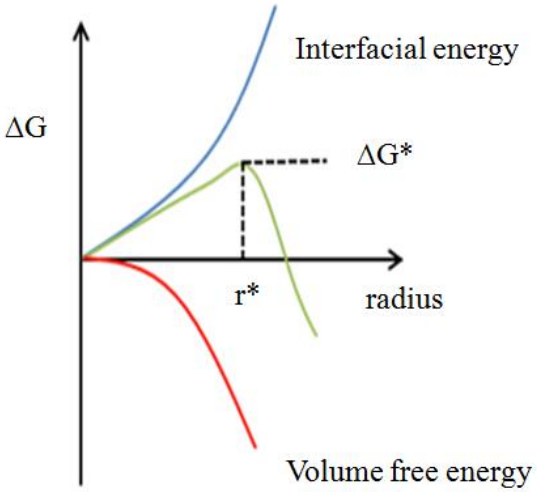

Figure I.2 The free energy change associated with homogenous nucleation of a sphere of radius r

There are two types of nucleation processes:

- Primary nucleation

Homogeneous primary nucleation: crystals appear spontaneously in the solution without any contact with the walls of the reactor or any solid particle. This type of primary nucleation occurs very rarely in practice, because it implies the absence of foreign materials in the solution (dust, impurities and microbubbles of gas...).

Heterogeneous primary nucleation: Crystals are induced by the presence of foreign surfaces (particles) due to their interactions with the environment (walls, stirrer probe...).

- Secondary nucleation is induced by crystals that already exist in the solution from the primary nucleation or by seeding manually the solution.

Nucleation is considered as the rate-limiting step in the crystallization process. In some cases, the system can be supersaturated but maintained in the Ostwald metastable zone. The concentration-temperature diagram shown in Figure I.3 shows the different zones of stability and metastability according to Ostwald.

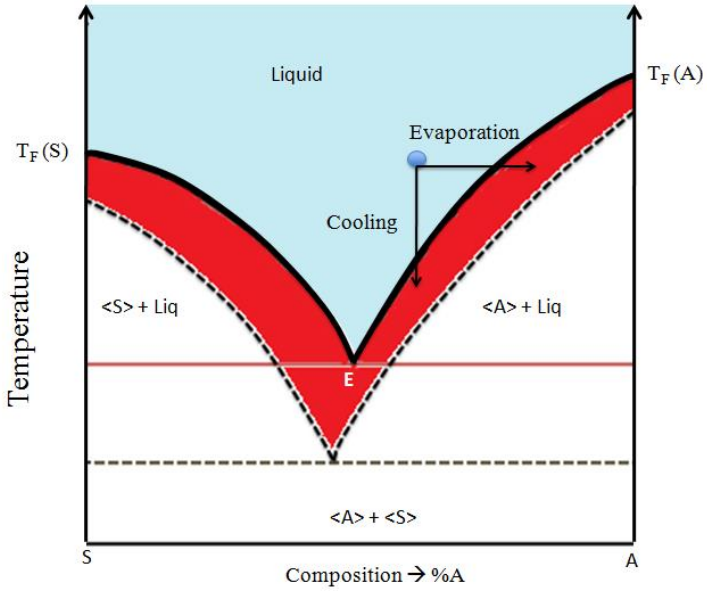

Figure I.3 Schematic representation of an eutectic phase diagram with the three main zones: undersaturated (blue), metastable (red) and spontaneous nucleation (white) during cooling or evaporation process

The main zones of concentration-temperature diagram are:

- Undersaturated zone (blue). In this zone, nucleation can't occur. Consequently, if a crystal is added to this solution it would definitely dissolve.
- Metastable/Ostwald zone (in red) crystallization can be observed after long induction such as stirring.
- Spontaneous nucleation zone (in white). In this zone, nucleation spontaneously occurs.

The metastable zone and the spontaneous nucleation zone are delimited by metastable zone width MSZW which is a kinetic boundary. Characterizing the MSZW is very important in crystallization process since it gives accurate information on the mechanisms of nucleation in a given system. However, the MZWS is greatly influenced by many parameters such as the supersaturation rate, the cooling rate, the impurities and stirring.

I.2.1.3 Crystal growth

The crystal growth occurs once the stable nucleus has succeeded in reaching r*. Crystal growth is accompanied by the appearance of crystal faces that lead to crystal morphology.

Nucleation and growth continue to occur simultaneously while the supersaturation exists. Once the supersaturation is exhausted, the solid–liquid system reaches equilibrium and the crystallization is complete. Hence, small crystals having a large surface area to volume ratio than large crystals will dissolve to reach a lower energy state and get transformed into large crystals. Large crystals, with their greater volume to surface area ratio, exhibit a lower energy state and consequently they are thermodynamically favored. This is what we call Ostwald ripening.

During crystal growth mechanisms, many factors can affect the crystallization of a compound in solution and can result in different polymorphic forms:

- Nature of the solvent: by simply switching from polar to apolar solvents, different polymorphic forms of the same compound can crystallize. It has been proven that a solvent acts by selective adsorption to certain faces of some of the polymorphs and thereby inhibits their nucleation and retards their growth to the advantage of others [28].
- Presence of impurities: many examples in literature [29,30] have proven that the crystallization of a specific polymorphic form can be enhanced or inhibited by adding a specific impurity or an additive at low concentrations to the system.
- Temperature: For enantiotropically related polymorphs, the solid-solid transition temperature is an important thermodynamic parameter that should be taken into account during crystallization essays from solution.

I.2.2 Crystallization from the melt

Melt crystallization consists in heating a compound up to its melting point then cooling rapidly the liquid melt under its fusion temperature (T_{fus}), generating by that a driving force to form crystals or amorphous materials. Figure I.4 illustrates the possible pathways following a melt crystallization in the case of a pure monomorphic compound.

The following interpretations can be noted:

Pathway (a): the system follows the equilibrium line of the liquid beyond T_{fus}. The cooled liquid is relative to the crystalline state.

Pathway (b): the system undergoes an out-of-equilibrium state called glassy state following a fast cooling (quenching) from the molten material. The quenching results in the formation of an amorphous material. Many examples of amorphous APIs obtained by melt quenching are reported in literature [31,32].

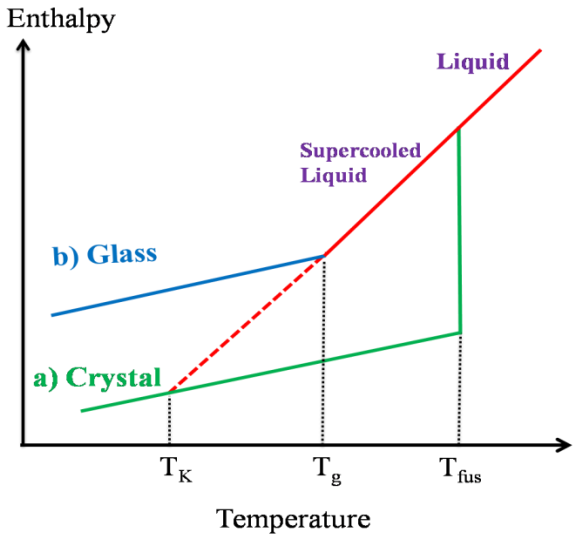

Figure I.4 Schematic representation of the paths followed by melt crystallization in a monomorphic system

I.2.3 Sublimation

Sublimation is the direct transition of a substance from the solid to the gas state without passing through the liquid state. When the solid is heated under vacuum in a sublimation apparatus, it will volatilize and condense on the cold surface of the tube, leaving a non-volatile residue of impurities behind. The example of glycine metastable forms crystallizing from gas phase via sublimation under vacuum is reported in literature[33].

I.2.4 High Energy Milling (HEM)

High energy milling process is usually used in pharmaceutical industry to reduce the particle size of powder particles. This process consists in grinding the powder by applying a mechanical stress with balls mills rotating in a high frequency. This grinding can result in the deformation of crystals, energy accumulation in the volume or at the surface of crystals, and subsequently amorphization [(34)]. Many examples are reported in literature illustrating the amorphization of compounds upon milling including lactose, D-trehalose and linazapran[(35,36,37)]. Grinding a crystalline compound can also result in phase transformation: this is the case of crystalline Γ-sorbitol that undergoes a complete structural transformation towards the metastable A-form of sorbitol upon mechanical milling [(38)].

In this work, the millings were performed by using a planetary mill Pulverisette 7 premium line (Fritsch, Germany) placed in a room at 4 °C.

The planetary mill is constituted by a horizontal disk with a rotating speed Ω, two vials with a rotating speed ω are fixed on this plate. Ω and ω can be opposite and are independent. The maximum speed is 1200 rpm for Ω and 1200 rpm for the satellites (ω). The couple (Ω,ω) determines the milling mode: mainly hitting mode (Ω and ω have opposite sign), friction (Ω and ω have the same sign) (Fig.I.5). In our experiments, the milling couple was fixed at 400 rpm.

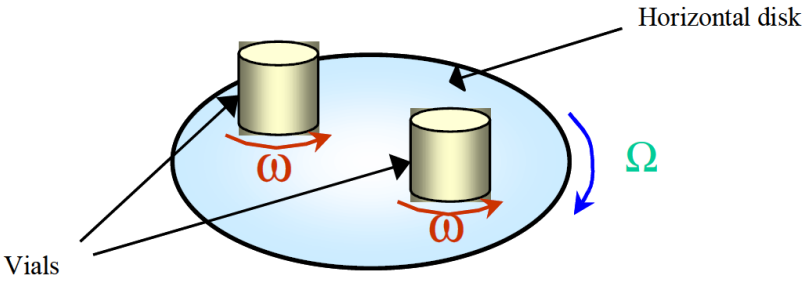

Figure I.5 Schematic representation of the HEM

In order to avoid the overheating inside the vials, it is possible to program alternated milling durations with break spells. Furthermore, the reverse mode was activated in order to improve the homogeneity of the samples (the « reverse » mode consists in inverting the rotation of the vials and the disk at the end of each milling cycle), which is the main problem that appeared during the HEM experiments. The program applied was successive cycles of milling of 30 minutes followed by 10 minutes break. In addition to neat millings, some Liquid Assisted Grinding (LAG) experiments can be performed with this device one or several drops of

solvent are added to the starting powders before milling. The phenomena taking place during milling will be totally disturbed by the solvent addition. Dissolution/recrystallization processes, catalyzed by the milling, will be generated instead of hitting and friction. This process is an interesting pathway to screen the existence of solvates, or co-crystals, and it limits the amorphization of the milled materials.

I.2.5 Spray Drying

Spray drying is a process that consists in dispersing a solution into spray, then evaporating rapidly the solvent in the generated spray and finally collecting the dried substances. The fast evaporation rate can contribute to the formation of amorphous materials[39] or metastable forms [40] in accordance with Ostwald rules stating that '*When leaving a given state and in transforming to another* state*, the state which is sought out is not the thermodynamically stable one, but the state nearest in stability to the original state'* [41].

Spray drying process will be detailed in Part I.4.

I.2.6 Desolvation and dehydration

Desolvation (or dehydration) of solvates (or hydrates) can lead to anhydrous crystal forms or amorphous solids. The desolvated form (anhydrous form) can have the same crystal form from which it was derived or a new crystal form. Examples of phase changes occuring upon desolvation of solvates are reported in literature including dehydration of rimonabant monohydrate resulting in a new polymorphic form [42], the dehydration of tranilast monohydrate over P_2O_5 inducing the formation of an amorphous solid [43] and desolvation of olanzapine solvates resulting in anhydrous metastable forms [44].

I.2.7 Confinement

The confinement method is based on reducing the domain size available during the crystallization process resulting in the growth of micro or nanometer size crystals through embodiement within nanoporous polymer, capillaries, metallic substrates, glass matrices, or combinations. Examples reported in literature revealed that the embedded nanocrystals under confinement can exhibit an array of phase behaviors including formation of metastable amorphous and formation of new polymorphs, and shifts of thermotropic relationships between polymorphs [45,46,47].

I.3 Thermodynamics and Heterogeneous equilibria

The total energy in a thermodynamic system is represented by the free enthalpy (also called Gibb's free energy [48] given by :

$G = H - TS$

With:

G: Gibb's free enthalpy ($J.mol^{-1}$)
H: enthalpy ($J.mol^{-1}$)
T: temperature (K)
S: entropy ($J.mol^{-1}.K^{-1}$)

When several phases take place in a system (gas, solid(s) and liquid(s)), the equilibria between these different phases are called heterogeneous equilibria.

I.3.1 Phase diagrams

Phase diagrams reflect the free enthalpy G supposed to be minima at the thermodynamic equilibrium including stable or metastable equilibria. Heterogeneous equilibria and construction of phase diagrams are valuable tools for the identification of phase nature. Exploring phase diagrams is essential for the development and the characterization of polymorphic forms during crystallization with solvents or with a solid compound or with an impurity [49].

If we consider a system consisted of *C* independent components, with N intensive variables (*e.g* temperature and pressure) with φ phases, we can determine the variance *V* defined as the number of variables necessary to determine the equilibrium of the system. This variance is defined by the Gibbs law [50] as:

$V = C + N - \varphi$

Accordingly, different phase diagrams can be defined: unary, binary, ternary, quaternary etc... Many cases including eutectic, peritectic, metatectic (catatectic), monotectic, eutectoid, peritectoid and monotectoid invariants can exist. Only cases of binary phase diagrams with eutectic, peritectic, metatectic (catatectic) invariants are presented in this part because they were encountered in the experimental found in this work.

I.3.1.1 Binary phase diagram in isobaric condition

Binary systems consist of two independent components (C=2), with a fixed pressure (N=1).

Binary phase diagrams are represented in a temperature-composition graphic, where the temperature is plotted on the ordinate axis and the composition on the abscissa axis and the

pressure is supposed constant. When three phases are in equilibrium, the variance is equal to 0. These invariant equilibria are represented by horizontal lines on binary phase diagram.

Solid solutions

When homogeneous mixtures of two or more kinds of compounds occur in the solid state, they are known as solid solutions. Studies have shown that solid solutions, by means of insertion or substitution can substantially modify the energy landscape between polymorphs [(51)]. Solid solutions are of two types: substitutional solid solutions and interstitial solid solutions.

a) Substitutional solid solution

If the molecules are replaced in the crystal lattice by other molecules then the solid solution is known as substitutional solid solution (Fig.I.6).

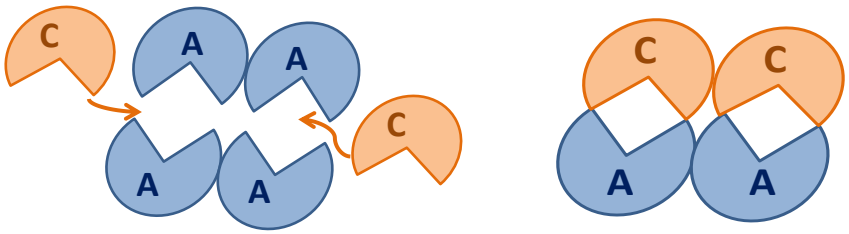

Figure I.6 Illustration of ordered substitutional solid solution

b) Interstitial solid solution

If molecules occupy the interstitial sites in the crystal structure then the solid solution is known as interstitial solid solution (Fig.I.7).

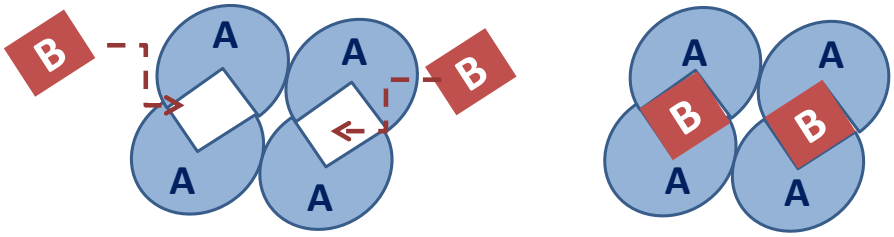

Figure I.7 Illustration of interstitial solid solutions where B molecules occupy the interstitial sites between A molecules

I.3.1.1.1 Solid-liquid equilibria

At a fixed pressure, several situations can be observed between two components.

Eutectic invariant

Often, melting points are reduced when B is added to A or A is added B. The eutectic invariant represents the equilibrium between liquid and two solids. Below the eutectic invariant, no liquid phase should exist only mixture of two solids. At the eutectic composition « E », the mixture A and B has the lowest melting point.

Two types of binary phase diagrams involving solid-liquid equilibria with and without solubility in the solid-state are represented in Figure I.8.

a) b)

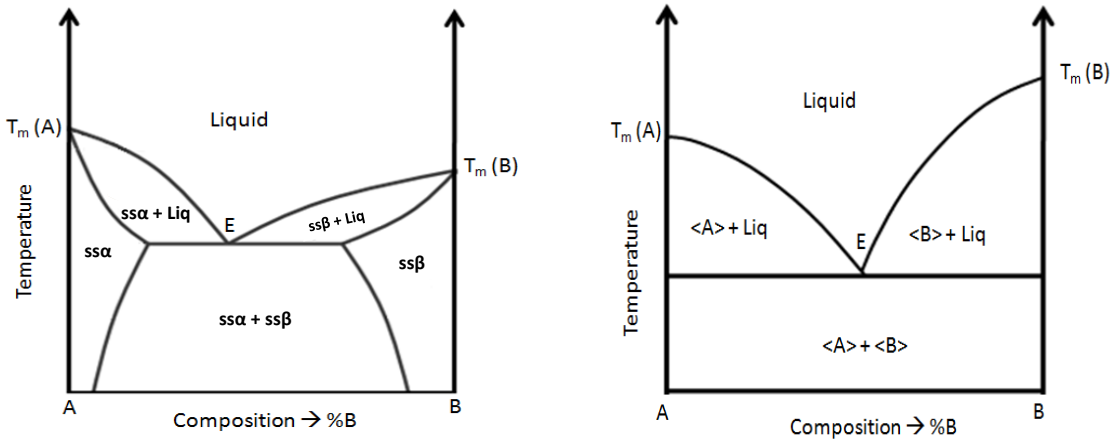

Figure I.8 Schematic representations of eutectic binary phase diagrams between two compounds A and B a) with partial solid solution b) with immiscibility at the solid state

Binary phase diagrams with defined compounds

Two components of binary system might combine in the solid state and form stoichiometric defined compounds. The melting of these phases can be congruent, in this case the liquid has the same composition as the solid, or non-congruent in this case the defined compound melts and it gives rise to a liquid with a composition different from the initial composition and a solid A (Fig.I.9 a-b). This melting will result in a binary invariant known as peritectic.

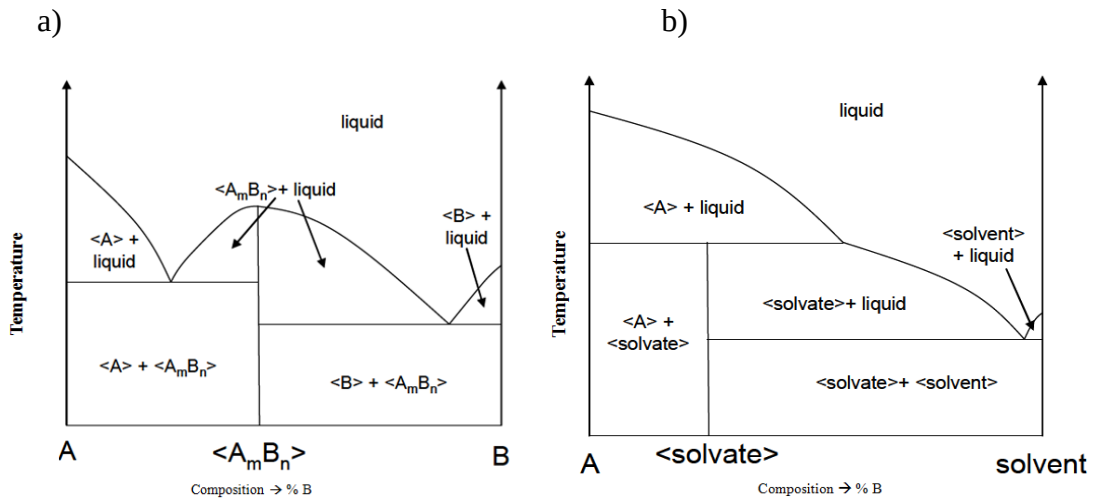

Figure I.9 Schematic representations of binary phase diagrams exhibiting a stoichiometric compound: a) with a congruent melting b) with a non-congruent melting (peritectic invariant).

Metatectic invariant

The compound A crystallizes in two polymorphic forms I and II enantiotropically related with a defined reversible solid-solid transition $T_{tr\ I \leftrightarrow II}$. By adding compound B, this solid-solid transition will decrease until reaching an invariant called metatectic where the solid transition from I to II is lower than the predefined value $T_{tr\ I \leftrightarrow II}$. Examples of cases of metatectic phase diagrams are illustrated in Figure I.10.

Figure I.10.a depicts a case in which solvent molecules B enter the crystal lattice of Form II only and lead to the decrease of the solid-solid transition temperature $T_{tr\ I \leftrightarrow II}$. In this case, the insertion of molecules of solvent B enlarges the stability domain of Form II towards low temperatures down to the metatectic invariant.

Figure I.10.b depicts a case in which molecules of solvent B enter the crystal lattices of both polymorphic forms (Form I and Form II) resulting in two partial solid solutions and leading to the decrease the solid-solid transition temperature $T_{tr\ I \leftrightarrow II}$ down to the metatectic invariant. In this case, the insertion of molecules of solvent B enlarges the stability domain of ss2 more than ss1 down to the metatectic invariant.

Figure.I.10.c depicts a case in which molecules of solvent B enter the crystal lattices of both polymorphic forms (Form I and Form II) resulting in two partial solid solutions and leading to the increase of the solid-solid transition temperature $T_{tr\ I \leftrightarrow II}$ up to a temperature labelled T_y for a B composition below y, and to the decrease of the solid solid transition temperature $T_{tr\ I \leftrightarrow II}$ down to the metatectic invariant for a B composition above y.

a)

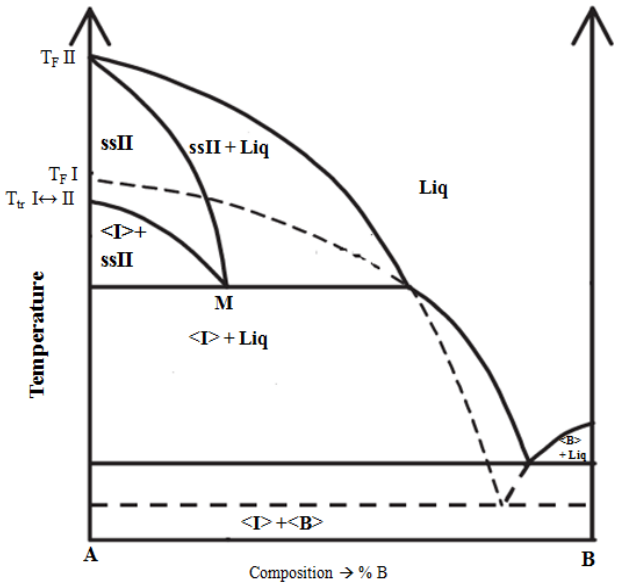

b)

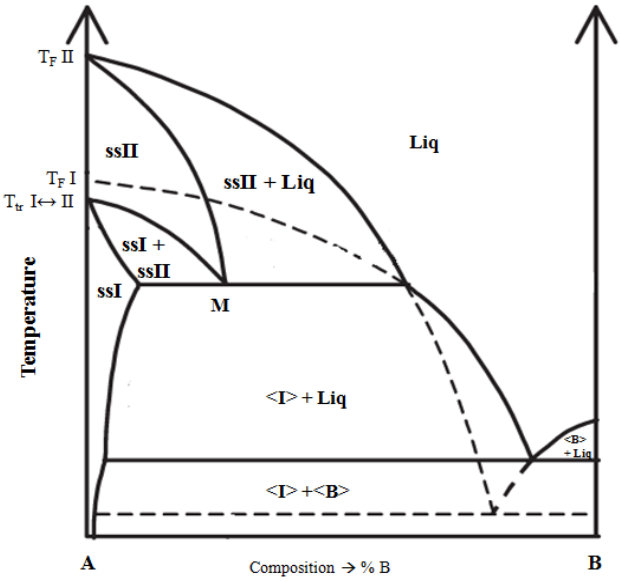

c)

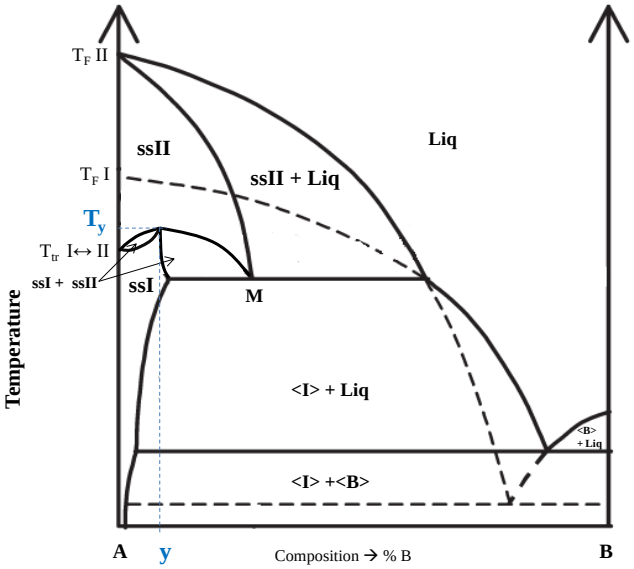

Figure I.10 Schematic representation of metatectic binary phase diagram

a) Increase in stability domain of Form I towards low temperature down to the metatectic invariant upon insertion of solvent molecules B

b) Increase in stability domain of ssII more than ssI towards low temperature down to the metatectic upon insertion of solvent molecules B

c) Decrease in stability domain of ssII more than ssI towards high temperature up to T_y for a composition below y, then increase in stability domain of ssII more than ssI towards low temperature down to the metatectic upon insertion of solvent molecules B above y composition.

I.3.1.1.2 Solid-vapour equilibria

The partial pressure of solvent is the ratio of the partial vapour pressure of a volatile solvent (P) over the saturating vapour pressure of this solvent (P^{sat}) at a given temperature.

When the solvent in the atmosphere is water, Relative Humidity (hereafter RH) is used.

$$RH = (P_{H_2O} / P^{sat}_{H_2O})_{T=cst}$$

RH is the ratio of the partial pressure of water vapor to the equilibrium vapor pressure of water at the same temperature. The relative humidity depends on temperature and the pressure of the system of interest.

When a solid phase is in interaction with gaseous phases, two types of interactions can be observed: Adsorption and adsorption.

Adsorption is the adhesion of water or solvent molecules in the surrounding gas atmosphere on the surface of solid materials via physical or chemical bonding.

Absorption is the incorporation of solvent molecules inside the solid structure.

A solid is classified as hygroscopic, if in ambient conditions of temperature and pressure, it uptakes water from the surrounding atmosphere and retains it.

A solid is classified as deliquescent if its strong affinity with solvent from the surrounding gas results in the formation of liquid solution following the solvent uptake. The critical relative humidity is the value above which the solid becomes deliquescent at a given temperature.

I.4 Spray Drying

This part is dedicated to give an overview of Spray Drying process by describing its principles, presenting its applications, advantages and parameters.

The spray dryer used in this thesis is a Mini Spray Dryer Buchi B-290 operating in a co-current configuration.

I.4.1 Review and applications of Spray Drying

Spray Drying process was invented by Samuel Peroy who first described the principle of spray drying in a patent issued in 1872 entitled 'Improvement in Drying and Concentrating Liquid Substances by Atomizing' [(52)]. This invention comes along with the market need to reduce weight of foods and other materials during transportation. The early developed spray dryers presented inconveniences because they weren't operating continuously. For this reason, few commercial applications have been made till 1920 [(53)].

Since that date, manufacturers have been improving Spray Drying designs to accommodate its use for large scale and to offer applications in many fields including pharmaceuticals, food and chemicals (detergents, soaps, pesticides, pigments, fertilizers, inorganic chemicals, organic chemicals…) [(54, 55,56,57)].

By counting the volume of spray-dried products, the dairy industry including skim milk, whole milk and fat-enriched milk is the largest user of spray dryers in food processing [(58)].

In pharmaceutical field, the first application of spray drying was devoted to obtain dry extracts of active raw materials from plants [(59)]. Since that date, a broad range of pharmaceuticals of active ingredients and excipients is produced yearly by Spray Drying.

The reason behind the increase of Spray Drying market is definitely related to the benefits offered by this process. Indeed, Spray drying is quite known for its advantages including:

- Operating continuously with maximum efficiency and minimal environmental impact. Indeed, in Spray Drying process there is no need for the usual sequence of operations: crystallization, filtration, drying and milling (or micronization). This may represent a considerable reduction of production costs [(60)].
- Delivering powder with controlled size and morphology [(61)]. Reducing particle size in pharmaceuticals is considered as an important criteria especially in pulmonary therapy where particle size distribution should be below 5 µm for easy transport to the lungs [(62)].

- Enhancing the solubility of poorly soluble drugs. Spray Drying process is known for producing amorphous materials and metastable forms. Thereby the solubility and the bioavailability of the products is improved [63,64,65]. The example of co-spray drying of ibuprofen with ordered mesoporous silica SBA-15 is a model example [66].
- Protecting a core material from degradation and modifying the release profiles of the active ingredients by microencapsulating [67]. Spray Drying is the most common and cheapest technique to produce microencapsulated food materials. Examples of flavors encapsulated with Arabic gum have been produced by Spray Drying since the 1930s [68].

I.4.2 Spray drying basics

Spray drying is a one-step drying operation process by which a liquid feed is atomized into fine droplets called 'spray' and evaporated subsequently with a hot drying gas resulting in the access to a dry powder. The schematic principle of a spray dryer device is illustrated in Figure I.11.

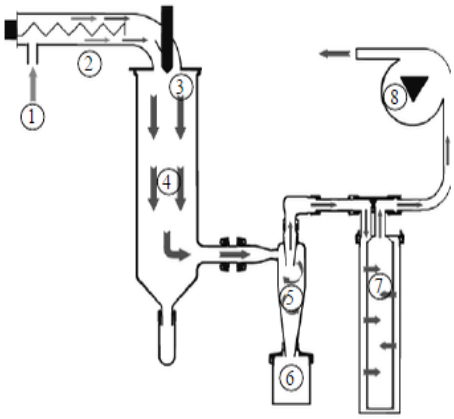

Figure I.11. Schematic principle of a Spray Dryer device with co-current flow. 1- Dry air (or nitrogen) inlet pipe; 2- Electric resistance; 3- Atomizer (nozzle system); 4- Drying chamber; 5- Cyclone, for the separation of particles and gas; 6- Bowl collector; 7- Exit filter (polyester); 8- Aspirator

The spray drying process consists of four basic stages: atomization of the feed, droplet air contact, droplet drying and separation of the dried particles from the gas.

I.4.2.1 Atomization of the feed

The liquid feed can be a solution, an emulsion or a suspension. However, the mixture should be homogenous in order to get an uniform size distribution in the particles.

The solution is pumped with a peristaltic pump to the spray nozzle. On the other side, nitrogen is transported under high pressure and velocity to the spray nozzle as well. The contact between high velocity gas and liquid breaks up the feed into fine droplets.

Atomization of the feed consists of successive steps [(69)] and is illustrated in Figure I.12:

1- A shear instability first forms waves on the liquid. The instability arises from the relative difference between the velocity of the liquid jet (V_1) and the gas ($V_2 > V_1$).
2- Above a critical velocity (of about 20 $m.s^{-1}$), the shears will give birth to digitations form.
3- As a drop moves through a gas, the pressure gradient causes its spherical shape to change and distort. As the distortion continues, the drop becomes an ellipsoid, or disk-shaped, until an upper limit is reached and breakup begins. These digitations will then stretch and become ligaments.
4- The liquid ligaments are stretched in the air stream and their diameter decreases until they break into drops. When these ligaments are stretched, their diameter decreases until they break into drops resulting in the primary atomization.
5- If drops produced by this process are big enough, they will break again during the process of secondary atomization.

The device that allows the atomization is called atomizer. Various types of atomizers exist on the market including pneumatic atomizer, pressure nozzle, spinning disk configurations, two fluid nozzle and sonic nozzle. The choice of the atomizer depends on the desired droplet size that has an impact on the final particle size. Compared to all the types of atomizers, the two fluid nozzle is the best suitable for small-scale production because it tends to consume less atomizing gas.

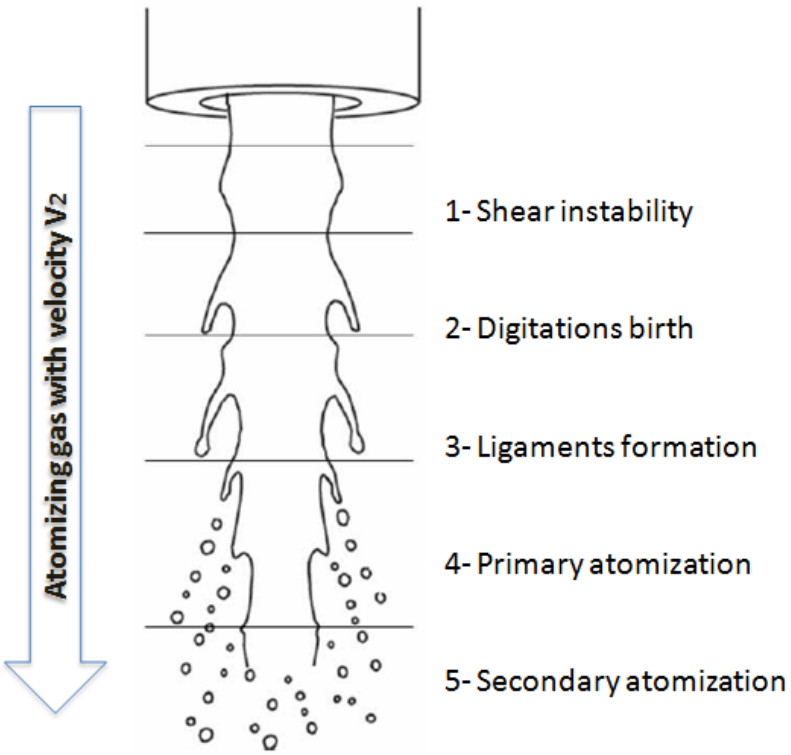

Figure I.12 Representation of different steps during atomization of liquid into Spray

I.4.2.2 Droplet-air contact

Droplets are brought into contact with hot gas (air or nitrogen) inside the drying chamber. The type of contact between the spray and the air is determined by the direction of both spray and drying air. Two types of dryers exist: co-current and counter-current dryers.

Counter-current dryer: the hot air flows in the opposite direction of the spray.

Accordingly, the spray is in contact with the coolest drying air. This type of dryers is recommended for materials with internal moisture retention, requiring a longer cycle of heat to draw out the moisture.

Co-current dryer: the spray and the hot air have the same flow direction inside the drying chamber. Co-current dryers are considered as the best designs for products that are keen to suffer from heat degradation: the hottest drying air is in contact with the droplets at their maximum moisture content (right after being released from the nozzle), accordingly, the co-current dryer results in a quick drying compared to the counter-current dryer and is less harmful to heat sensitive substances (*e.g* APIs).

Depending on the solvent used in the feedstock, Spray Drying experiments can be carried out in open or close mode.

The open cycle is applied for aqueous feeds: the drying gas is the air and it is vented to the atmosphere.

When the feedstock consists of solids mixed with flammable organic solvents (volume in water greater than 50% in volume), the closed mode is applied: the drying gas is nitrogen. The system will be connected to an accessory called inert Loop that enables the safe use of organic solvent in a closed loop and avoids any explosion risk or oxidation (Fig.I.13). The vapors of the solvents are condensed in a refrigerator and collected in a closed bottle. The cleaned gas stream is then preheated and it flows back to the Mini Spray Dryer.

A closed-cycle dryer recycles the drying gas, which is an inert gas such as nitrogen.

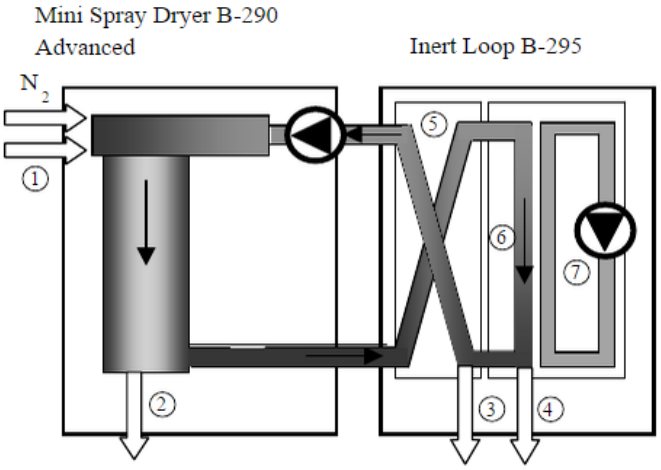

1- Feed
2- Product
3- Exhaust gas
4- Solvent
5- Preheat exchange
6- Condensation
7- Cooling unit

Figure I.13 Combined system of the Mini Spray Dryer B-290 and Inert Loop B-295

I.4.2.3 Droplet drying

It is important that droplets have sufficient residence time in the drying chamber to get efficiently dried particles. The droplet residence time in the drying chamber can give an idea whether or not the droplets are sufficiently dried. However, Spray Drying process involves many parameters: atomization of the feed, spray air contact/mixing, spray evaporation/drying, drying air temperature and humidity. Due to this complexity, it is difficult to simulate the droplet residence time inside the chamber.

Droplet drying takes place in two stages:

During the first stage, temperature at the surface of the droplet is less than the temperature of the drying gas. The droplets are dried without any real evaporation.

The second stage the temperature at the surface of the droplet is approximately equal to the temperature of the drying air. Consequently, droplets will decrease in volume.

The evaporation begins when there is no longer enough moisture to maintain saturated conditions at the droplet surface, causing a dried shell to form at the surface. Evaporation will depend on the diffusion of moisture through the shell, which is increasing in thickness. Once there is no longer enough moisture in the droplet, this leads to a dried particle that has a temperature lower than the temperature of the drying gas enriched with moisture.

Different products have different evaporation and particle-forming characteristics. Some expand, others contract, fracture or disintegrate. The resulting particles may be relatively uniform hollow spheres, or porous and irregularly shaped.

I.4.2.4 Separation

The dried particles are separated from the gas stream and collected by a conical container called cyclone (Fig.I.14). The gas charged with dried particles enters tangentially into the cyclone with an inlet velocity and moves in a spiral pattern. Thus, the strong swirling flow forms a vortex inside the cyclone. Due to their high inertia, large particles won't be able to follow the curve of the vortex. Consequently, with the effect of centrifugal force, they will collide with the cyclone walls, lose speed, and fall to the bottom of the cyclone where they are collected.

Smaller particles will remain in the helical gas that will exit the cyclone through the gas outlet at the top of the cyclone.

An expression is derived relating the collection efficiency to the different cyclone parameters and operating conditions.

with

$$\eta = \frac{\pi N_e \rho_P d_P^2 V_g}{9 \mu W}$$

η - collection efficiency

ρ_p - particle density

d_p - particle diameter

V_g - gas velocity

μ - gas viscosity

W - width of the rectangular inlet

N_e - effective number of revolutions

$$N_e = \frac{1}{H}\left(L_1 + \frac{L_2}{2}\right)$$

The value of N_e is derived from the following equation

with:

L_1 - *height of the main upper cylinder*

L_2 - *height of the lower cone*

H - *height of the rectangular inlet through which the dirty gas enters*

This model indicates that the collection efficiency is directly proportional to the particle size, particle diameter, the gas residence time which depends on gas inlet velocity and the number of turns in the vortex whereas it is inversely proportional to the gas viscosity and the cyclone inlet width.

If the gas temperature increases, its density will decrease whereas its velocity (V_g) will increase; in this case, the collection efficiency (η) is likely to increase.

If the viscosity of the gas (μ) that carries the particles to the cyclone increases then the collection efficiency will decrease with all the other factors remaining constant.

The term cut point is employed to design the size of particle that will be removed from the stream with a 50% efficiency. Accordingly, particles larger than the cut point will be removed with a greater efficiency and smaller particles with a lower efficiency.

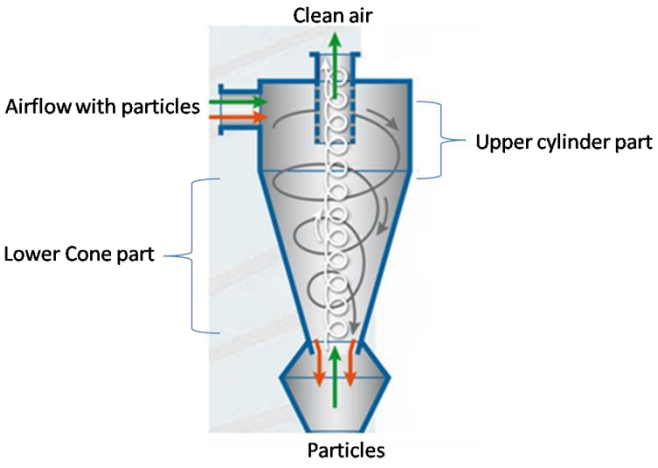

Figure I.14 Schematic representation of a cyclone

Cyclonic separation is considered as an efficient method for Spray Drying process since it is cheap, operates continuously with high safety without consuming energy, fits to conditions of temperature and process pressure and requires little maintenance.

I.4.3 Parameters

Many parameters in Spray Drying experiments can be adjusted by the operator including: nature of the solvent (organic or water), feed rate, aspirator rate, atomizing gas flow, inlet temperature and the humidity of the drying gas.

Studies have proven that these parameters are interrelated and they can be involved in modifying the properties of spray-dried substances [70,71,72].

For this reason, it is important to understand every parameter effect and to set the optimal conditions and settings allowing the access to the desired product.

In the section below, we will present Mini spray Dryer 290 adjustable parameters.

Table I.1 summarizes the parameters that can be adjustable in the mini Spray Dryer B-290 and their impact on the final product.

Table I.1 Impact of Spray Drying parameters on the properties of the spray-dried powder.

Parameter / Dependance	Aspirator ↑	Humidity drying gas ↑	Inlet temperture ↑	Spray gas flow ↑	Feed rate ↑	Solid concentration ↑	Organic solvent instead of water ↑
Outlet temperature	↑	↑	↑	↓	↓	↑	↑
Particle size	—	—	—	↓	↑	↑	↓
Humidity in final product	↓	↑	↓	—	↑	↓	↓

Legend:

High influence	Increasing parameter
Moderate influence	Increasing variable
Minor influence	Decreasing variable
No influence	

I.4.3.1 Inlet temperature

The inlet temperature is usually set above the boiling point of the solvent of the feed solution. It should be noted that the higher inlet air temperatures is, the faster the evaporation rate is. The fast evaporation can be a favoured condition to get access to metastable forms or amorphous materials in accordance with Ostwald rules. Besides, a higher inlet temperature will help the system get rid of internal moisture content which results in dryer powder.

In addition, an increase of the inlet temperature will result in an increase of the outlet temperature. A big difference between inlet and outlet temperature will result in a residual moisture in the particles that can be an inconvenient for hygroscopic powders.

At high inlet temperatures, amorphous particles may exceed their glass transition temperatures, making the amorphous particles sticky and rubbery. Consequently the yield will decrease as well as the recovery from spray drying.

I.4.3.2 Drying gas humidity

The drying gas humidity changes from an open mode to a closed mode. As mentioned previously, operating in an open mode involves the use of air as drying gas. Drying with air will bring humidity to the system fairly close to the relative humidity of the operating room. A high drying gas humidity can result in moist particles that could adhere to the glassware thereby decreasing the yield. Besides, the increase of humidity in the final product will affect important physical parameters of the spray-dried particles (*e.g* decrease of the glass transition of amorphous materials). In contrast, the use of pure nitrogen as a drying gas will theoretically bring no humidity to the system operating in a close mode and will result in dryer powder.

I.4.3.3 Spray gas flow

The rotameter is an indicator for the spray gas flow. Table I.2 gives a correlation between indicated height and volume throughput.

Applying a higher spray gas flow will generate smaller droplets from the nozzle resulting in the decrease of the solid particle size.

Table I.2 Table of correlation between the height of the ball in the rotameter and the spray gas flow expressed in (L/h)

Height (mm)	L/h
5	84
10	138
15	192
20	246
25	301
30	357
35	414
40	473
45	536
50	601
55	670
60	742
65	819

I.4.3.4 Feed rate

The feed rate is controlled by the peristaltic pump rate that can be adjusted between 0 and 100%. Depending on the organic solvent in the feed solution, different types of tubes can be used (silicone or tygon) differing in the inner and outer diameters. With different tube diameters, the absolute flow would change. The diagram in Figure I.15 shows the correlation for the standard 2/4 silicone tube.

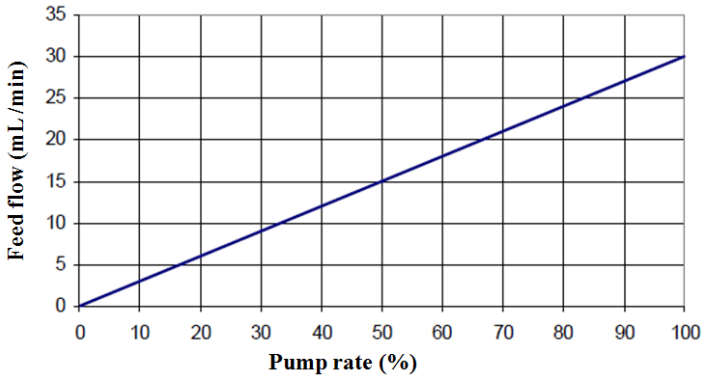

Figure I.15 Diagram of correlation between the pump rate expressed in % and the feed flow expressed in mL/min

If the feed rate is too high, the outlet temperature will be too low because there will be more liquid to evaporate and more solvent vapor in the system. It will also result in the increase of the moisture content in the gas and in the final product.

I.4.3.5 Solid concentration

A concentrated feed as well as the generated drop contain more solid and less liquid than a diluted feed. This will result in an increase in the particle size and a decrease in the final product humidity. Besides, the yield will increase since bigger particles are easier to separate with the cyclone.

I.4.3.6 Aspirator rate

A higher aspirator rate offers more drying energy and increases the outlet gas temperature and results in a higher degree of separation in the cyclone. The maximum aspiration in the Mini Spray Dryer B-290 is 35m^3/h.

I.4.4 Brief conclusion

Spray drying is an interesting process for pharmaceutical, agrochemical industries since it uses one-step process for formation and drying of powders.

A listing of product specifications should be gathered prior experiments: What is the material? Is there any historical data on spray drying this material? Is it temperature-sensitive? Does it sublimate? Is it hygroscopic? What is the solidification temperature of the solvent? Is the material hazardous? Is it aqueous or solvent-based? Does the powder present an explosion hazard? Is there any particle size requirements?

Answers to these questions are essential prior carrying out Spray Drying experiments.

REFERENCES

1.Shah, Birju, Kakumanu, Vasu Kumar, et Bansal, Arvind K. (2006) Analytical techniques for quantification of amorphous/crystalline phases in pharmaceutical solids. *Journal of pharmaceutical sciences*, vol. 95, no 8, p. 1641-1665.

2.Cui, Yong.(2007), A material science perspective of pharmaceutical solids. *International journal of pharmaceutics*, vol. 339, no 1, p. 3-18.

3.N. JagadeeshBabu, and Ashwini Nangia (2011) Solubility Advantage of Amorphous Drugs and Pharmaceutical CocrystalsCryst. Growth Des., 11 (7), pp 2662–2679

4.Morten Allesø, Norman Chieng, Sönke Rehder, Jukka Rantanen, Thomas Rades (2009) Enhanced dissolution rate and synchronized release of drugs in binary systems through formulation: Amorphous naproxen–cimetidine mixtures prepared by mechanical activation Journal of Controlled ReleaseVolume 136, Issue 1, Pages 45–53

5.Gurunath, S., Kumar, S. P., Basavaraj, N. K., &Patil, P. A. (2013) Amorphous solid dispersion method for improving oral bioavailability of poorly water-soluble drugs. Journal of Pharmacy Research,6(4), 476-480.

6. Petit, S. Coquerel, G. in Polymorphism : in the Pharmaceutical industry ; Rolf Hilfiker (Ed) 2006

7. McCrone WC, Fox D, Labes MM, Weissberger A, Rice SA.(1965) Physics and Chemistry of the Organic Solids State.Volume 2. Phys. Today. ; 18 (8) : 59.

8. Bernestein J. (2002) Polymorphism in molecular crystals. Clarendon Press / International Union of Crysallography;

9.M. J. Burger, (1951),Phase transformation in solids, Wiley, New York, p 147.

10.Burger, A. and Ramberger, R. (1979) On the polymorphism of pharmaceuticals and other molecular crystals. I. MicrochimicaActa, vol. 72, no 3-4, p. 259-271.

11. Doelker, E. (2002),Crystalline modifications and polymorphism changes during drug manufacture, Annalespharmaceutiquesfrancaises, Vol. 60, No. 3, pp. 161-176.

12. Datta, S., & Grant, D. J. (2004). Crystal structures of drugs: advances in determination, prediction and engineering. *Nature Reviews Drug Discovery*,*3*(1), 42-57.

13. Brittain HG.(2009) Polymorphism in pharmaceutical solids. Informa HealthCare.

14. Lee EH.(2014) A pratical guide to pharmaceutical polymorph screening 1 selection.Asian Journal of Pharmaceutical Sciences.

15. Sheth A, Grant D. (2005) Relationship between the structure and properties of pharmaceutical crystals. 23 : 36-48.

16. Hilfiker R. (2006)Polymorphism : in the pharmaceutical industry. John Wiley 1 Sons.

17. D. Martins, M. Sanselme, O. Houssin, V. Dupray, M. N. Petit, D. Pasquier, C. Diolez, G. Coquerel(2012) Physical transformations of the active pharmaceutical ingredient BN83495: enantiotropic and monotropic relationships. Access to several polymorphic forms by using various solvation–desolvation processes.*CrystEngComm*, 14, no 7, p. 2507-2519.

18. Sun, C., Zhou, D., Grant, D. J., & Young Jr, V. G(2002). Theophylline monohydrate ActaCrystallographica Section E: Structure Reports Online, vol. 58, no 4, p. 368-370.

19.Ripmeester, J. A. (1993). Crystalline β-cyclodextrin hydrate is non-stoichiometric with 10.5–12 waters per cyclodextrin molecule. *Supramolecular Chemistry*, *2*(2-3), 89-91.

20. Morris K., (1999) Structural aspect of hydrates and solvates H.G. Britain (Ed.), Polymorphism in Pharmaceutical Solids, Marcel Dekker, ,vol. 95, pp. 125–226.

21. Henck, J. O., Griesser, U. J., & Burger, A. (1997). Polymorphism of drug substances-An economic challenge. *PharmazeutischeIndustrie*, *59*(2), 165-169.

22. Morris, K. R., & Rodriguez-Hornedo, N. (1993). Encyclopedia of Pharmaceutical Technology. *Vol. 7 Marcel Dekker, New York*, 393-440.

23. Petit, S., & Coquerel, G. (1996). Mechanism of several solid-solid transformations between dihydrated and anhydrous copper (II) 8-hydroxyquinolinates. Proposition for a unified model for the dehydration of molecular crystals. *Chemistry of materials*, *8*(9), 2247-2258.

24. Bhattacharya, S., &Saha, B. K. (2013). Polymorphism through Desolvation of the Solvates of a van der Waals Host. *Crystal Growth & Design*, *13*(2), 606-613.

25.Coquerel, G. (2014). Crystallization of molecular systems from solution: phase diagrams, supersaturation and other basic concepts. *Chemical Society Reviews*, *43*(7), 2286-2300.

26. Mullin, J. W. (2001). *Crystallization*.Butterworth-Heinemann.

27. Kashchiev, D., & Van Rosmalen, G. M. (2003). Review: nucleation in solutions revisited. *Crystal Research and Technology*, *38*(7-8), 555-574.

28.Khoshkhoo, S., & Anwar, J. A. M. S. H. E. D. (1993). Crystallization of polymorphs: the effect of solvent. *Journal of Physics D: Applied Physics*,*26*(8B), B90.

29. Poornachary, S. K., Chow, P. S., & Tan, R. B. (2007). Influence of solution speciation of impurities on polymorphic nucleation in glycine. *Crystal Growth and Design*, *8*(1), 179-185.

30.Cashell, C., Corcoran, D., &Hodnett, B. K. (2005). Effect of amino acid additives on the crystallization of L-glutamic acid. *Crystal growth & design*,*5*(2), 593-597.

31.Wojnarowska, Z., Grzybowska, K., Adrjanowicz, K., Kaminski, K., Paluch, M., Hawelek, L., &Bieg, T. (2010). Study of the amorphous glibenclamide drug: analysis of the molecular dynamics of quenched and cryomilledmaterial.*Molecular pharmaceutics*, *7*(5), 1692-1707.

32.Laitinen, R., Löbmann, K., Strachan, C. J., Grohganz, H., &Rades, T. (2013). Emerging trends in the stabilization of amorphous drugs. *International journal of pharmaceutics*, *453*(1), 65-79.

33. Liu, Z., Zhong, L., Ying, P., Feng, Z., & Li, C. (2008). Crystallization of metastable β glycine from gas phase via the sublimation of α or γ form in vacuum. *Biophysical chemistry*, *132*(1), 18-22.

34. Balaz, P. (2008). *Mechanochemistry in nanoscience and minerals engineering*. Springer Science & Business Media.

35. Willart, J. F., Caron, V., Lefort, R., Danede, F., Prevost, D., & Descamps, M. (2004). Athermal character of the solid state amorphization of lactose induced by ball milling. *Solid State Communications*, *132*(10), 693-696.

36. Willart, J. F., De Gusseme, A., Hemon, S., Odou, G., Danede, F., & Descamps, M. (2001). Direct crystal to glass transformation of trehalose induced by ball milling. *Solid State Communications*, *119*(8), 501-505.

37. Willart, J. F., Durand, M., Briggner, L. E., Marx, A., Danède, F., & Descamps, M. (2013). Solid-state amorphization of linaprazan by mechanical milling and evidence of polymorphism. *Journal of pharmaceutical sciences*, *102*(7), 2214-2220.

38. Willart, J. F., Lefebvre, J., Danède, F., Comini, S., Looten, P., & Descamps, M. (2005). Polymorphic transformation of the Γ-form of D-sorbitol upon milling: structural and nanostructural analyses. *Solid state communications*, *135*(8), 519-524.

39.Broadhead, J., Edmond Rouan, S. K., & Rhodes, C. T. (1992). The spray drying of pharmaceuticals. *Drug Development and Industrial Pharmacy*, *18*(11-12), 1169-1206.

40. Matsuda, Y., Kawaguchi, S., Kobayashi, H., &Nishijo, J. (1984). Physicochemical characterization of spray-dried phenylbutazone polymorphs, .*Journal of pharmaceutical sciences*, *73*(2), 173-179.

41. Nývlt, J. (1995). The Ostwald rule of stages. *Crystal Research and Technology*, *30*(4), 443-449.

42.Fours, B., Cartigny, Y., Petit, S., & Coquerel, G. (2015). Formation of new polymorphs without any nucleation step. Desolvation of the rimonabant monohydrate: directional crystallisation concomitant to smooth dehydration.*Faraday discussions*.

43. Kawashima, Y., Niwa, T., Takeuchi, H., Hino, T., Itoh, Y., &Furuyama, S. (1991). Characterization of polymorphs of tranilast anhydrate and tranilast monohydrate when crystallized by two solvent change spherical crystallization techniques. *Journal of pharmaceutical sciences*, *80*(5), 472-478.

44. Cavallari, C., Fini, A., & Pérez-Artacho Santos, B. (2013). Thermal study of anhydrous and hydrated forms of olanzapine. *Pharm Anal Acta*, *4*(237), 2.

45.Ha, J. M., Wolf, J. H., Hillmyer, M. A., & Ward, M. D. (2004). Polymorph selectivity under nanoscopic confinement. *Journal of the American Chemical Society*, *126*(11), 3382-3383.

46. Lee, A. Y., Lee, I. S., Dette, S. S., Boerner, J., & Myerson, A. S. (2005). Crystallization on confined engineered surfaces: A method to control crystal size and generate different polymorphs. *Journal of the American Chemical Society*, *127*(43), 14982-14983.

47.Beiner, M., Rengarajan, Pankaj, S., Enke, D., Steinhart, M. Manipulating the Crystalline State of Pharmaceuticals by Nanoconfinement. Nano Letters 2007, 7, 1381- 1385

48. Gibbs, J. W. (1961). *Scientific Papers: Thermodynamics* (Vol. 1). Dover Publications.

49. Paul J. Fischer,. (2008) Using Graphs of Gibbs Energy versus Temperature in General Chemistry Discussions of Phase Changes and Colligative Properties. *Journal of chemical education*, vol. 85, no 8, p. 1142.

50. Ricci, J. E. (1951). phase rule and heterogeneous equilibrium.

51. Coquerel, G. (2006). Thermodynamic predictions of physical properties–prediction of solid solutions in molecular solutes exhibiting polymorphism.*Chemical engineering & technology*, *29*(2), 182-186.

52. Patent US 125406A Improvement in drying and concentrating liquid substances by atomizing

53. Patel, R. P., Patel, M. P., &Suthar, A. M. (2009). Spray drying technology: an overview. *Indian Journal of Science and Technology*, *2*(10), 44-47.

54. Langrish, T. A. G., & Fletcher, D. F. (2001). Spray drying of food ingredients and applications of CFD in spray drying. *Chemical Engineering and Processing: Process Intensification*, *40*(4), 345-354.46

55. Broadhead, J., Edmond Rouan, S. K., & Rhodes, C. T. (1992). The spray drying of pharmaceuticals. *Drug Development and Industrial Pharmacy*, *18*(11-12), 1169-1206.

56. He, P., Davis, S. S., &Illum, L. (1999). Chitosan microspheres prepared by spray drying. *International journal of pharmaceutics*, *187*(1), 53-65.

57. Main, J. H., Clydesdale, F. M., & Francis, F. J. (1978). Spray drying anthocyanin concentrates for use as food colorants. *Journal of Food Science*,*43*(6), 1693-1694.

58. Chen, X. D., & Mujumdar, A. S. (Eds.). (2009). *Drying technologies in food processing*. John Wiley & Sons.

59. Sollohub, K., & Cal, K. (2010). Spray drying technique: II. Current applications in pharmaceutical technology. *Journal of pharmaceutical sciences*, *99*(2), 587-597.

60. Jain Manu, S., Lohare Ganesh, B., Bari Manoj, M., ChavanRandhir, B., BarhateShashikant, D., & Shah Chirag, B. (2011), Spray Drying in Pharmaceutical Industry: A Review. Research J. Pharma. Dosage Forms and Tech. Vol 4(2): 74-79

61. Nandiyanto, A. B. D., &Okuyama, K. (2011). Progress in developing spray-drying methods for the production of controlled morphology particles: from the nanometer to submicrometer size ranges. *Advanced Powder Technology*,*22*(1), 1-19.

62. Seville, P. C., Li, H. Y., &Learoyd, T. P. (2007). Spray-dried powders for pulmonary drug delivery. *Critical Reviews™ in Therapeutic Drug Carrier Systems*, *24*(4).

63.Chen, R., Tagawa, M., Hoshi, N., Ogura, T., Okamoto, H., &Danjo, K. (2004). Improved dissolution of an insoluble drug using a 4-fluid nozzle spray-drying technique. *Chemical and pharmaceutical bulletin*, *52*(9), 1066-1070.

64.Yi, T., Wan, J., Xu, H., & Yang, X. (2008). A new solid self-microemulsifying formulation prepared by spray-drying to improve the oral bioavailability of poorly water soluble drugs. *European Journal of Pharmaceutics and Biopharmaceutics*, *70*(2), 439-444.

65. Jung, J. Y., Yoo, S. D., Lee, S. H., Kim, K. H., Yoon, D. S., & Lee, K. H. (1999). Enhanced solubility and dissolution rate of itraconazole by a solid dispersion technique. *International journal of pharmaceutics*, *187*(2), 209-218.

66. Shen, S. C., Ng, W. K., Chia, L., Dong, Y. C., & Tan, R. B. (2010). Stabilized amorphous state of ibuprofen by co-spray drying with mesoporous SBA-15 to enhance dissolution properties. *Journal of pharmaceutical sciences*, *99*(4), 1997-2007.

67.IRé, M. (1998). Microencapsulation by spray drying. *Drying technology*, *16*(6), 1195-1236.

68.Krishnan, S., Kshirsagar, A. C., &Singhal, R. S. (2005). The use of gum arabic and modified starch in the microencapsulation of a food flavoring agent.*Carbohydrate Polymers*, *62*(4), 309-315.

69. Marmottant, P. Atomisation d'un liquide par un courant gazeux, PhD thesis, 2001, Institut National Polytechnique de Grenoble, France

70. Buckton G, Chidavaenzi O and Koosha F (2002) The effect of spray drying feed temperature and subsequent crystallization conditions on the physical form of lactose. AAPS Pharm. Sci. Tech. 3(4), 17.

71. Littringer, E. M., Mescher, A., Eckhard, S., Schröttner, H., Langes, C., Fries, M., &Urbanetz, N. A. (2012). Spray drying of mannitol as a drug carrier—the impact of process parameters on product properties. *Drying Technology*, *30*(1), 114-124.

72. Maa, Y. F., Costantino, H. R., Nguyen, P. A., & Hsu, C. C. (1997).The effect of operating and formulation variables on the morphology of spray-dried protein particles. *Pharmaceutical Development and Technology*, *2*(3),2

Chapter II

Pyrazinamide

II. 1. Introduction

Pyrazinamide (hereafter PZA) has long been recognized as an active drug against Mycobacterium Tuberculosis, a pathogenic bacterial species causing tuberculosis [(1)]. World health organization guidelines recommend the administration of PZA in association with two other drugs (rifampicin and isoniazid), in order to reduce bacterial growth during the initial phase of tuberculosis treatment [(2)]. The molecular structure of PZA is shown in Figure II.1.

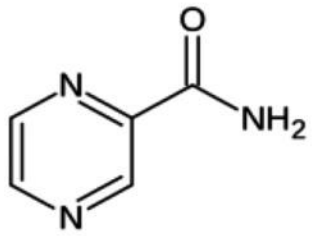

Figure II.1 molecular structure of Pyrazinamide

Given that various possibilities of intermolecular hydrogen bonds between PZA molecules can be established, different packing arrangements can exist. So far, four polymorphs have been reported namely: α, β, γ and δ [(3)].

α form (CSD reference code: PYRZIN) is referred to as the stable polymorph for a temperature higher than 25 °C. It is obtained by evaporation of a saturated solution of PZA in water at room temperature.

γ form (CSD reference code: PYRZIN05) is the stable form from 156 °C [(4)] or 145 °C [(3)] up to its melting at 188 °C. This high temperature form can be obtained by sublimation or freeze drying and it exhibits a structural disorder even at room temperature where it is metastable.

δ form (CSD reference code: PYRZIN02) is stable at low temperature and can be obtained by evaporation of a saturated solution of PZA in solvents such as tetrahydrofuran (THF), acetic acid at 4 °C.

β form (CSD reference code: PYRZIN01) has never been obtained as a structurally pure phase but always mixed with γ form.

A schematic representation of the relative stability of PZA polymorphs is represented in Figure II.2.

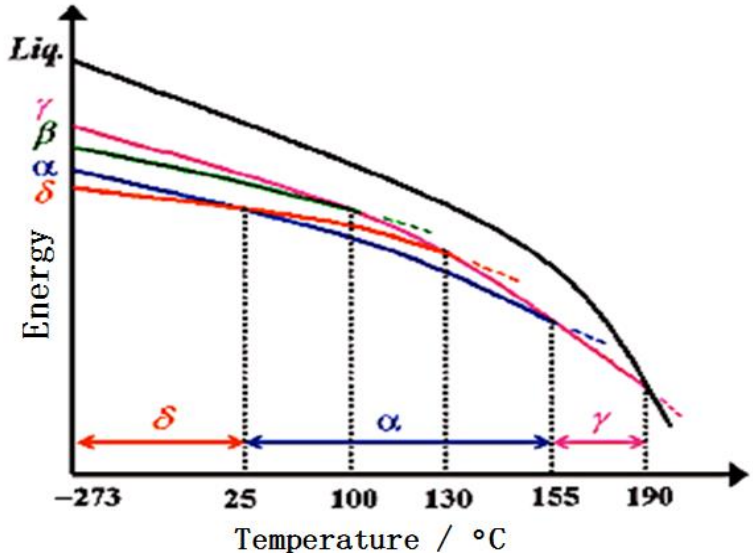

Figure II.2 Schematic representation of the relative stability of PZA polymorphs [(4)].

In their study, Cherukuvada et al. (2010) investigated phase transformation experiments of PZA; they found out that β, γ and δ forms tend to transform to α under the following conditions: ambient storage upon 6 months, polymorph seeding, solvent-mediated crystallization, neat and liquid assisted grinding [(4)]. Phase transformation experiments of PZA polymorphic forms are represented in a scheme in Figure II.3.

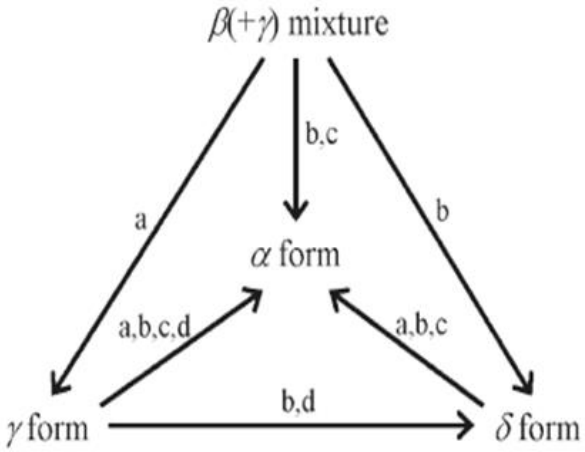

Figure II.3 Scheme representing phase transformation experiments of PZA polymorphic forms a) grinding of pure form b) grinding together with the seeds of the final form c) water assisted grinding of pure form d) storage for 6 months

The purpose of this chapter is to study the behaviour of PZA obtained by Spray Drying and the effect of the addition of excipients on the crystallization of PZA polymorphs by co-spray drying. In addition, we aim at finding appropriate excipients able to inhibit phase transition that can naturally occur upon ambient storage.

II.2 Study of PZA's behavior by Spray Drying

PZA was purchased from Sigma Aldrich and used without purification. X-ray analysis confirms that it refers to the stable α form. The experiments of Spray Drying of PZA were carried out in Buchi B-290 laboratory-scale mini spray dryer.

II.2.1 Solvents screening

This series of Spray Drying experiments was carried out with water and organic solvents including acetone and ethanol. The feedstocks are prepared by dissolving 0.5 g of PZA in 100 mL with of one of the listed solvents. The inlet temperature was set at 100 °C, the feed flow rate was set at 4 mL/min, the atomizing airflow rate at 473 L/h and the aspiration at 35 m^3/h. The open mode was selected for the experiment carried out with water whereas the closed mode was selected for experiments carried out with ethanol and acetone. The spray-dried powders were directly analysed by X-ray analysis. The diffraction patterns of spray-died PZA with water, ethanol and acetone with the inlet temperature set at 100 °C perfectly match the calculated diffraction pattern of the γ form of PZA with a crystallinity that seems to be lower with water (Fig.II.4).

Similar results were obtained by Spray Drying PZA with mixtures of solvents and water including acetone/ water 50/50 (v/v) (sample labelled SD-A) and ethanol/water with the exact parameters set above.

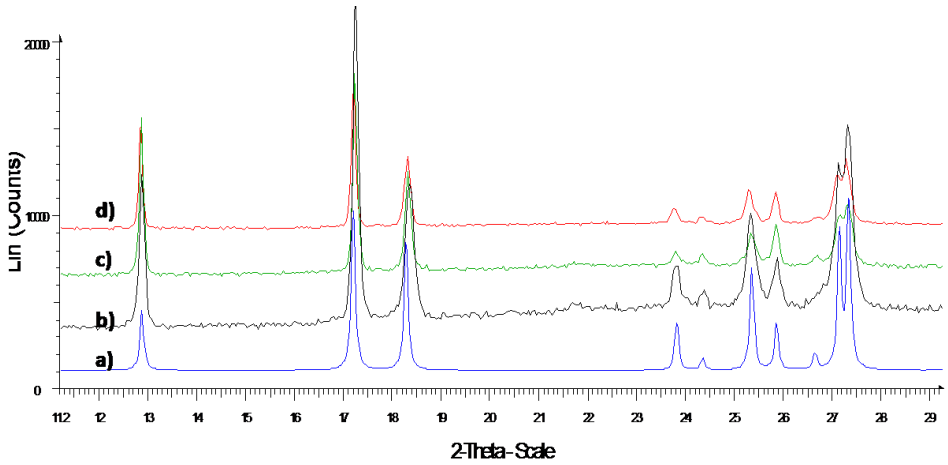

Figure II.4 Superimposition of a) the calculated pattern of γ form of PZA and the experimental XRPD patterns of spray-dried PZA obtained at T_{in}=100 °C with b) ethanol c) water d) acetone

II.2.2 Effect of the inlet temperature

The next series of experiments was performed by Spray Drying with an inlet temperature raised to 150 °C whereas all the other parameters including feed rate, gas flow, aspiration, concentration were kept constant.

X-ray diffraction patterns on the spray-dried samples, reveal characteristic peaks of γ form of PZA in addition to a shoulder (highlighted in grey) at 2θ = 27.6° referring to a characteristic peak of δ form of PZA (Fig.II.5).

By comparing this series of experiments to the ones performed in section II.2.1, it can be noticed that peaks are broader than products obtained with an inlet temperature fixed at 150 °C which means that the crystallinity is poorer than products obtained with an inlet temperature fixed at 150 °C. This can be a consequence of the too fast evaporation rate at 150 °C resulting in the crystallization of the metastable δ form.

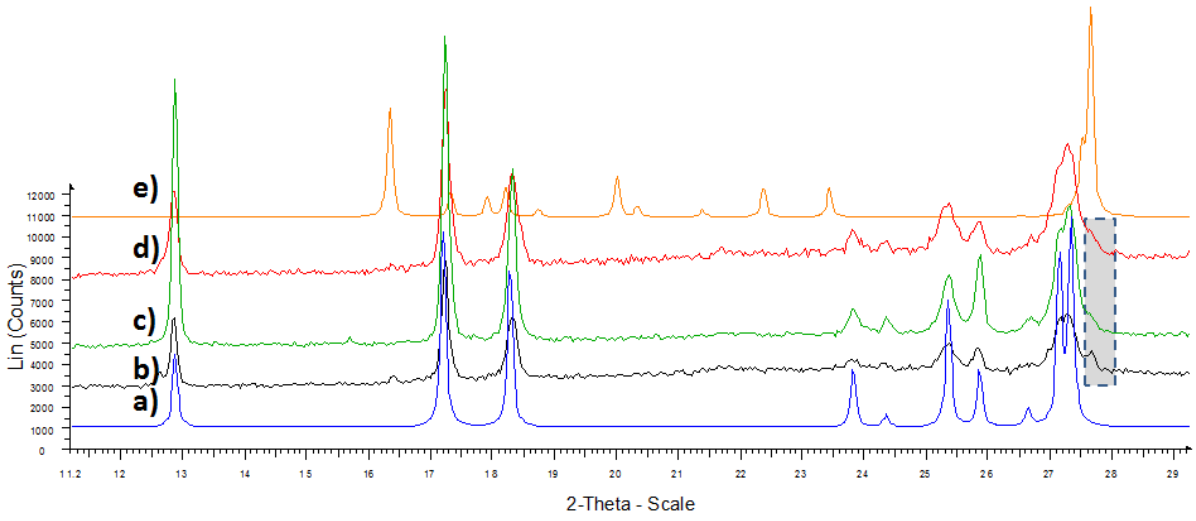

Figure II.5 Superimposition of the calculated patterns of a) γ form of PZA e) δ form of PZA and the experimental XRPD patterns of spray-dried PZA obtained at T_{in} = 150 °C with b) ethanol c) water d) acetone with δ form peak highlighted in grey

II.3 Characterization of spray-dried PZA

DSC analyses were performed on both commercial batch and sample SD-A. DSC thermogram shows that the commercial batch undergoes solid-solid phase transition at circa 147.5 °C corresponding to α→γ transition fairly close to the value in literature [3]. This phenomenon is followed by an endothermic peak with an onset temperature at 188 °C referring to the fusion of the γ polymorph (Fig.II.6.a).

Moreover, DSC analysis performed on fresh spray-dried PZA (SD-A sample) reveals only one endothermic event that can be ascribed to the fusion of the γ form with a T_{onset} at circa 188 °C (Fig.II.6.b).This confirms that γ form of PZA was successfully produced by means of spray drying and that there is no transition back to the α form during the heating at 5 K/min.

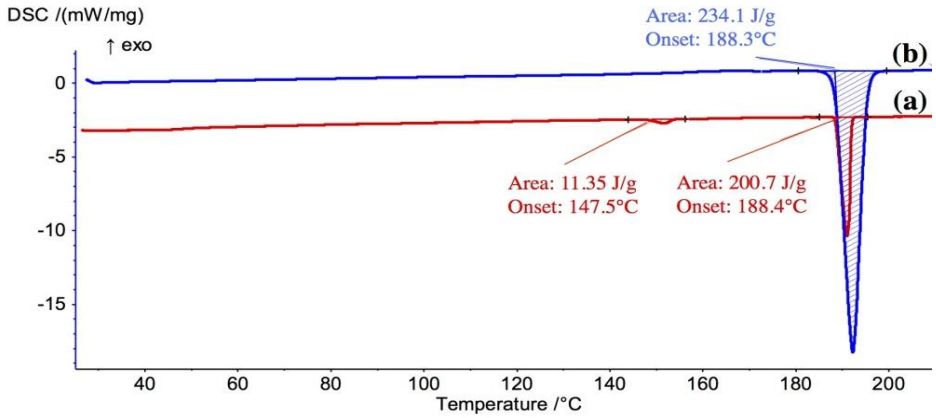

Figure II.6 DSC thermograms with a heating rate fixed at 5 K/min of (a) commercial PZA and (b) SD-A sample

II.4 X-ray follow-up of spray-dried PZA

Spray-dried SD-A sample was stored in a closed vial glass and was subjected to a daily monitoring by X-ray analysis. After 14 days of storage, additional peaks at 2θ equal to 9.11°, 27.7°, referring to δ form of PZA, were detected (Fig.II.7.b).

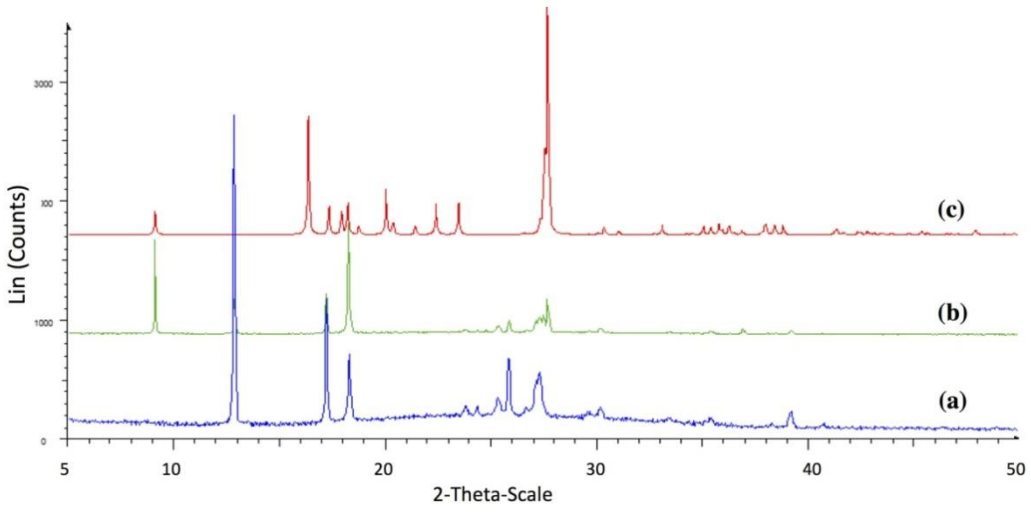

Figure II.7 Superimposition of the experimental XRPD patterns of spray-dried SD-A sample a) freshly obtained b) analyzed after 14 days of storage at room temperature and c) the calculated pattern of δ form of PZA.

II.5 Co-spray Drying PZA with Excipients

With the aim of preventing γ→δ form phase transition, it is desirable to add inhibitors like excipients in the spray drying process. According to generally held views, phase transitions are triggered at the surface or in the vicinity of defects. In fact, it is assumed that a flawed surface can easily induce a phase transition [(5)]. To overcome this problem, drug manufacturers seek out the stable form or efficient excipients able to inhibit phase transitions of a metastable form of an active ingredient [(6)]. Studies of active drug/excipient compatibility represent an important phase in the preformulation stage of the development of all pharmaceutical solids. It has been proven that the potential physical and chemical interactions between drugs and excipients can affect the chemical nature, the stability and bioavailability of drug. A study conducted with spray drying PZA resulted in the crystallization of δ form [(7)]. However, this form was unstable over time; the stability of the spray-dried PZA has extended from one to more than 4 weeks just after adding a list of excipients composed of hyaluronic acid in combination with dipalmitolphosphatidylcholine.

Pilcer and Amighi [(8)] have elaborated a list of excipients used in the formulation of marketed drugs for pulmonary inhalation. In reference to that list, excipients like glucose and D-mannitol were selected and added separately to the feed solution containing PZA and spray dried together. Given that the number of excipients approved by FDA for respiratory drug delivery is limited, we have also investigated other additives such as glycine, L-arginine, sodium chloride, urea and its derivatives: N-methylurea, 1,1-diethylurea, trimethylurea, lactose, citric acid and β-cyclodextrin. Experiments carried out by co-spray drying PZA with these excipients with the same conditions detailed in section II.2.1 were unsuccessful to prevent the transition of γ form of PZA. Indeed, X-ray analyses performed on the spray-dried samples have revealed peaks referring to α and/or δ forms of PZA after few days of storage at room temperature (Figures.II.8,9,10). Even by increasing the ratio excipient /PZA (w/w), the phase transition from γ form→α and/or δ forms couldn't be inhibited.

Co-spray drying PZA with glucose

Prior co-spray drying with PZA, glucose was spray dried solely. Figure II.8.a shows that spray drying glucose results in amorphous material revealing a halo by X-ray analysis. By co-spray drying PZA with glucose in the same experimental conditions, only peaks of PZA γ form are detected whereas glucose is amorphous (Fig.II.8.d). Hence, 7 days after storage at

room temperature, a phase transition γ to δ form of PZA was detected. Characteristic peaks of δ form of PZA are marked with arrows (Fig.II.8.e).

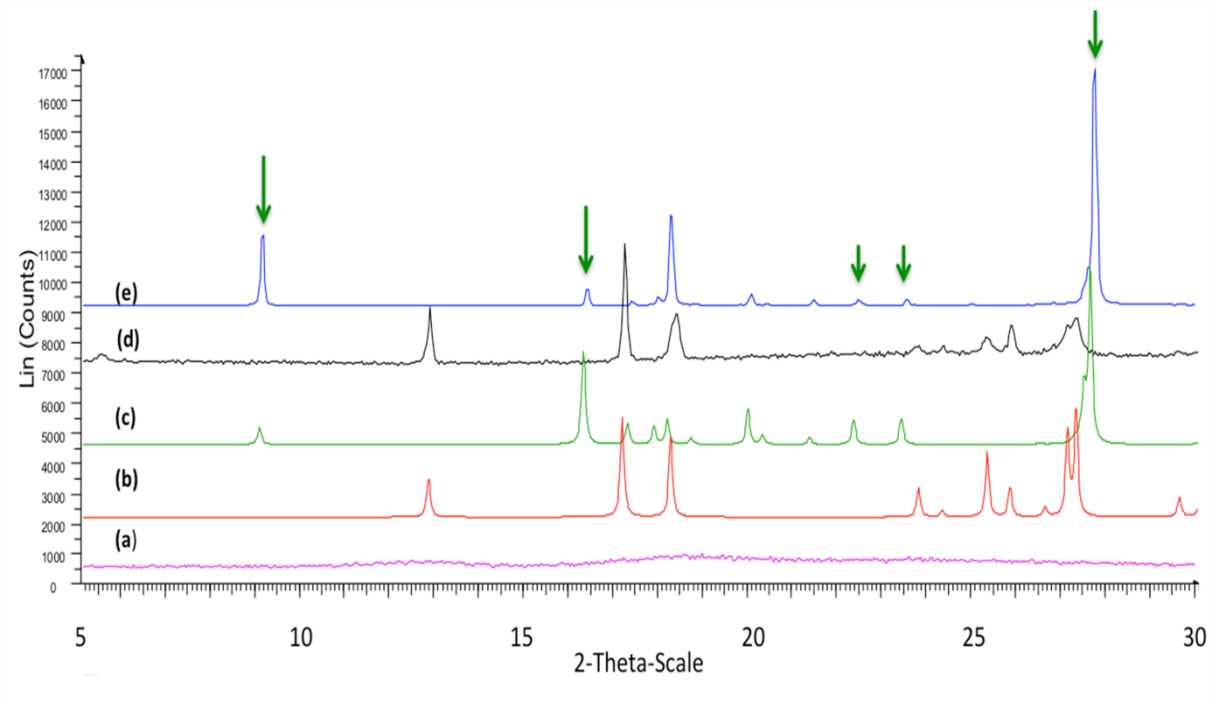

Figure II.8 Superimposition of a) experimental XRPD pattern of spray-dried Glucose and calculated XRPD patterns of b) γ PZA c) δ PZA and experimental XRPD patterns of co-spray-dried PZA + Glucose d) freshly obtained and e) analyzed after 7 days of storage at room temperature with arrows showing peaks of δ form of PZA

Co-spray drying PZA with urea

Co-spray drying PZA with urea resulted in the crystallization of γ form of PZA (Fig.II.9.e). However, a phase transition was detected after 10 days of storage: characteristic peaks of δ and α forms of PZA are marked with arrows (Fig.II.9.f).

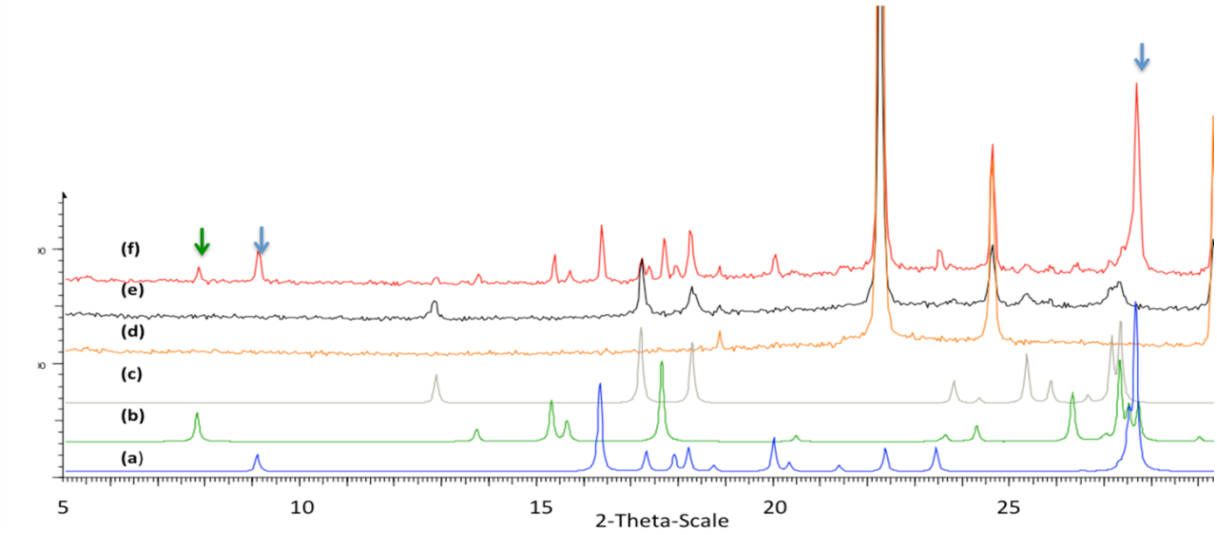

Figure II.9 Superimposition of calculated XRPD patterns of a) δ PZA b) α PZA c) γ PZA d) experimental XRPD pattern of commercial urea and experimental XRPD patterns of co-spray-dried PZA + urea e) freshly obtained f) analyzed after 10 days of storage at room temperature with arrows showing peaks of δ and α forms of PZA

Co-spray drying PZA with N-methylurea

Spray drying of N-methylurea solely resulted in the crystallization of a mixture of a new phase and stable form. Indeed, new peaks (highlighted in grey) appeared in Figure II.10.c. Hence, by co-spray drying PZA and N-methylurea, it results in the crystallization of γ PZA and the stable form of N-methylurea. The phase transition was detected after 1 month of storage.

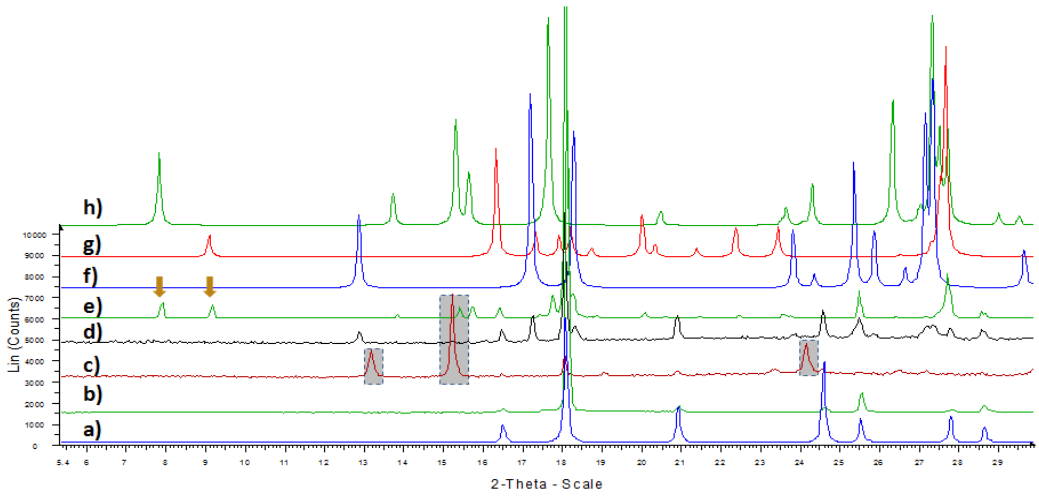

Figure II.10 Superimposition of calculated XRPD patterns of a) N-Methylurea f) PZA γ form g) PZA δ form h) PZA α form
experimental XRPD patterns of b) commercial N-Methylurea and c) spray-dried N-Methylurea with new peaks highlighted in grey and experimental XRPD patterns of co-spray-dried PZA + N-Methylurea d) freshly obtained e) analyzed after 1 month of storage at room temperature with arrows showing peaks of δ and α forms of PZA

The investigation of other urea derivatives was undertaken since by proceeding from urea to N-methylurea the isolation time of γ PZA increased from 10 days to 1 month. Among urea derivatives including: Trimethylurea, 1,1-diethylurea, only 1,3-dimethylurea presented an unique effect that will be further discussed. For this reason, supplementary tests were performed with two other excipients: 1,3-dimethylurea (hereafter DMU) and polyvinylpyrrolidone (hereafter PVP).

II.6 Co-spray Drying PZA with 1,3-Dimethylurea

DMU represented in Figure II.11 is an urea derivative used for the synthesis of caffeine, chemicals, textile aids, herbicides and others [(9)].

DMU exists as polymorph (I) stable at high temperature, crystallizing in *F*dd2 space group (CSD reference code NIJHUJ) with Z = 8, and as polymorph (II) stable at low temperature crystallizing in $P2_12_12$ space group (CSD reference code NIJHUJ02) [(10)], with Z = 2.

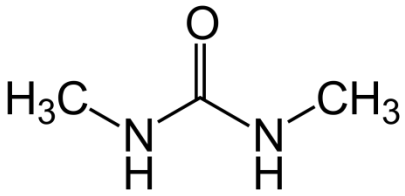

Figure II.11 Molecular structure of DMU

II.6.1 X-ray analysis of SD- PZA-DMU sample

A solution consisting of 0.5g of PZA and 0.5g of DMU was spray dried in 50/50 acetone/water with an inlet temperature set at 100 °C. The co-spray-dried sample (labelled hereafter SD-PZA-DMU) was analyzed by XRPD. The diffraction pattern of the freshly obtained SD-PZA-DMU sample exhibits peaks referring to both PZA (γ form) and DMU Form I (Fig.II.12.a-b-c). It excludes the formation of a co-crystal. Thus, the sample SD-PZA-DMU obtained by co-spray drying PZA and DMU is a physical mixture of γ form of PZA and DMU Form I.

SD-PZA-DMU sample was stored in a closed glass vial and subjected to an X-ray monitoring. It was observed that the γ form of PZA has remained unchanged up to 24 months of storage at room temperature (Fig.II.12.d).

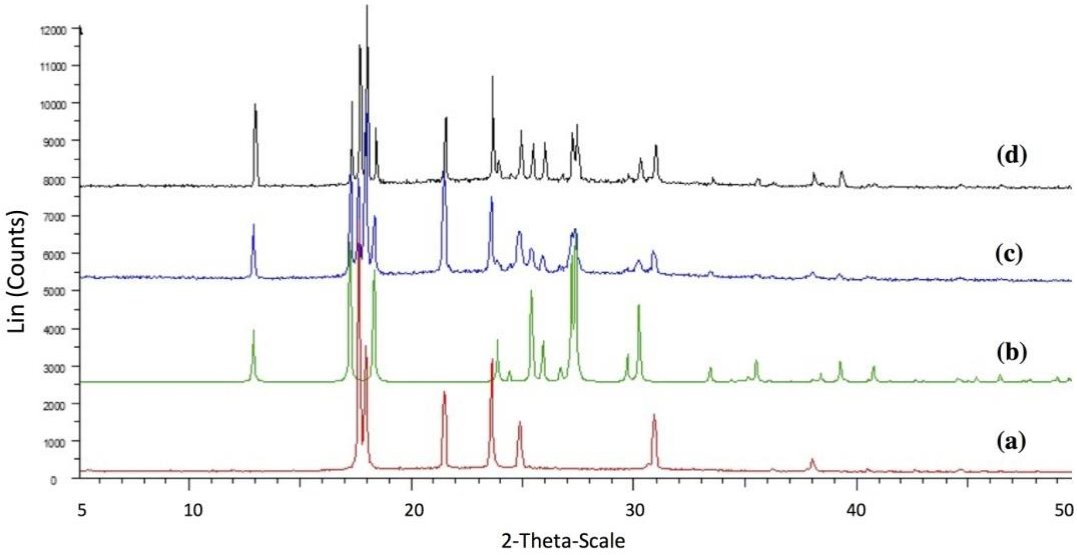

Figure II.12 Superimposition of calculated XRPD patterns of a) form I of DMU b) γ form of PZA and experimental XRPD patterns of SD-PZA-DMU sample c) freshly obtained (d) analyzed after 24 months of storage at room temperature.

It was quite interesting to evaluate whether DMU concentration has any impact on the phase inhibition process. For this reason, feed solutions with different concentrations of DMU were prepared ranging from 1 to 5g/L. It was observed that below 95/5 PZA/DMU (w/w), a phase transition was induced. Consequently, the threshold was estimated to be 95/5 PZA/DMU (w/w).

II. 6.2 Metastable binary phase diagram between PZA and DMU

Right after this observation, the hypothesis of the existence of partial solid solution was elaborated. In fact, previous studies related to the overturn of the order of polymorphs stability, showed that the addition of extra components can modify the landscape of polymorph stability via the formation of partial solid solutions [(11)]. However, no shift could be noticed at the high θ values between the XRPD pattern of γ form of PZA and the XRPD pattern of sample SD-PZA-DMU which is consistent with no partial solid solution.

Hence, the construction of metastable binary phase diagram between DMU Form I and γ PZA was an effective tool to confirm or reject this hypothesis. Accordingly, the compositions were prepared by manual grinding DMU form I and PZA γ form obtained by Spray Drying in an agate mortar at room temperature. The fusion heats of the systems as well as the eutectic temperatures were determined by differential scanning calorimetry (DSC) with a heating rate of 5 K/min. The experimental eutectic invariant temperature was found at 95.5 °C ± 0,75 °C

with a eutectic composition 85/15 DMU/PZA. Tammann graph is represented in red dashed lines plots the heats of fusion of the eutectic versus the composition expressed in weight percentage. Tammann graph shows an intersection with x axis at 0 from both sides of DMU form I (100%) and PZA γ form (100%) which confirms that no solid partial solution seems to exist (Fig.II.13). Consequently, the hypothesis of the existence of a surface effect and interaction between PZA and DMU seems consistent with the obtained results.

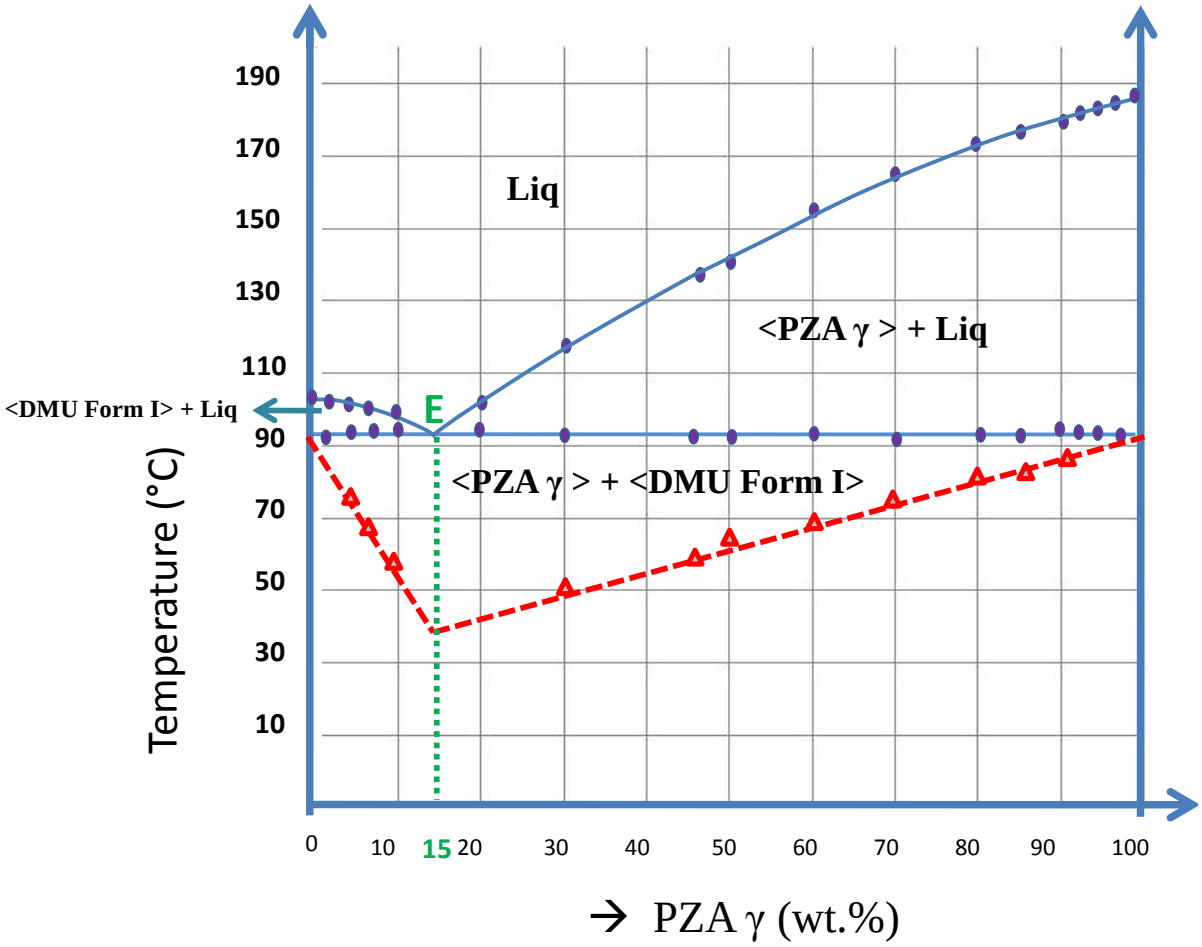

Figure II.13 Schematic metastable binary phase diagram between DMU Form I and PZA γ as function of mass percentage of PZA γ form and Tammann graph represented in red points

II.6.3 Plot of the ideal solubility curves of DMU and water

The depression of the melting point versus the mole fraction is given by the Schroeder Van Laar equation . The terms involving ΔC_p and the pressure can be neglected, so the expression is:

$$\text{Ln } x_A = \frac{\Delta H_A^f}{R}\left(\frac{1}{T_A^f} - \frac{1}{T^f}\right)$$

x_A stands for the molar fraction of <A>

T_A^f stands for the melting point of the pure compound <A> (expressed in Kelvin)

ΔH^f_A is the enthalpy of fusion of the pure compound <A>

R perfect gas constant 8.31 $J.mol^{-1}.K^{-1}$

T^f is the end of the fusion (Liquidus) expressed in Kelvin.

For the DMU compound: $\Delta H_{F\,DMU} = 12496\ J.mol^{-1}$. $T_{F\,DMU} = 378.7\ K$

For PZA compound: $\Delta H_{F\,PZA} = 28820\ J.mol^{-1}$. $T_{F\,PZA} = 461.3\ K$

The calculated values of liquidus temperatures versus mole fraction of water are represented in red points for DMU ideal solubility curve and in green points for PZA ideal solubility curve (Fig.II.14). The experimental points are represented in dark blue points.

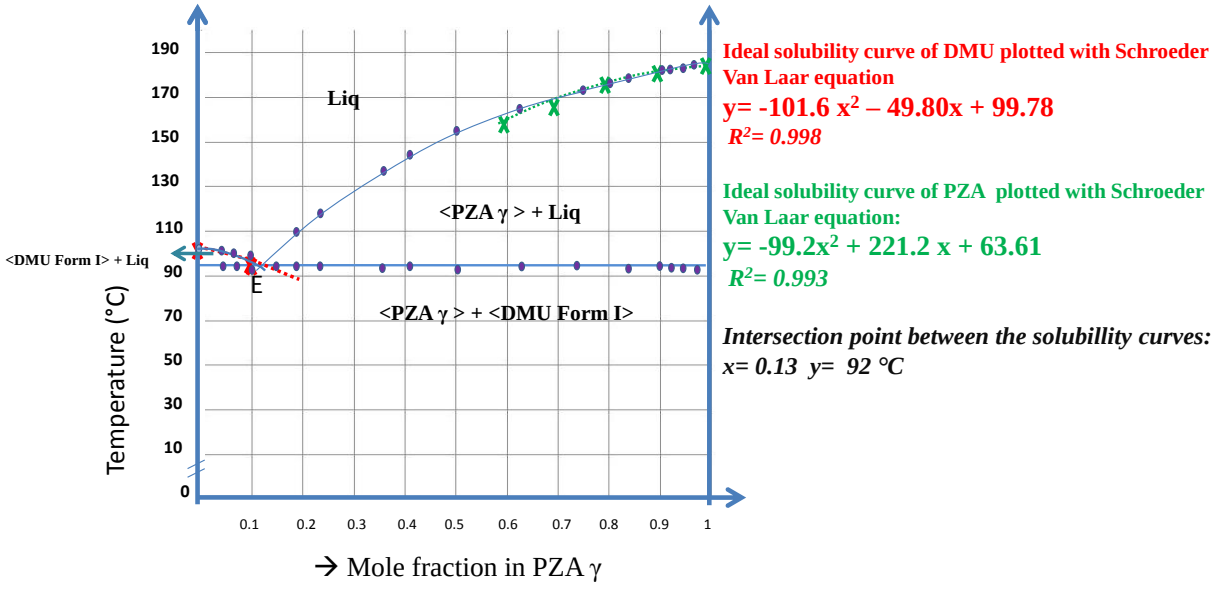

Figure II.14 Illustration of the binary phase diagram DMU-PZA versus mole fraction with the calculated solubility points of DMU (in red) and PZA (in green) given by Schroeder Van Laar equation and the experimental points (dark blue)

The ideal liquidus curve of PZA fits reasonably well down to 0.7 mole fraction in PZA form.

II.6.4 SEM images

Scanning electron micrographs of various spray-dried samples are presented in Figures II.15-16. Figure II.15 shows that SD-A sample referring to as γ form of PZA has irregular shapes with rough surfaces. Consequently, the roughness of these particle surfaces could facilitate the triggering of the irreversible phase transition: γ form → δ form of PZA observed few days after storage at room temperature. By contrast, when PZA was combined with DMU, the resulting particles labelled SD-PZA-DMU shows a modified morphology compared to the spray-dried compound SD-A. Figure II.16 shows that SD-PZA-DMU sample agglomerated

particles with well-faceted crystals, referring to as γ form of PZA, dispersed in a DMU Form I matrix. The mixture of these two compounds improved γ form of PZA in terms of shape and surface of the particles. Indeed, the concomitant crystallization of PZA and DMU seems to promote a better morphology of PZA single crystals. Therefore, the reduction of the surface defects of PZA might explain the inhibition of the phase transition γ → δ.

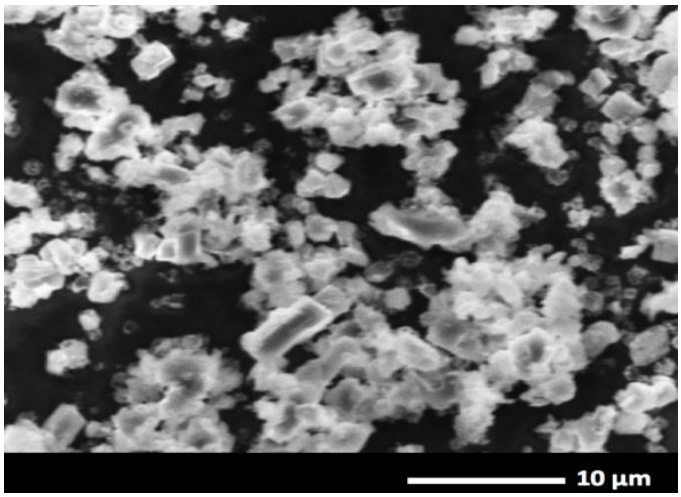

Figure II.15 SEM micrograph of spray dried PZA (γ form)

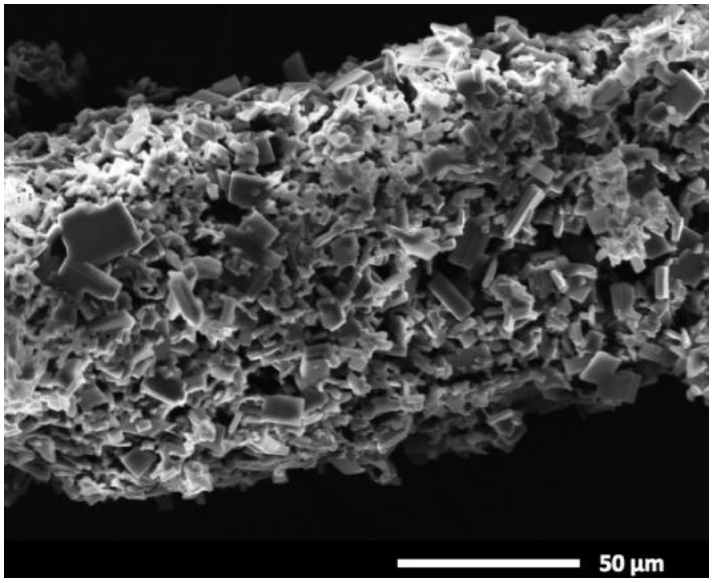

Figure II.16 SEM micrograph of SD-PZA-DMU (50/50 PZA/DMU w/w)

II. 6.5 Raman spectroscopy of SD-PZA-DMU sample

In order to examine the relative distribution of the two compounds PZA and DMU in SD-PZA-DMU sample, Raman mapping was used.

Prior to recording the Raman image, spectra of PZA γ form and DMU Form I were recorded in order to choose the better characteristic Raman bands for each compound (Fig.II.17.a). For a relevant mapping, it is recommended to choose Raman band of equivalent intensity and with no overlapping between the spectra of the compounds of interest (see enlargement of Fig.II.17.b). Thus, for DMU Form I, the 935cm^{-1} Raman band was chosen. It has been assigned to the symmetric stretching of the C-N bond coupled to the symmetric rocking of the CH_3 moieties [12] (ν_s C-N + ρ_s CH_3). For PZA γ form, the 1055cm^{-1} Raman band was chosen. It has been assigned to the in plane ring bending (δ ring).

The 2D spectral image was constructed in false colors (green for DMU form I and red for PZA γ) by calculating for each point of the mapped area the integral intensity of the Raman signal corresponding to the two selected Raman bands. On Figure II.18.a, it is visible that the PZA particles (of circa 5-15 µm diameter) are almost homogeneously dispersed among the DMU particles so as the two compounds are in close contact. This suggests that the stabilization of the PZA γ form could proceed from a surface effect. In other terms, DMU Form I particles or the nature and/or the distribution of defects thereby could inhibit the phase transition. Figure II.18.b shows a comparison between the reference spectrum of PZA γ and the spectrum of PZA extracted from the Raman image. The high similarity of the two spectra confirms that the PZA form involved in SD-PZA-DMU sample is PZA γ form. However, some remnant peaks of DMU (Form I) are observed in the spectrum extracted from the image suggesting (i) a deeper interpenetration of the two compounds or/and (ii) the detection of Raman signal coming from an adjacent particle (i.e. lateral spatial resolution was evaluated at circa 2µm and axial resolution at circa 10µm).

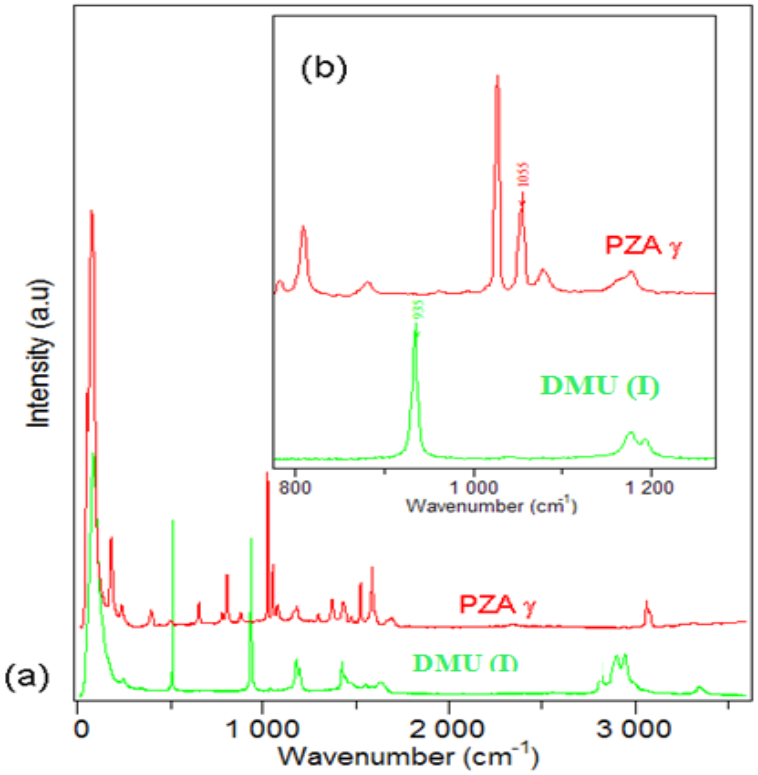

Figure II.17 (a) Raman spectra of DMU Form I (green) and PZA γ form (red); the inlet magnifies the region where are the chosen bands (1055cm^{-1} for PZA γ and 935cm^{-1} for DMU Form I)

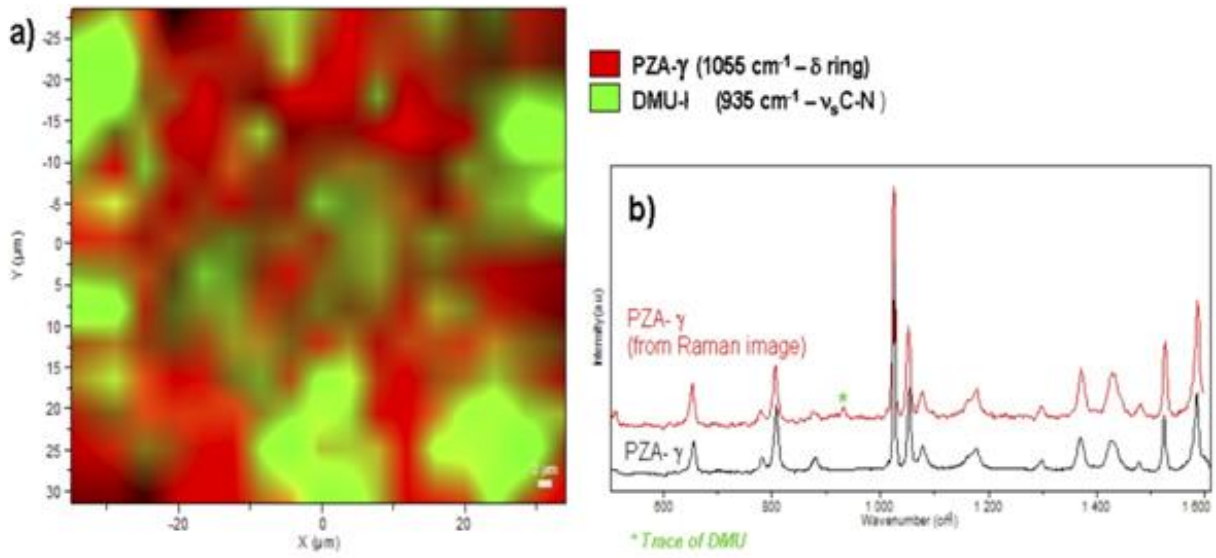

Figure II.18 (a) Raman mapping of SD-PZA-DMU sample; (b) comparison between the reference spectrum of PZA γ and the spectrum of PZA extracted from the Raman image.

II.7 Specificity of DMU Form I

It is worth mentioning that experiments carried out by manual co-grinding and with milling of PZA and DMU (Form I) revealed the same result as by co-spray drying.

It was also interesting to investigate the effect of DMU (II) on the inhibition of γ form of PZA. However, DMU (Form II) couldn't be obtained by Spray Drying. For this reason, PZA γ form and DMU (Form II) obtained by crystallization at low temperatures were submitted to manual co-grinding. Therefore, a transition was observed within several days.

A suggestion of a mechanism(s) by which DMU Form I has such a specific inhibition effect on the irreversible transition γ PZA was elaborated through an epitaxial relationship between the specific polymorphic forms of both compounds. Indeed, the epitaxial condition is surmised from the orientation of a specific face of a crystal that can be used as a substrate to control polymorph selectivity [13]. Accordingly, the interplanar distances between PZA Form γ and DMU (Form I and Form II) were compared for simple planes in the aim of finding similar interplanar distance (Table II.1 and Table II.2).

Table II.1 Comparison between interplanar distances of PZA γ and DMU (Form I)

PZA γ form Planes (h,k,l)	**d_{hkl} (Å)**	**DMU(Form I) Planes (h,k,l)**	**d_{hkl} (Å)**
001	10.3007	020	10.089
$\bar{1}01$	6.6783	030	6.7260
101	**5.0827**	**040**	**5.0445**
010	3.7291	310	3.7394
$\bar{2}01$	3.5875	131	3.5889

The comparison between the interplanar distances of PZA γ and DMU (Form I) reveals close values (Table II.1). One of the best matching distance between PZA γ form and DMU (Form I) is 5.08 Å referring to the planes (101) and (040) respectively. The epitaxial effect would occur at the interfaces between the primary molecular overlayer and the substrate [14]. For this reason, the planes involved in the illustration of the interface contact correspond to their respective perpendicular planes: $(10\bar{2})$ for PZA γ and $(00\bar{1})$ for DMU (Form I). The illustration of the epitaxial layers of PZA γ and DMU Form I is shown in Figure.II.19: DMU (Form I) molecules can be viewed as clips on PZA γ resulting in docking effect.

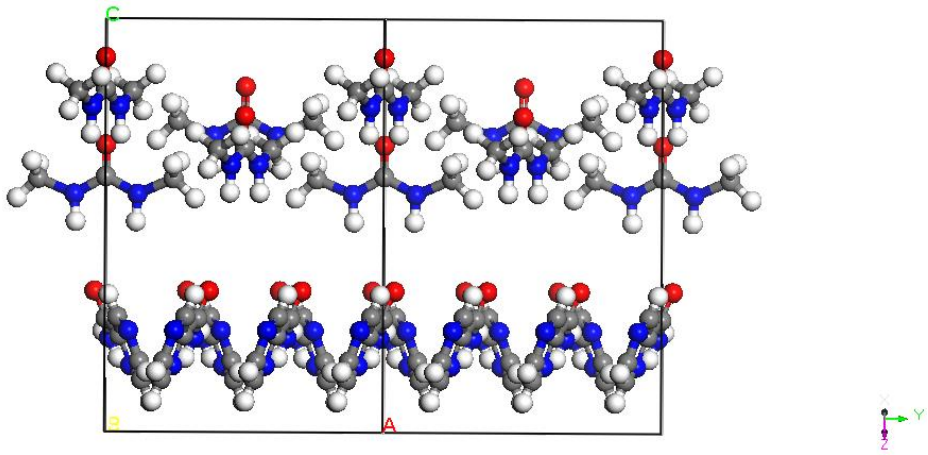

Figure II.19 Illustration of the hypothetical crystal structure built from the superimposition of PZA γ form plane (10$\bar{2}$) and DMU (Form I) plane (00$\bar{1}$).

Table II.2 Comparison between interplanar distances of PZA γ and DMU Form II

PZA γ form Planes (h,k,l)	**d_{hkl} (Å)**	**DMU(Form II) Planes (h,k,l)**	**d_{hkl} (Å)**
001	10.3007	100	10.754
010	**3.7291**	**210**	**3.7439**
$\bar{2}$01	3.5875	300	3.5847
011	3.5064	201	3.4940
200	3.4388	011	3.4486
110	3.2782	111	3.2839
$\bar{1}$12	2.9558	310	2.9543

One of the best matching interplanar distance between PZA γ and DMU Form II is at circa 3.72 Å corresponding to the planes (010) and (210) respectively. The planes involved in the illustration of the epitaxial effect are: (10$\bar{2}$) for PZA γ and (00$\bar{1}$) for DMU Form II. The corresponding illustration is shown in Figure II.20. This configuration might less favourable than the previous one with DMU Form I with regards to PZA-DMU hydrogen intermolecular interactions.

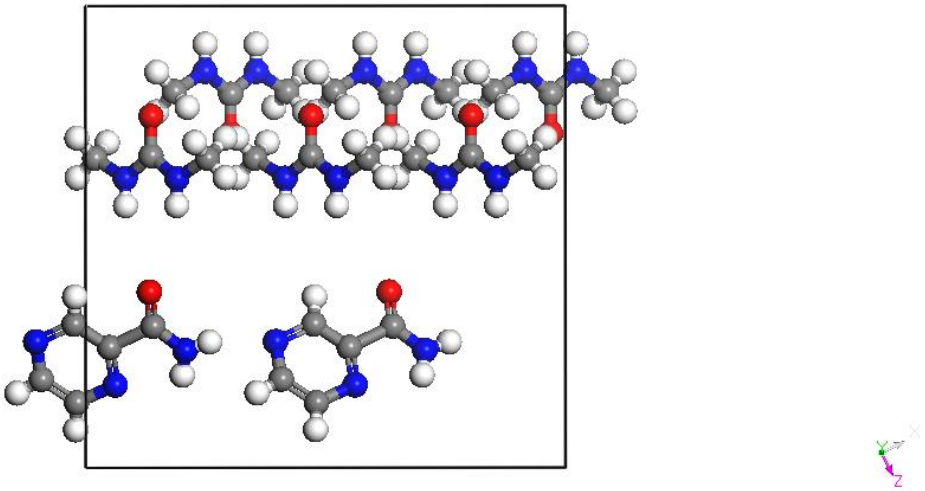

Figure II.20 Illustration of the hypothetical crystal structure built from the superimposition of PZA γ form plane ($10\bar{2}$) and DMU (Form II) plane ($00\bar{1}$).

The most direct approach for predicting epitaxial configurations involves total potential energy (PE) calculations [(14)]. Therefore, the lack of quantification of energy in the suggested models is a limiting factor that prevents getting a real approach for the prediction of an epitaxial configuration. On-going modelisation with softwares equipped with energy calculations will be in process. The modelisations presented above can be considered as a first approach to understand the specificity of the action of DMU (Form I) on PZA γ form. Besides, other aspects will be investigated: the bidimensional lattices and the coincidence of the non-centrosymmetric space groups of both compounds PZA γ and DMU (Form I and II).

II.8 Co-spray Drying PZA with PVP

PVP represented in Figure II.21 is an amorphous polymer widely used as excipient for the solid dosage forms. Many applications including its use as a binder in pharmaceutical tablets are reported in the literature[(15)]. Besides, the high value of its glass transition found at 163 °C, explains its ability to resist to relaxation and consequently its low probability to crystallize with time at room temperature. Therefore, storage at temperatures far below the glass transition is required to minimize the likelihood of recrystallization, and the higher the difference between storage temperature and the glass transition, the higher the stability of the amorphous phase. For these reasons, PVP could be a promising excipient for the present application involving a co-spray drying with PZA.

A solution consisting of 0.5g of PVP and 0.5g of PZA was spray dried in the same conditions detailed in section II.2.1.

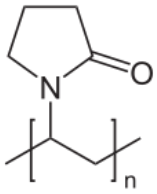

Figure II.21 Molecular structure of PVP

II. 8.1 X-ray analysis of SD- PZA-PVP sample

The co-spray-dried sample (labelled hereafter SD-PZA-PVP) was analyzed by XRPD.

The diffraction pattern of freshly obtained SD-PZA-PVP sample exhibits the peaks referring to δ form of PZA and a halo referring to the amorphous PVP (Fig.II.22)

SD-PZA-PVP sample was stored in a closed glass vial and subjected to an X-ray monitoring. It was observed that the δ form of PZA has remained unchanged up to 24 months of storage at room temperature (Fig.II.22).

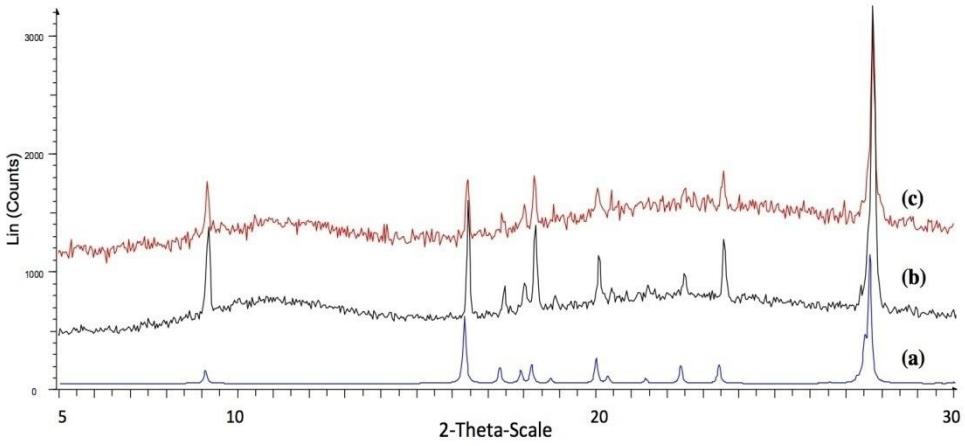

Figure II.22 Superimposition of a) calculated XRPD pattern of δ Form of PZA and experimental XRPD pattern of SD-PZA-PVP sample b) freshly obtained c) analyzed after 24 months of storage.

PVP was then found to be highly effective in the crystallization of δ form PZA and the prevention of any phase solid –solid transition.

Additionally, feed solutions with different concentrations of PVP were prepared ranging from 1 to 5g/L. It was found that from a mixture 5/95 PVP/PZA (w/w)up to 45/55 PVP/PZA (w/w), a mixture of γ+δ forms of PZA was obtained. Starting from a mixture of 50/50 PVP/PZA (w/w) up to 95/5 PVP/PZA (w/w), δ form of PZA was obtained structurally pure by co-spray drying with PVP (as far as XRPD can tell).

II.8.2 Raman spectroscopy of SD-PZA-PVP sample

The relative distribution of the two compounds PZA and PVP in SD-PZA-PVP sample was studied by Raman spectroscopy. For PVP, the 935cm^{-1} Raman band was chosen. It has been assigned to the out-of-plane rings C–H bending [16]. PZA δ form structurally pure was obtained by the protocol described by Takaki et al. [17] .The 1055cm^{-1} Raman band was chosen for PZA δ form coinciding by chance with the same value of Raman band chosen for PZA γ form (Fig.II.23.a-b). Prior Raman analyses, the structural purity of these forms is confirmed with the support of X-ray analyses.

The 2D spectral image was constructed in false colors (green for PVP and red for PZA δ form (Fig.II.24-a). The sample presents similarities with the SD-PZA-DMU sample as it is visible that the PZA particles (of circa 5-10 µm diameter) are almost homogeneously dispersed among the PVP particles. Figure II.24.b shows a comparison between the reference spectrum of PZA δ form and the spectrum of PZA extracted from the Raman image. The high similarity of the two spectra confirms that the PZA form involved in SD-PZA-PVP sample is PZA δ form.

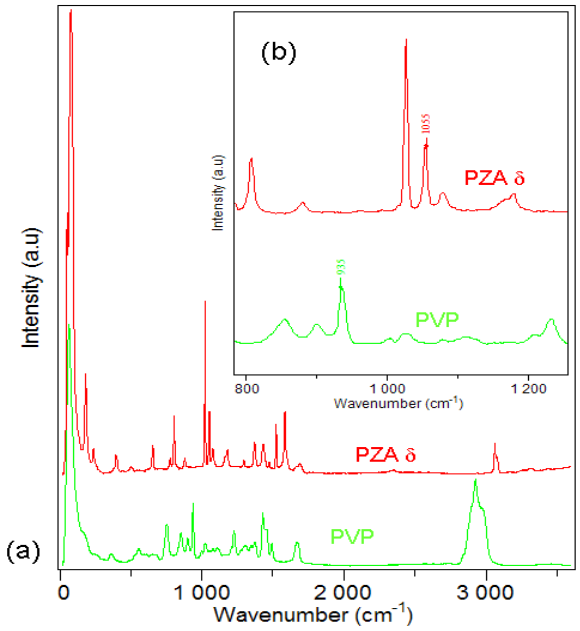

Figure II.23. (a) Raman spectra of PVP (green) and PZA δ (red); the inlet magnifies the region where are the chosen bands (1055cm^{-1} for PZA δ form and 935cm^{-1} for PVP).

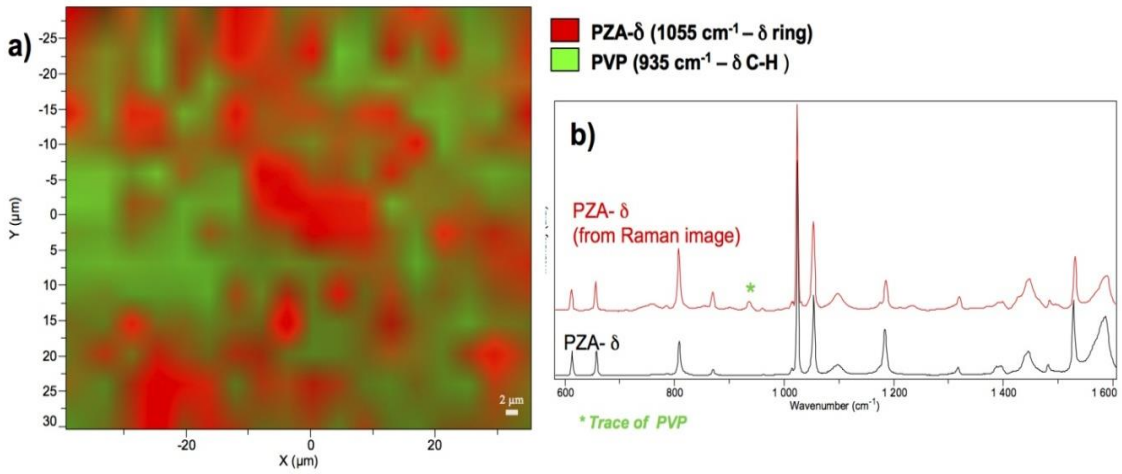

Figure II.24. (a) Raman mapping of SD-PZA-PVP sample, (b) comparison between the reference spectrum of PZA δ form and the spectrum extracted from the Raman image.

II.9. Conclusion

The influence of the addition of excipients on the crystallization behavior of PZA has been investigated by using co-spray drying. The experiments carried out with a dozen of different excipients proved that DMU Form I is, so far, the only component able to prevent the solid phase transition from γ PZA to δ form at room temperature. With the support of X-ray monitoring, it was found that only 5% in mass of DMU (with reference to PZA) dissolved in the feed solution is enough to block the metastable γ form for at least 24 months. The construction of the metastable binary phase diagram between γ PZA and DMU Form I shows that there is no domain of miscibility in the solid state. SEM micrographs showed that the co-spray-dried sample of γ PZA with DMU Form I has regular well-defined crystals with smooth surfaces. Besides, confocal Raman spectroscopy evidenced that every PZA particle is surrounded by particles of DMU Form I. Consequently, specific action on the surface is surmised. In addition to smooth surfaces of PZA crystals, the close contact between the two compounds might be an additional factor in the inhibition of the phase transition. Therefore, DMU form II didn't provide the same effect: a solid-solid transition of γ form of PZA was observed after few days of storage. We can conclude that there is a specificity of the compound (DMU) and the Form I. Moreover, a co-spray drying experiment carried out with PVP resulted in the crystallization of δ form of PZA. The physical mixture remained unchanged over 24 months of storage at room temperature [(18)]. In conclusion, the addition of an appropriate excipient is a key step for a successful formulation extending the life span of an API metastable form.

REFERENCES

1.Zhang, Y., Mitchison , D., (2003).The curious characteristics of Pyrazinamide Int. J. Tuberc. Lung Dis., 7, pp. 6–21

2.Maher, D., Chaulet, P., Spinaci, S., Harries, A., (1997). Treatment of tuberculosis: Guidelines for national programs, World Health Organization, Geneva.

3.Castro, R. A.E., Maria, T. M.R., Évora, A.O.L., Feiteira, J. C., Silva, M. R., Beja, A. M., Canotilho, J.,Eusébio, M. E. S., (2010).A new insight into pyrazinamide polymorphic forms and their thermodynamic relationships, Cryst. Growth & Des,10,pp. 274–282.

4.Cherukuvada, S., Thakuria, R., and Nangia, A., (2010).Pyrazinamide Polymorphs: Relative Stability and Vibrational Spectroscopy,Cryst. Growth & Des,10,pp. 3931–3941.

5. Ewen, B., Strobl, G.R., Richter D.,(1980). Phase transitions in crystals of chain molecules. Relation between defect structures and molecular motion in the four modifications of n-$C_{33}H_{68}$ Faraday Discuss. Chem. Soc, 69, pp.19-31

6.Airaksinen, S1., Karjalainen, M.,Kivikero, N., Westermarck, S., Shevchenko, A., Rantanen, J., Yliruusi, J.,(2005). Excipient selection can significantly affect solid-state phase transformation in formulation during wet granulation AAPS PharmSciTech, 6(2),E.311-E322

7. Pham, D-D.,Fattal, E., Ghermani, N., Guiblin, N., Tsapis, N., (2013). Formulation of pyrazinamide-loaded large porous particles for the pulmonary route: avoiding crystal growth using excipients Int J of Pharmaceutics ,454 (2),pp.668-677

8. Pilcer, G., Amighi, K., (2010). Formulation strategy and use of excipients in pulmonary drug delivery Int J Pharm ,392, pp.1-19.

9.SIDS Initial Assessment Report for SIAM 17 11–14 November 2003, Arona, Italyhttp://www.inchem.org/documents/sids/sids/96311.pdf

10.Näther C1., Döring C.,Jess I., Jones., PG., Taouss C.,(2013).Thermodynamic and structural relationships between the two polymorphs of 1,3-dimethylurea ActaCryst. 69, pp.70–76

11. Coquerel, G., (2006) Thermodynamic predictions of physical properties - Prediction of solid solutions in molecular solutes exhibiting polymorphism. Chem. Eng. Technol., 29, (2), pp.182-186.

12. Martins, D., Spanswick, C., Middlemiss, D., Abbas, N., Pulham, C., Morrison, C.; 2009. A new polymorph of N,N'-Dimethylurea characterized by X-ray diffraction and first-principles lattice dynamics calculations J. Phys.Chem. A,113(20), pp.5998–6003.

13. Mitchell, C. A., Yu, L., Ward, M. D. (2001). Selective nucleation and discovery of organic polymorphs through epitaxy with single crystal substrates.*Journal of the American Chemical Society*, *123*(44), 10830-10839.

14. Last, J. A., Hooks, D. E., Hillier, A. C., Ward, M. D. (1999). The physicochemical origins of coincident epitaxy in molecular overlayers: Lattice modeling vs potential energy calculations. *The Journal of Physical Chemistry B*, *103*(32), 6723-6733.

15. Volker, B., 2005.Polyvinylpyrrolidone Excipients for Pharmaceuticals: Povidone, Crospovidone and Copovidone. Berlin, Heidelberg, New York: Springer. pp. 1–254

16.Wu, K.H., Wang Y.R.,Hwu W.H., 2003. FTIR and TGA studies of poly(4-vinylpyridine-co-divinylbenzene)–Cu(II) complex, PolymerDegradation and Stability, 79, pp.195-200.

17. Takaki, Y., Sasada, Y., and Watanabé, T.,1960.The crystal structure of α pyrazinamide ActaCryst, 13, pp. 693-702

18. Baaklini, G., Dupray, V., & Coquerel, G. (2015). Inhibition of the spontaneous polymorphic transition of pyrazinamide γ form at room temperature by co-spray drying with 1, 3-dimethylurea. *International journal of pharmaceutics*, *479*(1), 163-170.

Chapter III

1,3-Dimethylurea

III.1 Introduction

A literature review on 1,3-dimethylurea (hereafter DMU) indicates that this molecule crystallizes in two enantropically-related polymorphic forms[(1)], named Form I and Form II; where Form I is the stable polymorph at high temperature, its space group is uncommon *F*dd2 (refcodes: NIJHUJ01 & 03 – occurrence 0.3% in the CSD) and Form II is the stable form at low temperature, its space group is $P2_12_12$ (refcodes: NIJHUJ02 & 04). Nevertheless, the solid-solid transition temperature between both forms remained unclear. Indeed, it was observed at 41 °C by DSC analysis, but was also observed at -20 °C [(1)].

For this reason, it is worthwhile to reinvestigate the solid-solid transition of DMU and to establish its value more accurately. Moreover, knowing that DMU has a strong interaction with water [(2)], it is possible that water influences the temperature of the solid-solid transition as in the ammonium nitrate-water system[(3)]. For this purpose, it is interesting to study the binary system: DMU-Water and to determine the nature of equilibria associated to the solid-solid transition of DMU forms with water and to investigate the behavior of DMU by Spray Drying.

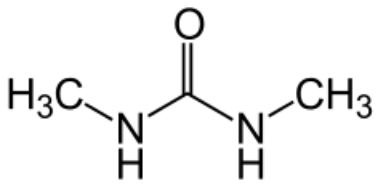

Figure III.1 Molecular structure of DMU

III.2 Behavior of DMU in Spray Drying

III.2.1 Behavior of DMU in Spray Drying with water and organic solvents at T_{in}= 100 °C

Feed solutions were prepared by dissolving 1g of DMU in 40 mL in water, methanol, ethanol and acetone. Spray Drying experiments were carried out with a feed flow rate at 4 mL/min, an atomizing airflow rate at 473 L/h, aspiration at 35 m^3/h, inlet temperatures fixed at 100 °C; the outlet temperatures recorded were 43 °C for spray drying test carried out with aqueous solution test and 60 °C for spray drying tests carried out with organic solvents. The open mode was selected for the aqueous solution whereas the close mode was selected for the solutions with organic solvents. X-ray analyses performed on spray-dried DMU are illustrated in Figure III.2: the XRPD patterns of the four experiments reveal peaks corresponding to the

Form I structurally pure. The yield was estimated at 70% for the experiments carried out with organic solvents and it was estimated at 10% for the experiment carried with water. In fact, due to the hygroscopicity of DMU, the powder sticks on the wall of the cyclone resulting in the decrease of the yield while operating with water.

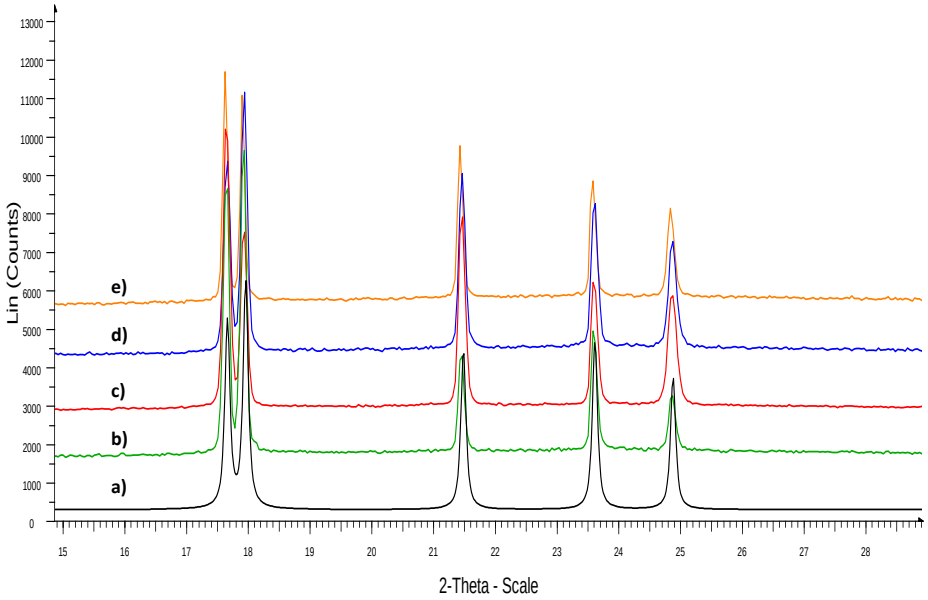

Figure III.2 Superimposition of a) calculated XRPD patterns of DMU form I and experimental XRPD patterns of spray-dried DMU at T_{in}=100 °C with b) methanol c) ethanol d) acetone e) water

III.2.2 Effect of the inlet temperature

In this series of experiments, the same concentration of DMU was prepared with methanol, ethanol and acetone. The inlet temperature was decreased from 100 °C to 60 °C. The oulet temperature recorded was 40 °C.

Figure III.3 illustrates the experimental XRPD patterns of the spray-dried samples.

Despite the decrease of the inlet temperature, Form I is obtained solely. It is mainly due to the outlet temperature located above the solid-solid transition temperature at 40 °C. The ideal case was to optimize Spray Drying parameters in order to get an outlet temperature below the solid-solid transition Form II → Form I. Therefore, the inlet temperature couldn't be set below 60 °C since an efficient drying is required.

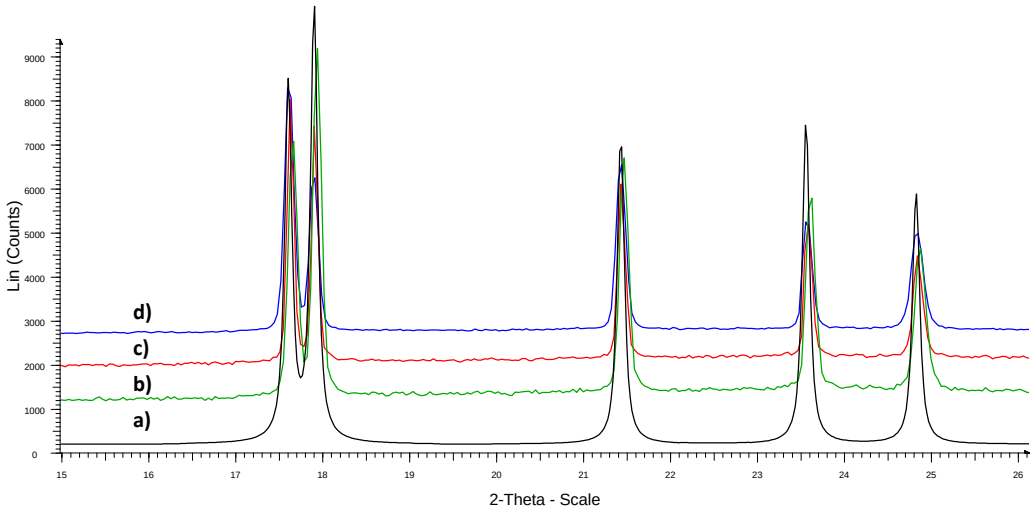

Figure III.3 Superimposition of a) calculated XRPD patterns of DMU form I and experimental XRPD patterns of spray-dried DMU with T_{in}= 60 °C with b) methanol c) ethanol d) acetone

III.3 Characterization of DMU

III.3.1 DVS analysis on the commercial form

DVS analysis performed on commercial DMU (mixture of Form I and Form II) shows that from 0% to 58% RH a steady baseline is established revealing no change in mass. (Fig.III.4). When the humidity of the system was raised to 58%, the sample began to gain mass rapidly. Thus, the critical relative humidity (RH_c) for DMU where deliquescence occurs is estimated between 59% and 69 % at 25 °C. Upon increasing the RH above RH_c, the sample starts dissolving until forming an unsaturated solution. The desorption profile reveals a continuous decrease in the mass until reaching a plateau (30% in mass change)upon RH decrease from 40 to 0%. The sample retrieved from DVS analysis was not dry, indeed, it looked like a gel. This observation explains the reason why the desorption is not reversible.

Based on the DVS moisture/desorption profile of DMU, it can be deduced that this compound has a strong affinity with water leading to its deliquescence at a defined relative humidity and temperature. For this reason, precautions were taken into account during the storage and manipulation: the sample was dried in a desiccator over P_2O_5 prior use to avoid as much as possible its interaction with water from the atmosphere.

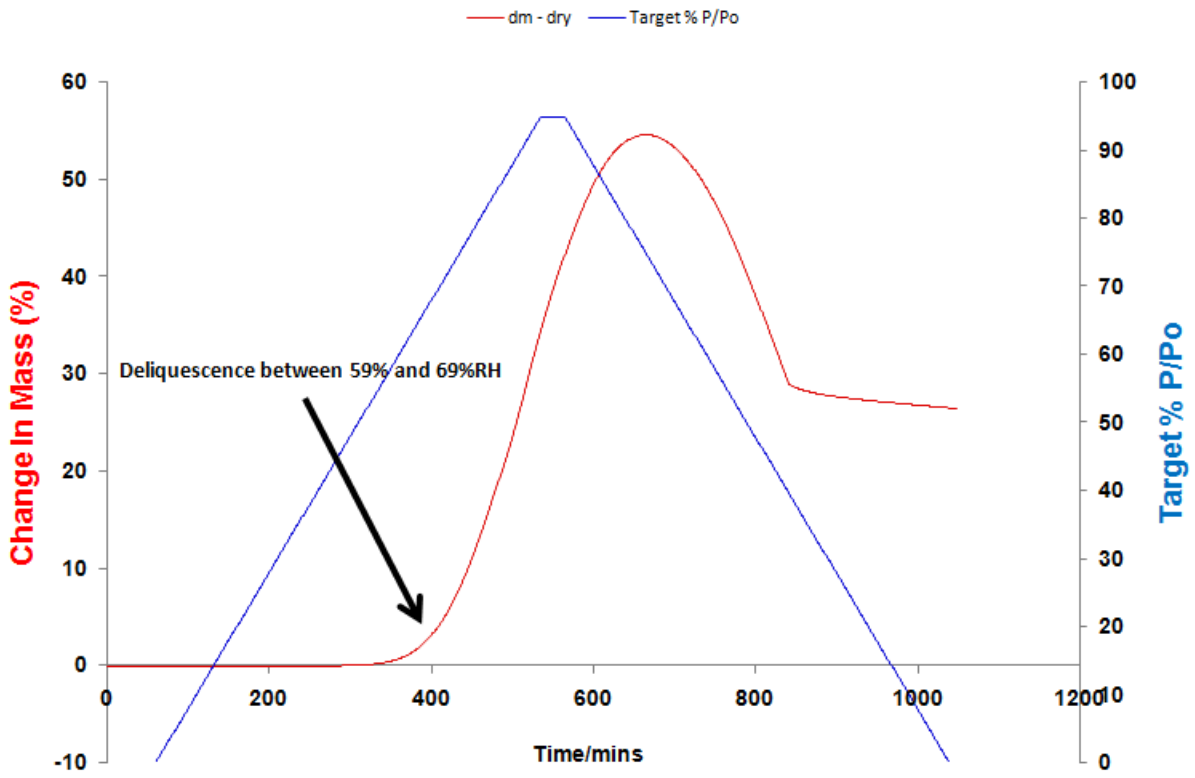

Figure III.4 DVS analysis on the commercial DMU at 25 °C

III.3.2 TR-X-Ray analysis of Form II

Form II was obtained by preparing a suspension of the commercial batch of DMU in n-heptane. The suspension was stirred for 24 hours in a cold room at 4 °C and filtered at the same temperature.

Form II was placed on a sample holder and analyzed by TR-X-Ray powder diffraction. At 22 °C (RH circa 60%), the XRPD corresponds to Form II with the characteristic peaks pointed with arrows (Fig.III.5.a). When the temperature reaches 30 °C (RH circa 32%), characteristic peaks of Form I indicated by asterisks appear (Fig.III.5.b). Therefore, the solid-solid transition Form II towards Form I occurs between 22 °C and 30 °C. At 40 °C (RH circa 20%), the transition is completed and the XRPD depicts a pattern of structurally pure Form I with characteristic peaks indicated by asterisks (Fig.III.5.c).

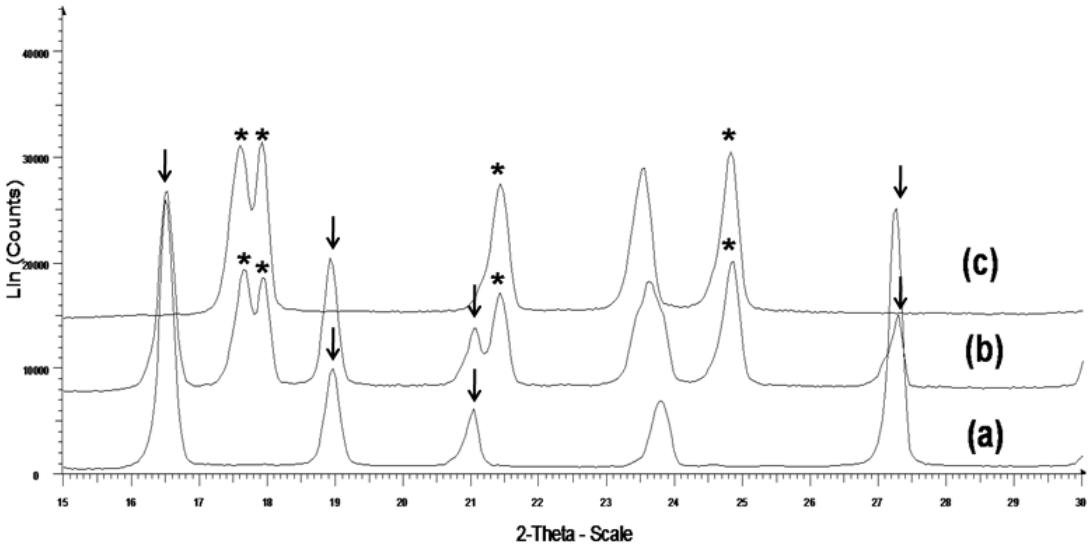

Figure III.5 Superimposition of TR-XRPD patterns of DMU (a) at 22 °C (b) at 30 °C (c) at 40 °C with the characteristic peaks of Form I indicated by asterisks and the characteristic peaks of Form II indicated by arrows.

III.3.3 DSC analysis on Form II

DSC analysis was performed on Form II that was placed in a crucible with a pierced lid with a heating rate fixed at 5 K/min. The DSC thermogram (Fig.III.6) shows that Form II undergoes the solid–solid phase transition at circa 41.2 °C. This temperature is in agreement with the DSC onset temperature found in literature [(1)]. This phenomenon is followed by an endothermic peak with an onset temperature at 105.7 °C referring to the melting of Form I.

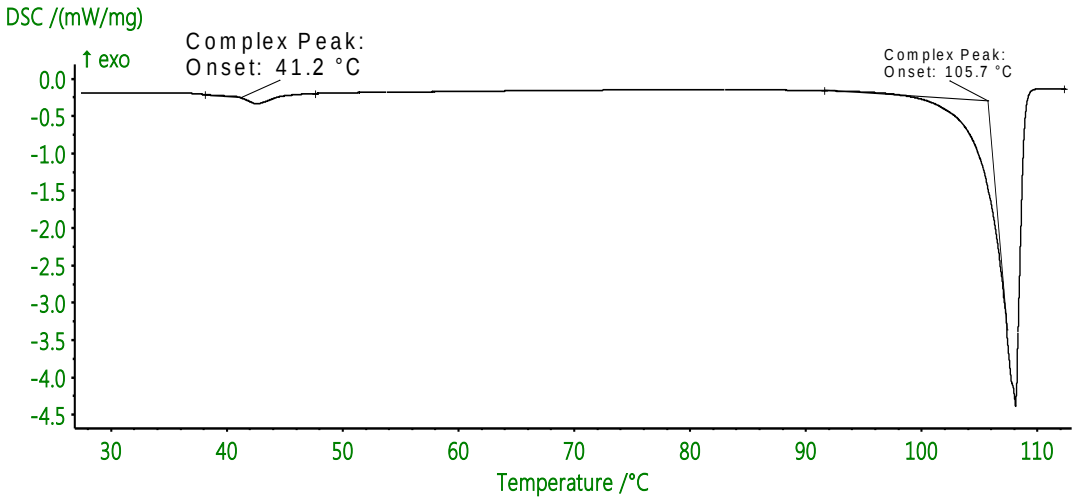

Figure III.6 DSC analysis of DMU Form II

Thus, DSC and TR-X-ray analyses performed on Form II display different values for the same solid-solid transition temperature. Further investigations were then necessary to understand this discrepancy. In fact, all along the DSC analysis, the RH is controlled by the nitrogen flow and supposed to be close to 0%. In contrast, when the TR-X Ray analyses were performed, no nitrogen flux was used, so the powder might have easily adsorbed water and the solid-solid transition temperature would rather decrease following a metatectic equilibrium associated to the solid-solid transition of DMU with water.

III.4 *In- situ* X-Ray analyses

In-situ X-Ray analyses [(4)] were performed on 7g of Form II in suspension with 80 mL n-heptane with different amount of water (Fig.III.7).

Figure III.7.a represents an *in-situ* X-ray analysis performed on DMU in suspension with n-heptane dried with molecular sieve. The amount of water in the dried n-heptane was determined by Karl Fischer titration and was found at 40 ppm of water.
Estimation of the amount of water in the reactor containing 7g of DMU in 80 mL of n-heptane dried with molecular sieve:
$V_{heptane}$= 80 mL; ρ= 0.6795 g/ mL ; $m_{heptane}$ = ρx V = 0.6795 x 80 = 54.36 g
(54.36 x 40) / 7 = 310 ppm which corresponds to 0.03 % water (wt), corresponding to 0.15 % molar in water.
At this composition, the solid-solid transition from Form II to Form I is detected at 28 °C. The domain of co-existence ssI + ssII relies between 28 °C and 42 °C. In reference to DSC analysis, the solid-solid transition Form II → Form I was found at 41 °C. Thus, when the system contains 0.15% molar in water, the solid-solid transition decreases from for 41 °C to 28 °C.

Figure III.7.b illustrates an *in-situ* X-ray analysis performed on DMU in suspension with n-heptane saturated in water. The amount of water in the n-heptane saturated in water was found at 98 ppm of water by Karl Fischer titration. The same formula applied above gives a value equal to 775 ppm of water inside the reactor which corresponds to 0.39 % molar in water. At this composition, the solid-solid transition from Form II to Form I is detected at 24 °C. The domain of co-existence ssI + ssII relies between 24 °C and 36 °C.

A last *in-situ* X-ray analysis was performed by adding 200 microliters to the reactor. Thus, the solid-solid transition from Form II to Form I was found at 26 °C. No domain of co-existence ssI + ssII is present: only peaks of structurally pure Form I and XRPD patterns of structurally pure Form II are detected (Fig.III.7.c)**.** The volume of added water in this experiment corresponds to 12% in molar percentage of water in the reactor.

In light of these results, it can be deduced that the addition of water results in the decrease of the solid-solid transition following metatectic equilibrium. When the molar percentage in water in the reactor was increased from 0.15 % to 0.39%, the lower limit of the co-existence domain of the two forms decreased from 28 °C down to 24°C. Hence the metatectic invariant is likely to be at 25 °C ± 1 °C.

Table III.1 summarizes the values of $T_{r\ II \rightarrow I}$ (°C) and the boundaries of the domain of co-existence ssI + ssII as function of water amount in the reactor expressed in molar percentage in water.

Table III.1 Relevant data obtained by *in-situ* X-Ray analyses as function of molar percentage in water

Water (molar %)	$Tr_{II \rightarrow I}$ (°C)	Boundaries of the domain of co-existence ssI + ssII
0.15	28 ± 2	28→ 42 °C
0.39	24 ± 2	24→ 36 °C
12	26 ± 2	No domain of co-existence

a)

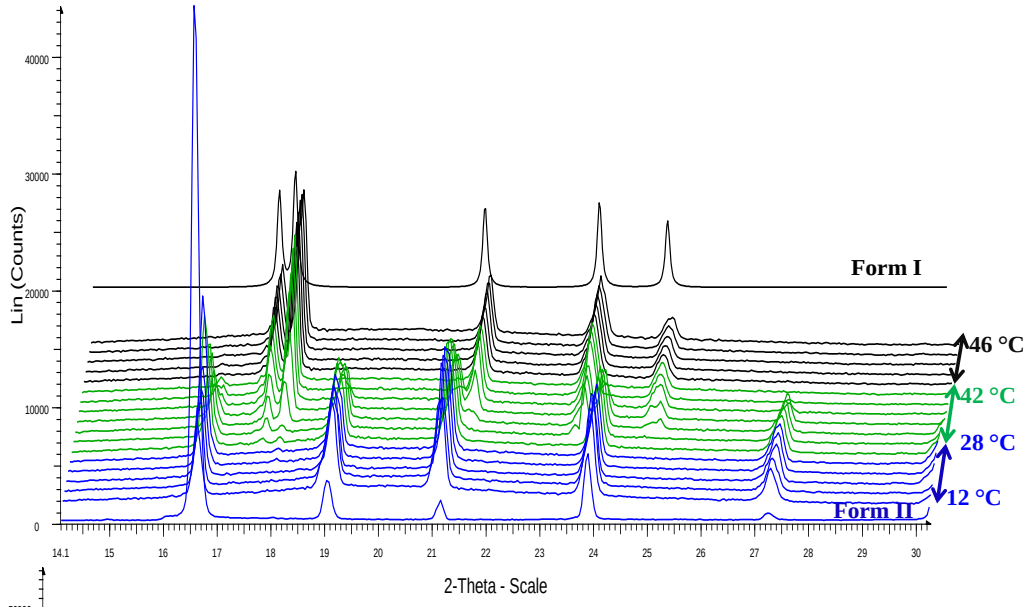

b)

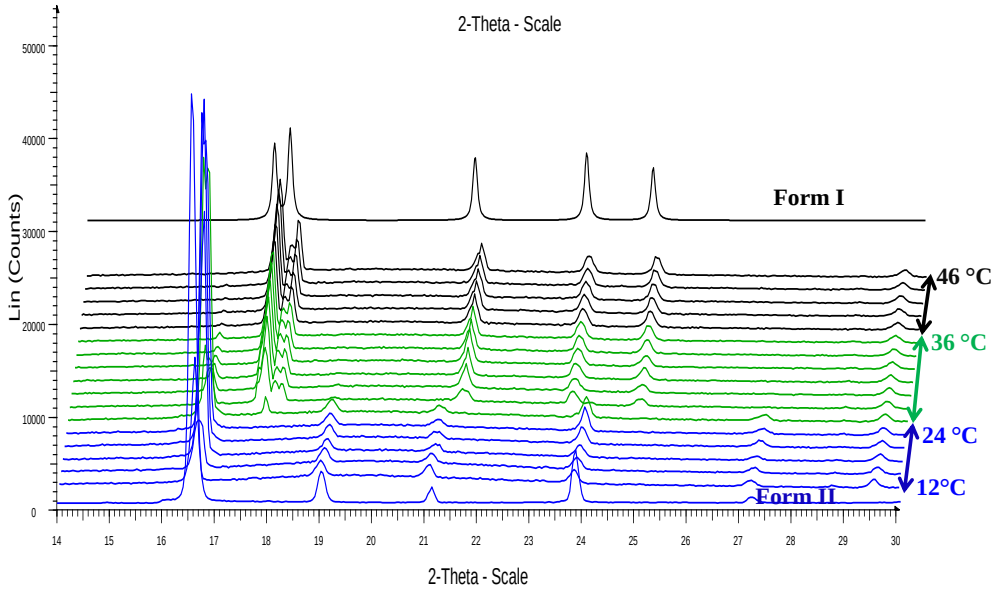

c)

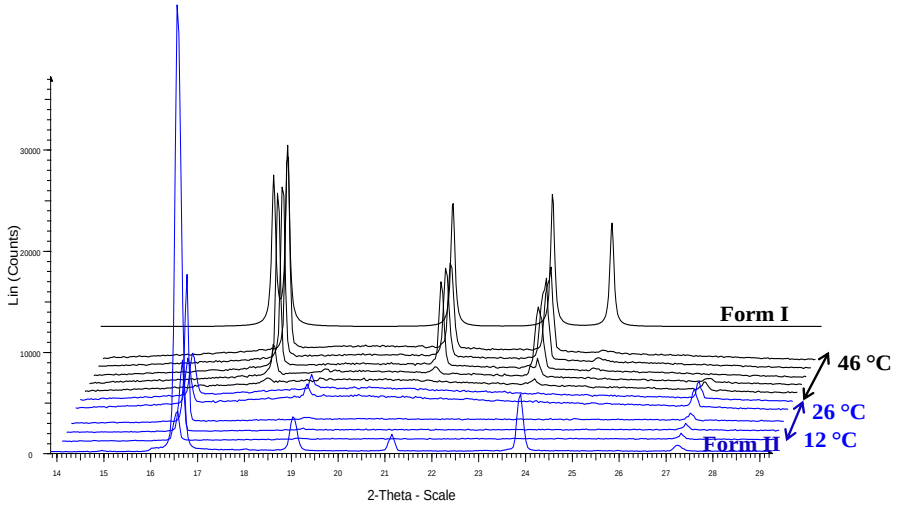

Figure III.7 *In-situ* X-Ray analyses of DMU in suspension with n-heptane with different molar percentage of water: a) 0.15 % b) 0.39% c) 12%
The experimental XRPD patterns of Form II are represented in blue.
The experimental XRPD patterns of Form I are represented in black.
The experimental XRPD patterns illustrating the domain of co-existence ssI+ ssII are represented in green.

III.5 DSC analyses of closed crucibles enriched with water

Crucibles containing commercial DMU (dried in a desiccator over P_2O_5 prior use) were placed in a desiccator at 20 °C with a saturated salt solution of sodium chloride to control the RH (75% at 20 °C). DMU samples were then enriched in water. The percentage of water absorbed in each powder was determined by weighing accurately the crucible before and after storage in the desiccator. Furthermore, after this conditioning, crucibles were hermetically sealed with lids in order to keep the amount of water constant all along DSC analyses. The crucibles containing DMU/water mixtures with various compositions were analyzed by DSC in a temperature range starting at -70 °C and ending at 120 °C at 5 K/min.

The first DSC analyses (Fig.III.8) revealed a complex behavior with several overlapping phenomena:

- an endotherm located at circa -37 °C directly followed by an exothermic phenomenon (recrystallization). Hence, this endotherm would likely belong to a metastable equilibrium.
- an endotherm at -20 °C can be assigned to the presence of eutectic between a hydrate and ice. However, its presence (or another invariant at a very close temperature) for compositions lower than 50% molar in water could be due to a metastable hydrate not yet defined.
- a third endotherm located at circa 8 °C whose maximum heat exchange for 50% mol. It is likely that this invariant corresponds to the non-congruent fusion of a hydrate.
- a fourth endotherm located at different temperatures corresponding to the end of fusion of the solid solution.

In order to get closer to equilibrium, an annealing at -10 °C for two hours was performed for each composition in DSC. Examples of DSC heating curves before and after annealing representing the metastable and stable equilibria are shown in Figure III.8 and Figure III.9 respectively.

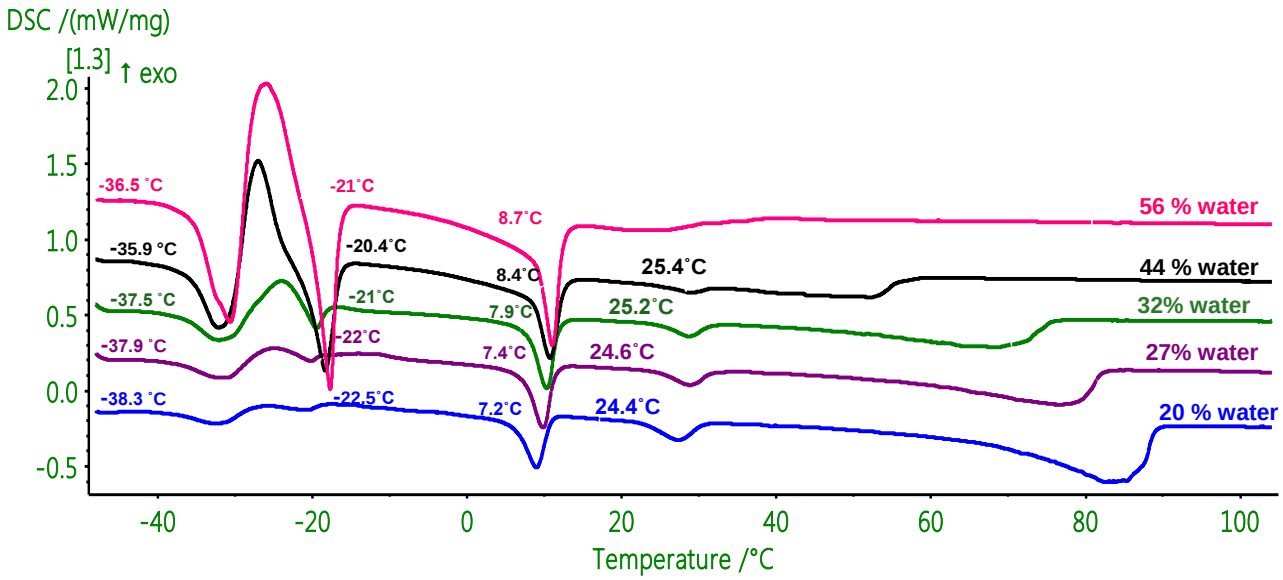

Figure III.8 DSC curves of mixtures of various compositions in water before annealing at -10 °C (expressed in molar % of water)

After annealing, for the composition 42% molar of water, only the peritectic invariant (7.8 °C), the solid-solid transition at circa 25 °C and the liquidus (58 °C) were recorded.

By contrast, for the compositions 52 and 58% molar of water, stable eutectic invariants are present at circa -22 °C, followed by the peritetic invariant, the solid-solid transition at circa 25 °C and finally the liquidus.

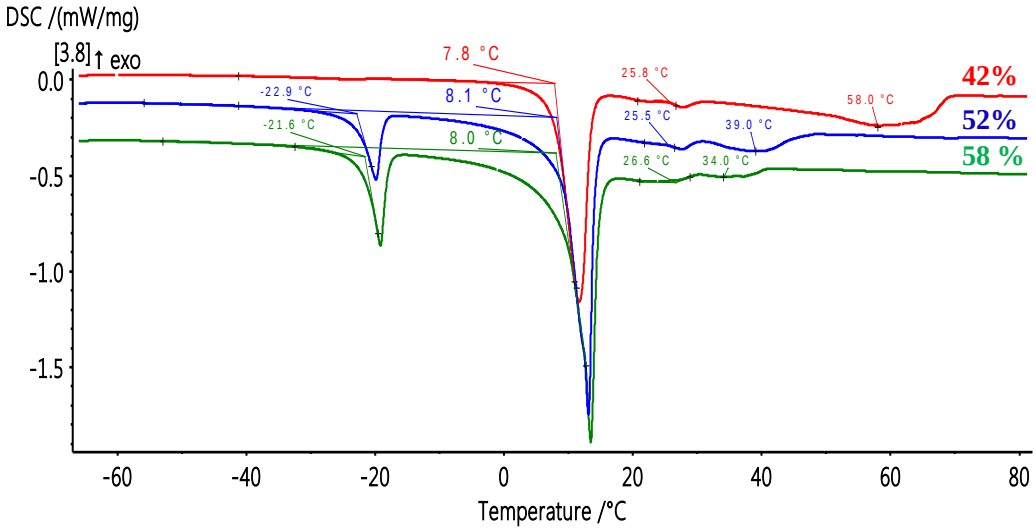

Figure III.9 DSC curves of mixtures of various compositions in water after annealing at -10 °C (expressed in molar % of water)

III.6 Tammann graph

The stoichiometry of the hydrate DMU:water (1:1) was confirmed by the construction Tammann graph: the heats of fusion of peritectic invariant were plotted versus water composition in mass percentage (Fig.III.10).

The experimental points served to find the composition with the highest heat of fusion of the peritectic referring to the hydrate composition. This composition was found at 16.55 % (%wt in water) corresponding to 49.26 % molar in water fairly close to 50% which confirms that the hydrate stoichiometry is: DMU water (1:1).

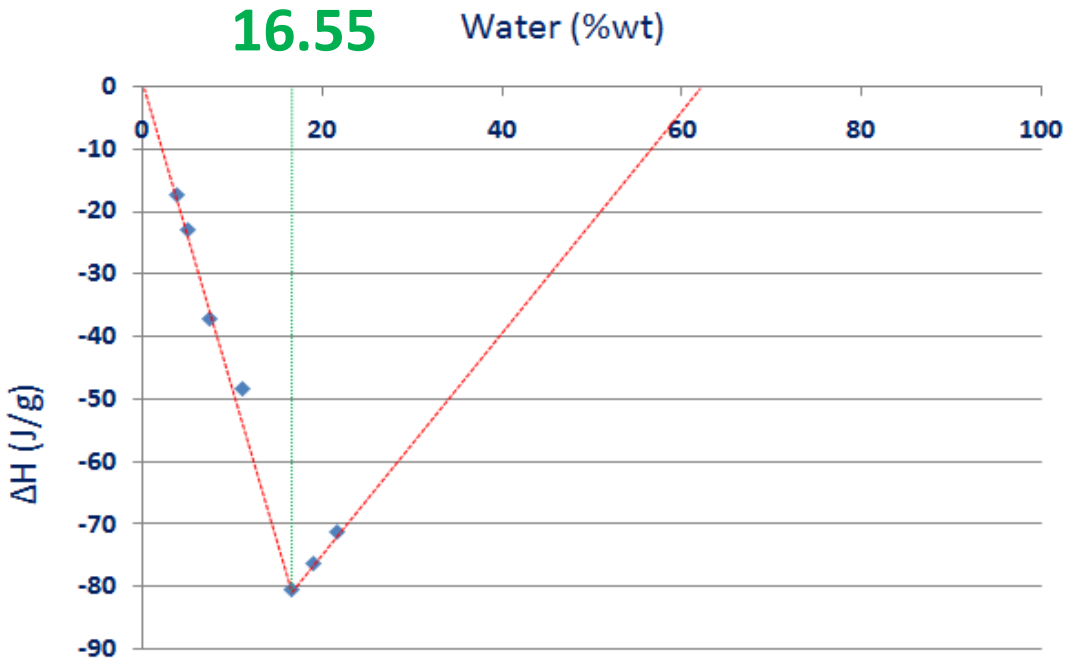

Figure III.10 Tammann graph of the peritectic invariant

III.7 Spectroscopic identification of a new phase: a monohydrate of DMU

In order to crystallize the suspected monohydrate at low temperature, a solution of DMU with 60% molar of water was prepared and placed in the freezer (-18 °C) for 4 hours then stored in a room at 4 °C for 15 days. Sample preparation for X-ray analysis was performed in a cold room storage so that the temperature of the sample remained below the peritectic invariant located at circa 8 °C. The sample was immediately analyzed by TR-XRPD at -25 °C.

The results confirmed the hypotheses extracted from DSC measurements. Interestingly, at -25 °C, a new XRPD with characteristic peaks at 22.5° and 25.5° in 2θ appear in addition to some peaks of hexagonal ice pointed with arrows at 16° and 23° in 2θ (Fig.III.11).

The XRPD pattern is assigned to the DMU monohydrate. When the sample was heated till -15 °C, peaks of the ice disappeared; hence, only peaks of the monohydrate remain. At 11 °C, above the peritectic transition, Form II appears with its characteristic peaks which is consistent with DSC analysis where the peritectic invariant is located at circa 8 °C.

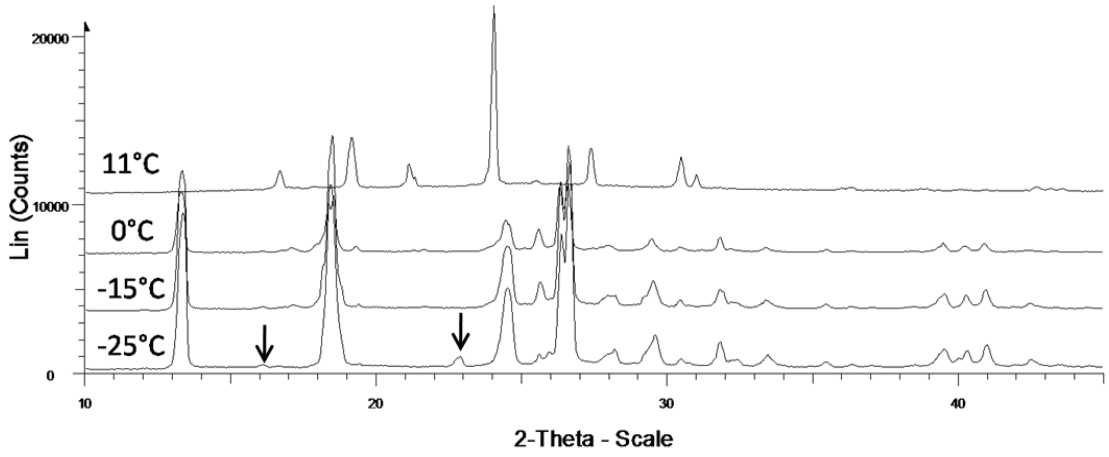

Figure III.11 TR-X-ray patterns of the DMU-water with 60% molar at different temperatures with the characteristic peaks of ice indicated by arrows

Remark: other TR-XRPD experiments confirmed that the endotherm at -37 °C belongs to the metastable eutectic transformation between Form II and ice (data not shown).

III.8 Refractometry measurements

For most of binary mixtures, the refractive index changes linearly over a wide range of concentrations, thus it can be used to measure the solubility of a compound in a given solvent at a given temperature.

In this regard, the solubility curve of DMU in water between -17 °C and 20 °C was determined by refractometry method.

A calibration curve was first plotted by measuring the refractive index of eight solutions of known concentrations of DMU in water (ranging between 50 and 100% wt in water) at room temperature. A linear relationship between the mass percentage of water and the refractive index is shown by constructing the calibration curve (Fig.III.12).

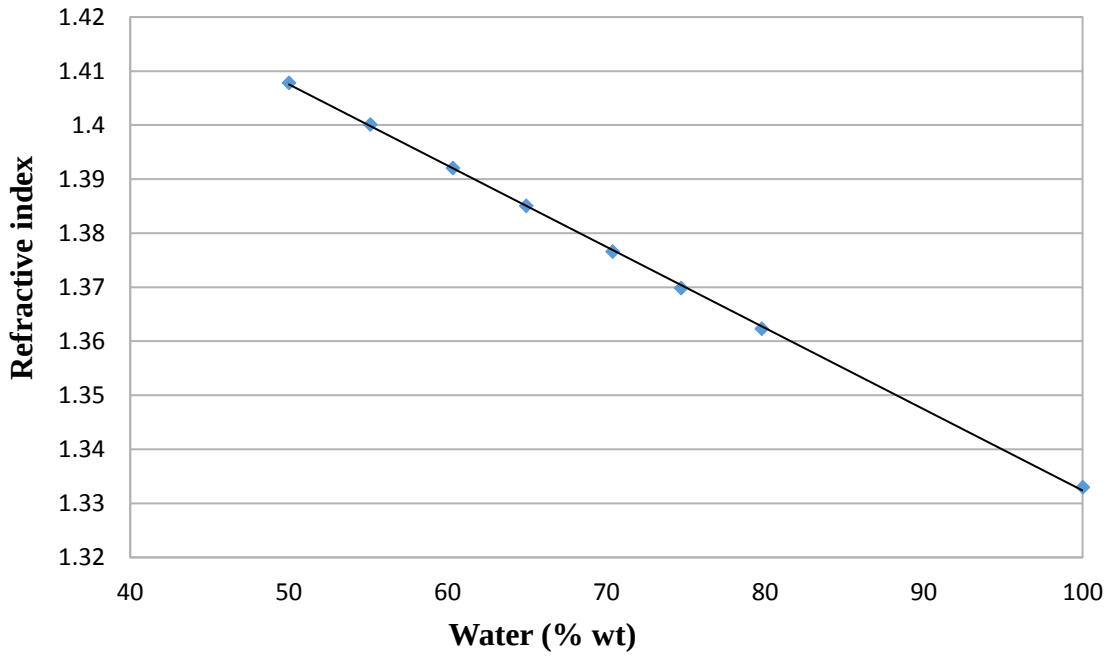

Figure III.12 Calibration curve of the refractive index of different concentrations of DMU-water as function of the mass percentage of water (R^2 =0.999)

Furthermore, a suspension of DMU in water was prepared and stirred for 24 hours at a given temperature ranging between -17 °C and 20 °C. The refractive index of the supernatant solutions at a given temperature was measured by refractometry. Thus, the molar composition was then determined with reference to the calibration curve. The solubility curve was represented by plotting the temperatures as function of the molar percentage of water (Fig.III.13). It is likely to correspond to the metastable eutectic between DMU ssForm II and water. A noticeable sharp decrease of the temperature (from 20 °C down to -17 °C) is observed on a small range of molar percentage of water (from 61% up to 72 %).

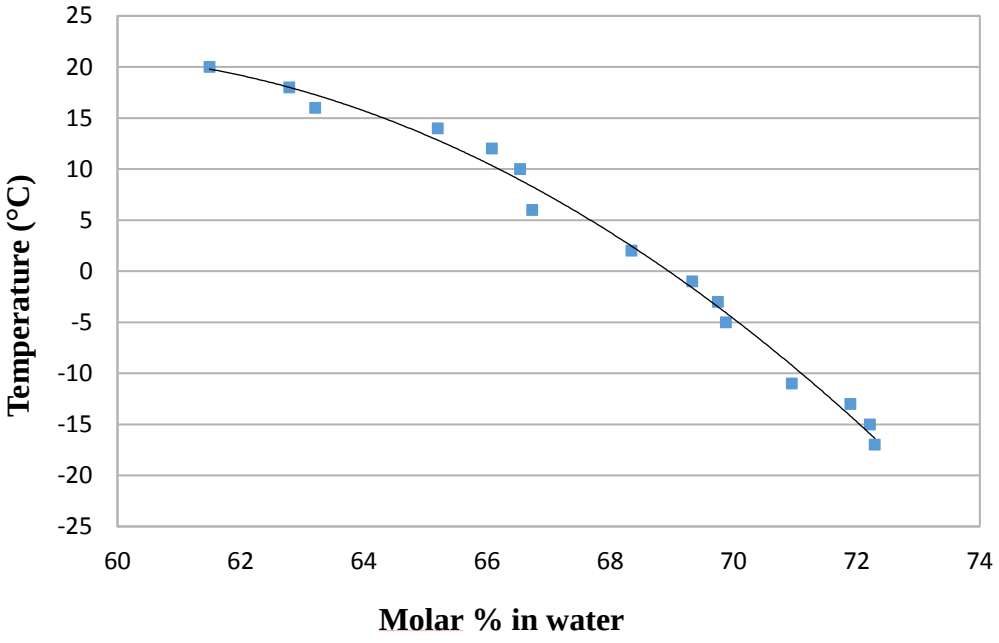

Figure III.13 Solubility curve of DMU in water determined by refractometry method

III.9 Refinement of the metastable eutectic composition of DMU/ water binary system by TR-SHG

Second Harmonic Generation (SHG) is a non-linear optical technique that revealed to be a useful, rapid and sensitive tool for the determination of phase domain boundaries, phase diagram investigations, precise determination of eutectic compositions[(5)], as well as the track of various types of solid-solid transitions [(6,7,8)]. This technique requires at least one non-centrosymmetric phase (see Appendix A.7). Thus, TR-SHG can be used in our case study since DMU (Form II) crystallizes in non-centrosymmetric space group $P2_12_12$.

Different compositions of DMU/water mixtures ranging between 70%, and 80% molar in water were analyzed by TR-SHG. The sample was cooled to -50 °C at a cooling rate of 10 K/min, then kept at -50 °C for two hours and finally it was heated at 1 K/min. TR-SHG measurements were performed every minute during the heating process and the duration of each measurement was 3s. As examples, results obtained for two hypoeutectic compositions (70% and 70.5% molar in water) and one hypereutectic composition (71% molar in water) are reported hereafter.

III.9.1 TR-SHG analysis of the hypoeutectic compositions (70% and 70.5 % molar in water)

The TR-SHG analyses performed on compositions of 70 % and 70.5 % in water show that the signal remains stable between -50 °C and -39 °C. At -38 °C, the signal decreases sharply, which corresponds to the metastable eutectic temperature. Then the signal decreases progressively and totally vanishes at -21 °C for the composition at 70 % molar of water and at -28 °C for the composition at 70.5 % molar of water (Fig.III.14.a.b). These values correspond to the liquidus temperatures. One can notice the sharp decline of the liquidus from -21 °C down to -28 °C on a small range of molar percentage of water (0.5 %). Above the liquidus temperatures, no SHG signal is detected because there is only liquid. In region A, a mixture of ice and DMU Form II crystals exists, in which DMU (Form II) crystals are responsible for the high SHG signal observed. In region B, DMU crystals disappear progressively, therefore the TR-SHG signal decreases. The onset of the metastable eutectic temperature was estimated at -37 °C from DSC result. It is fairly close to the metastable eutectic temperature determined by TR-SHG (-38 °C).

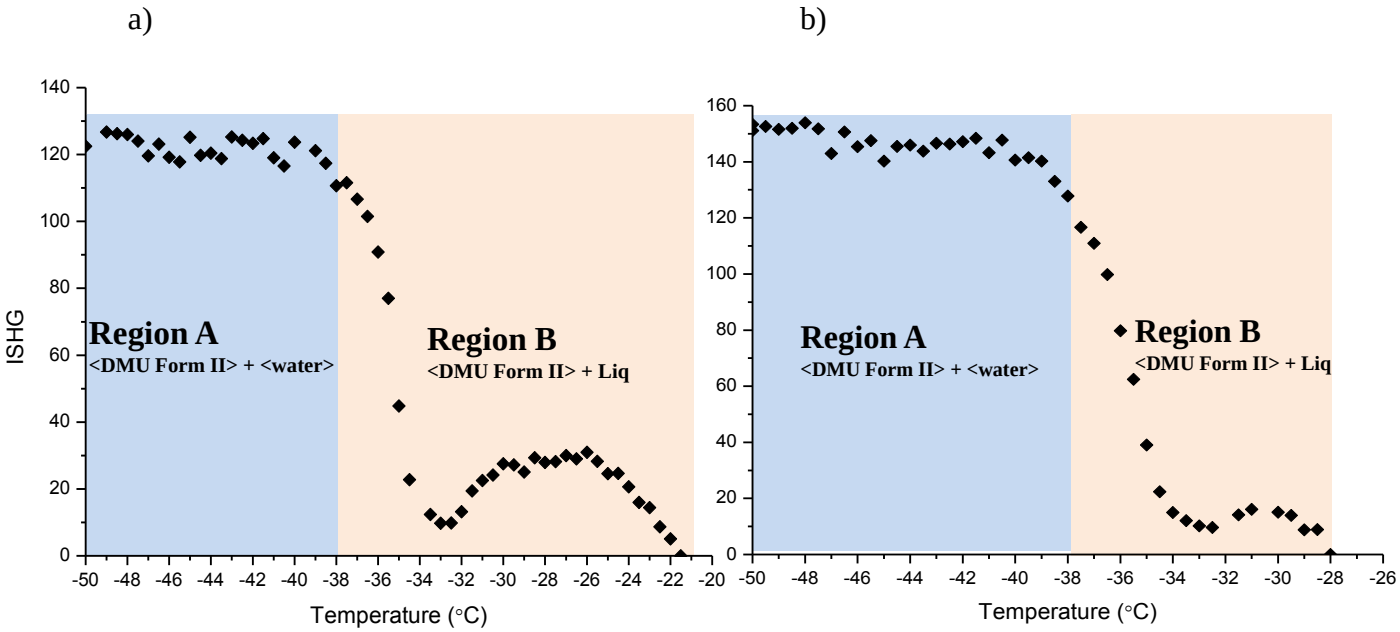

Figure III.14 TR-SHG curves for compositions of a) 70% molar in water and b) 70.5 % molar in water (heating rate : 1 K/min)

III.9.2TR-SHG analysis of the hypereutectic composition (71% molar in water)

The TR-SHG result for the composition of 71 % in water is shown in Figure III.15. A plateau is observed from -50 °C to -39 °C followed by a drastic decrease of the TR-SHG signal at

-38 °C, which corresponds to the metastable eutectic temperature. In region A, a mixture of DMU Form II and ice exists, but only DMU Form II crystals are responsible for the high SHG signal observed. In region B, once all the DMU Form II crystals melt, no TR-SHG signal is produced by an end of fusion. This composition is likely to be very close to that of the eutectic composition.

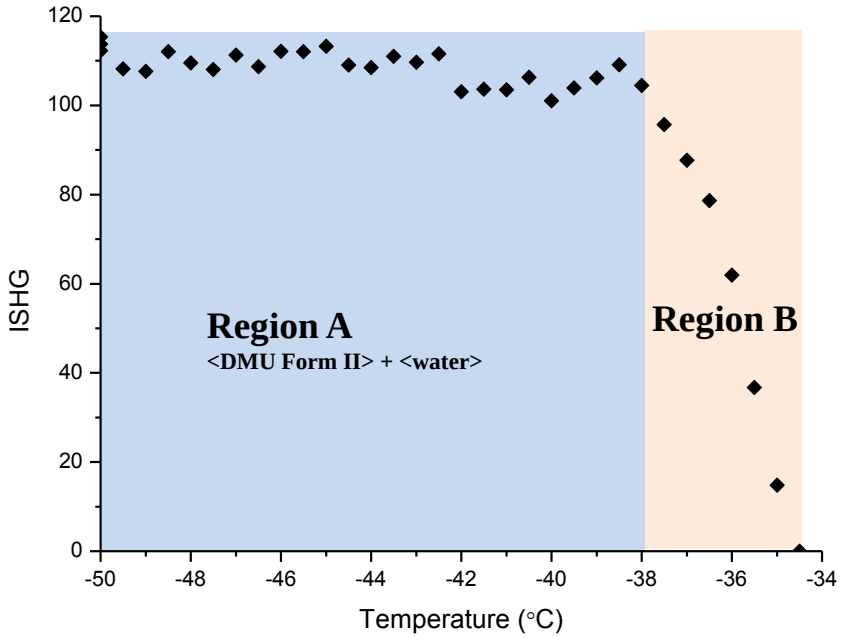

Figure III.15 TR-SHG curves for a composition of 71% molar in water (heating rate : 1 K/min)

In Figures III.14 a-b , the evolution of the TR-SHG signal for the compositions of 70% and 70.5% molar in water shows a progressive decrease (region B) and the metastable eutectic temperature and the liquidus temperature can be determined. It means that these compositions (70% and 70.5%) correspond to metastable hypoeutectic compositions. For the composition of 71% water (Fig.III.15), once the metastable eutectic temperature (- 38 °C) is reached, the TR-SHG signal decreases drastically that no liquidus is observed. It means that this composition (71%) corresponds to a metastable hypereutectic composition. Thus, the metastable eutectic composition is located between the compositions 70.5% and 71% molar in water.

III.10 Construction of the binary phase diagram between DMU and water

Referring to DSC, *in-situ* X-Ray, TR-XRPD, TR-SHG and refractometry analyses, the binary phase diagram between DMU and water is constructed and represented in molar percentage (Fig.III.16).

In the inlet, the two domains of solid solution are exaggerated in water composition for clarity reason. It can be deduced that the system exhibits a metatectic equilibrium with low concentration of water (hundreds of ppm – mass fraction) which decreases the polymorphic transition of DMU from 41 °C to 25 °C.

The presence of a stoichiometric monohydrate at low temperatures is represented, as well as the peritectic invariant at 8 °C above which Form II crystallizes as a solid solution with a minor composition in water.

The stable eutectic composition E was found at 80 % molar in water by extrapolation of the liquidus line of ice.

The eutectic composition E' referring to the metastable equilibrium between the ice and Form II (represented in blue dashed lines) was found between 70.5% and 71 % in molar in water with reference to TR-SHG results.

It should be noted that a metastable equilibrium also exists between ssForm I and the ice with an eutectic invariant below -37 °C but this has never been observed.

The invariants detected by DSC are summarized in Table III.2.

Table III.2 Characteristics of the different invariants observed by DSC

$T_{invariant}$ (°C)	Nature of the invariant	Stability of the equilibrium	the equilibrium
-37	Eutectic	Metastable	<ss II>(<<1%) + <Ice>↔doubly saturated liquid (between 70.5% and 71%)
-20	Eutectic	Stable	<monohydrate> + <water>↔ doubly saturated liquid (≈80%)
8	Peritectic	Stable	<monohydrate>↔<ssII> (<<1%) + doubly saturated liquid(≈65%)
25	Metatectic	Stable	<ssII> (<<1%) + doubly saturated liquid(≈60%)↔<ss I> (<<1%)

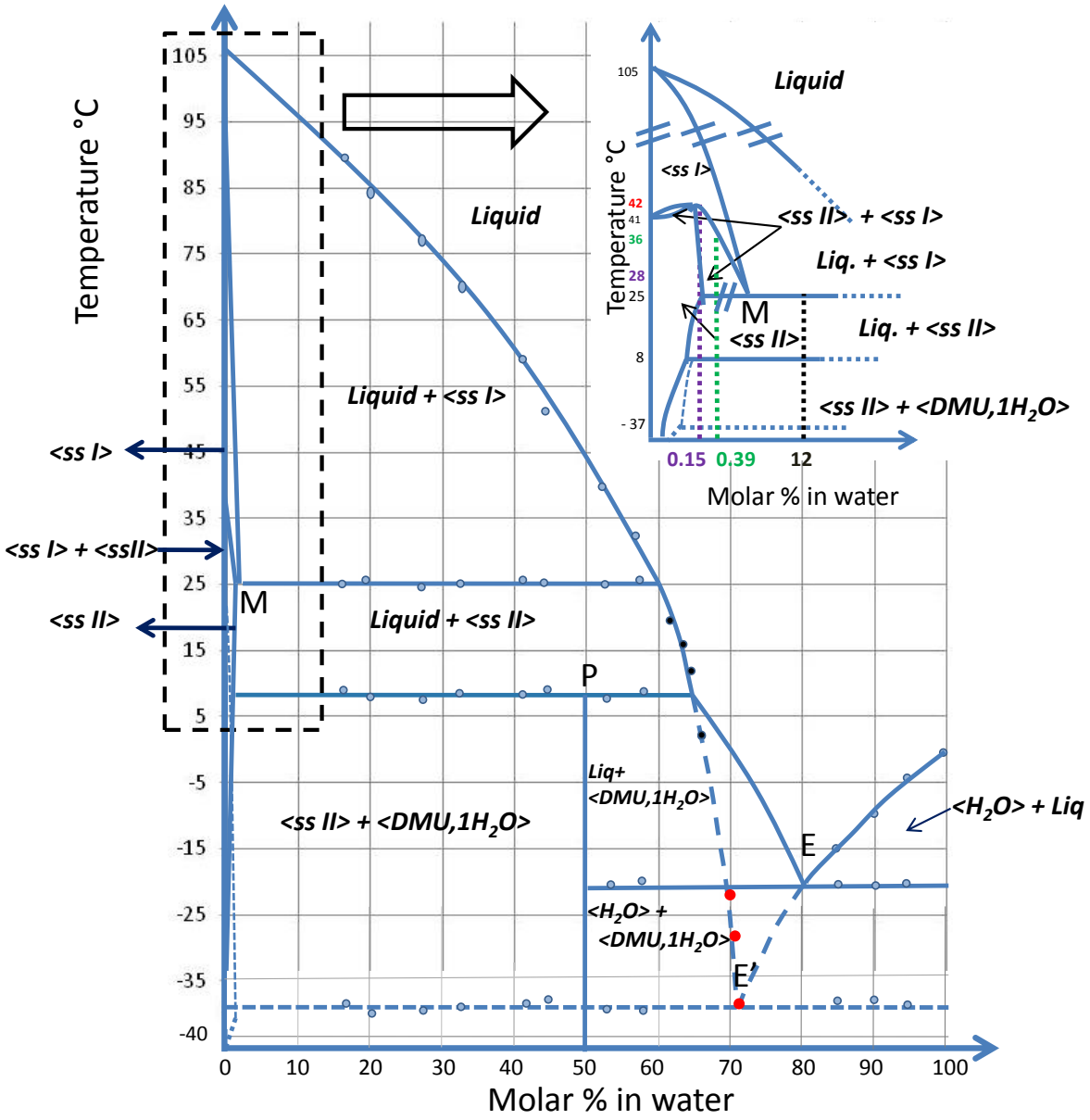

Figure III.16 Schematic binary phase diagram of DMU-water
Blue dots: experimental points obtained by DSC analyses
Black dots: experimental points obtained by refractometry method
Red dots: experimental points obtained by TR-SHG analyses

III.11 Plot of the ideal solubility curves of DMU and water

The ideal depression of the melting point versus the mole fraction is given by the simplified Schroeder Van Laar equation (no correction due to ΔCp and no correction due to pressure).

For the DMU compound: $\Delta H_{F\,DMU} = 12496$ J.mol $^{-1}$. $T_{F\,DMU} = 378.7$ K.

For water compound: $\Delta H_{F\,ice} = 6025.93$ J.mol $^{-1}$. $T_{F\,ice} = 273$ K

Example: For x_{DMU}= 0.8 T_{DMU} = 358.5 K = 85.5 °C.

The calculated values of liquidus temperatures versus mole fraction of water are represented in orange points for DMU ideal solubility curve and in green points for water ideal solubility curve (Fig.III.17).

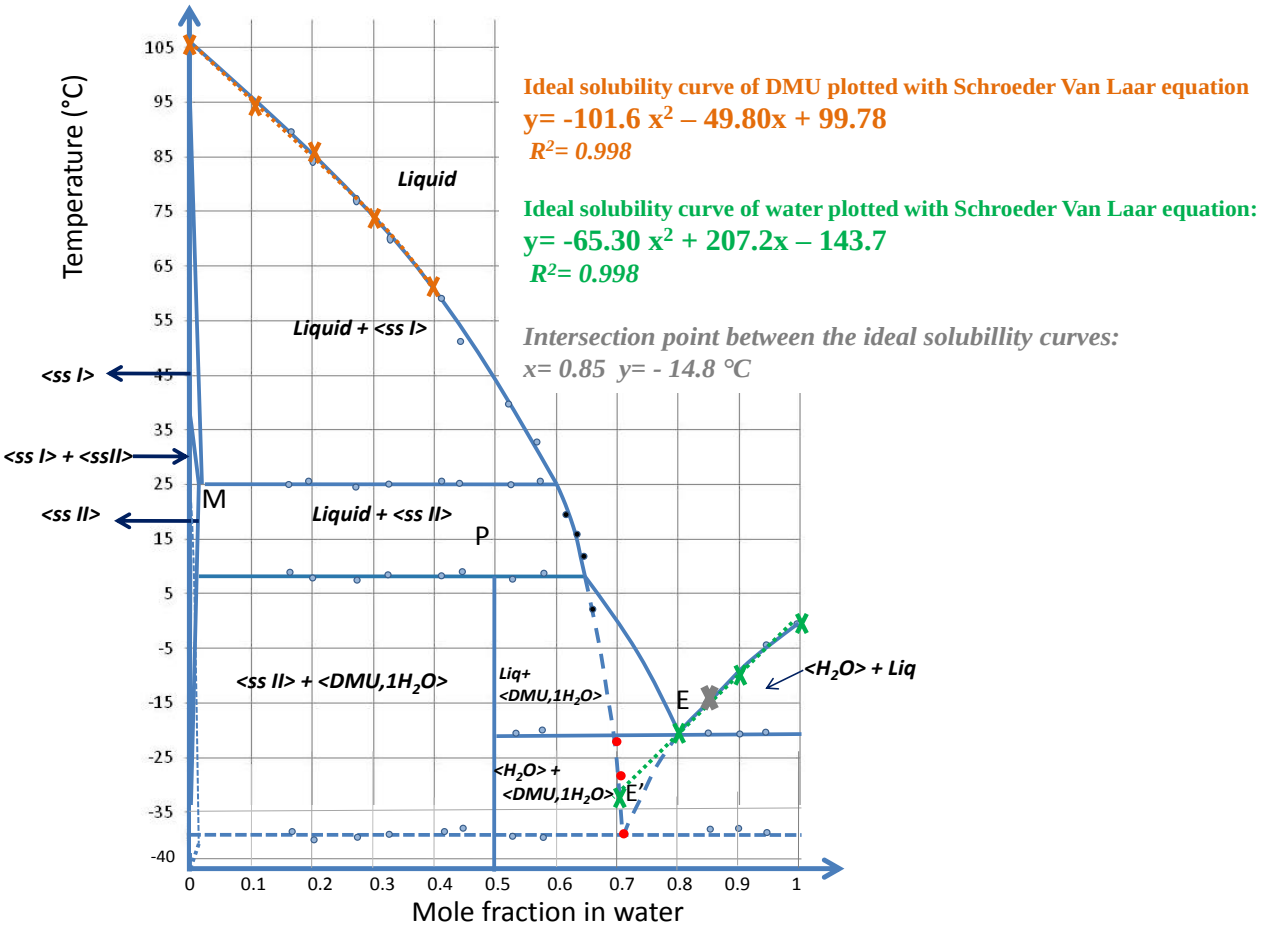

Figure III.17 Illustration of the binary phase diagram DMU-water versus mole fraction in water with the calculated solubility curves of DMU (in orange) and water (in green) given by Schroeder Van Laar equation

The liquidus curve of DMU Form I (supposed pure here) deviates substantially from ideality form above 0.4 mole fraction of water. The ideal liquidus of ice fits reasonably well down to 0.2 mole fraction in DMU (0.8 mole fraction in water).

III.12 Conclusion

The moisture sorption/desorption analyses carried out by DVS revealed a deliquescence behavior of DMU. The strong affinity between DMU and water was suspected in decreasing the solid-solid transition from Form I to Form II. The construction of the whole binary phase diagram between DMU and water was achieved by combining TR-XRPD (*ex-situ* and *in-situ*) and DSC, refractometry and TR-SHG results. It confirms the correlation of the analyses showing that water at low concentration levels (hundreds of ppm level) decreases the polymorphic transition temperature of DMU from 41 °C to 25 °C through a metatectic equilibrium [(9)].

An X-ray analysis in transmission will be useful to determine the crystal structure of the monohydrate. On-going analyses will be performed by SHG to find out if the monohydrate crystallizes in a non-centrosymmetric space group (or centrosymmetric space group) and to determine the precise stable eutectic composition.

Finally, the findings in this study indicate that DMU Form I doesn't exist as pure form but as a solid solution with water (ssI). This indication raises an open question of the possible role of water in the mechanism of the inhibition of the transition of γ of PZA.

REFERENCES

1.C. Näther, C. Döring, I. Jess, P. G. Jones and C. Taouss (2013), Thermodynamic and structural relationships between the two polymorphs of 1,3-dimethylurea, ActaCryst., 69, 70-76.

2.A.Clow (1940) , Deliquescence in Urea and Methyl-ureas,Nature, 146, 26-26.

3.L. Misane, S. El Allali, M. Kaddami, A. Zrineh, R. Tenu, J. Berthet, J.J. Counioux (2000), Etude du système quasi ternaire H_2O–NH_4NO_3–$Mg(NO_3)_2{\cdot}6H_2O$: isotherme 60°C, coupe quasi binaire NH_4NO_3–$Mg(NO_3)_2{\cdot}6H_2O$ et diagramme polythermique, ThermochimicaActa., 354, 135-144.

4.Applicant: University of Rouen. G. Coquerel, M. Sanselme, A. Lafontaine, Method and measuring scattering of X-rays, its applications and implementation device. 2012, patent WO2012/136921A1

5. L.N Yuan, S. Clevers, N.Couvrat, V.Dupray, G.Coquerel Proceeding BIWIC 2015: 22nd International Workshop on Industrial Crystallization 09/2015

6. S. Clevers, C.Rougeot, F.Simon,M. Sanselme, V.Dupray, G. Coquerel, G. (2014). Detection of order–disorder transition in organic solids by using temperature resolved second harmonic generation (TR-SHG). *Journal of Molecular Structure*, *1078*, 61-67.

7. F.Simon,S.Clevers, V. Dupray, G.Coquerel, G. (2015). Relevance of the Second Harmonic Generation to Characterize Crystalline Samples. *Chemical Engineering & Technology*.

8. S. Clevers, F.Simon, V.Dupray, G. Coquerel: Temperature resolved second harmonic generation to probe the structural purity of m-hydroxybenzoic acid. J. Therm. Anal. Calorim.,112 (2013) 271-277.

9. G.Baaklini, M. Schindler, N.Couvrat, M. Sanselme, Y. Cartigny, G.Coquerel. Proceeding BIWIC 2015 : 22nd International Workshop on Industrial Crystallization 09/2015

Chapter IV

N-methylurea

IV.1 Introduction

N-methylurea (hereafter NMU) with the molecular structure shown in Figure IV.1 is a hygroscopic non-linear optical material [(1)]. Few bibliographical reviews are given by literature on NMU. In fact, the only known crystal structure of NMU is a stable form that was first proposed in 1933[(2)], the definitive structure was solved in 1976 by Huiszoon and Tiemessen[(3)]. NMU crystallizes in the orthorhombic system with the chiral space group $P2_12_12_1$ (CSD refcode: MEUREA).

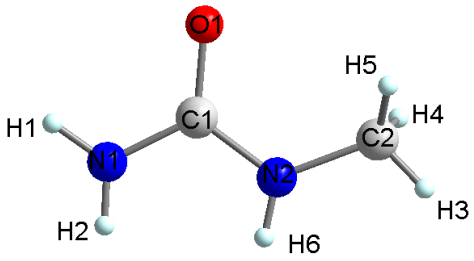

T_F^I= 98 °C

ΔH_F^I = 188.5 J/g

Figure IV.1 Molecular structure of NMU with labelled atoms

In Chapter II, urea derivatives were tested for their ability to block γ form of Pyrazinamide. As part of the same project, we decided to investigate polymorphs of NMU that displayed new features by X-ray analysis upon Spray Drying.

IV.2 Behavior of NMU in Spray Drying with water

Feed solutions were prepared by dissolving 1g of NMU in 40 mL of water. Spray Drying experiments were carried out with a feed flow rate at 4 mL/min, an atomizing airflow rate at 473 L/h, aspiration at 35 m^3/h, inlet temperatures fixed at 100 °C and 120 °C; the outlet temperatures recorded were 41 °C and 58 °C respectively. The open mode was selected for these aqueous solutions. The hygroscopic character of NMU gave rise to sticky particles crystallizing on the walls of the cyclone. Thus the yield was poor (less than 5%). X-ray analyses performed on spray-dried NMU are illustrated in Figure IV.2. In addition to the characteristic peaks of the stable form, Figure IV.2 reveals new peaks at 2θ= 13.2° , 15.2° and 26.5° (marked with arrows) corresponding to a new phase in the samples obtained by Spray Drying NMU in water with T_{in} set at 100 °C and 120 °C.

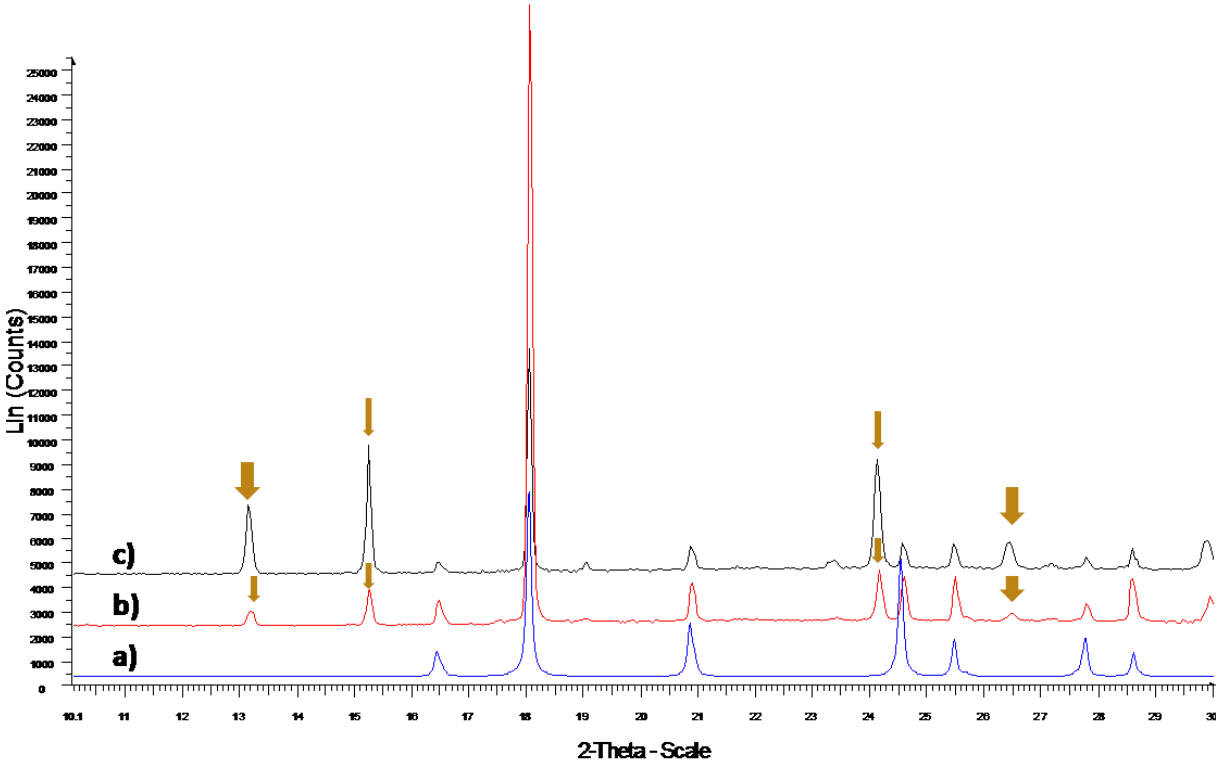

Figure IV.2. Superimposition of a) calculated XRPD patterns of NMU (CSD ref code: MEUREA) and experimental XRPD patterns of spray drying NMU with water b) T_{in} = 100 °C c) T_{in}= 120 °C with arrows referring to a new phase.

IV.3 Behavior of NMU in Spray Drying with alcoholic solvents

Due to the hygroscopicity of NMU, it was dried prior use in a desiccator over P_2O_5 atmosphere. The alcoholic solvents were dried as well by using zeolithes as molecular sieves. Spray Drying experiments were carried out by dissolving 1g of NMU in 40 mL of one of the following alcohols: methanol (boiling point (bp) = 65 °C), isopropanol (bp = 82.5 °C) and ethanol (bp = 79 °C), isopropylalcohol (82.6 °C), n-propyl alcohol (bp = 97 °C) and n-butanol (bp = 117.4 °C). The relatively high solubility of NMU in alcoholic solvents was the main reason for selecting these solvents. The solubility of NMU in each solvent was determined by gravimetric method at 20 °C. It was found at 47% in methanol, 38% in ethanol, 19% in both isopropyl and in n-propyl alcohols and 14% in n-butanol.

IV.3.1 Behavior of NMU in Spray Drying with alcoholic solvents at T_{in} 80 °C

It was possible to perform Spray Drying with an inlet temperature lower than the boiling points of the listed alcohols since they exhibit a high vapour pressure. Thus, for this series of experiments, the drying temperature was set at 80 °C, the outlet temperature was recorded at

50 °C and the close mode was selected since the feeds contain organic solvents, the feed flow rate was fixed at 4 mL/min, the atomizing air flow rate at 473 L/h and the aspiration at 35 m^3/h.The powder was easily collected compared to the previous experiments carried out with water. The yield was estimated to be 40%.

Figure IV.3 shows the X-ray powder diffraction patterns of spray-dried samples compared with the calculated pattern of the stable form.

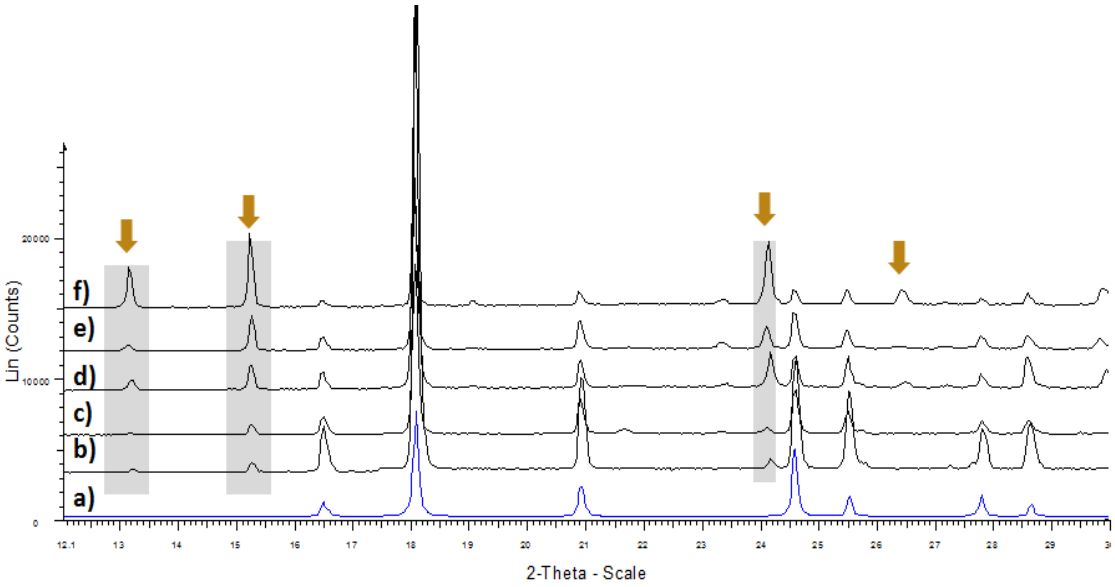

Figure IV.3 Superimposition of the a)calculated XRPD patterns of NMU and XRPD patterns of spray drying NMU with T_{in} = 80 °C with b) methanol c) ethanol d) n-propanol e) Isopropylalcohol f) n-butanol with arrows referring to a new phase

The essays realized by Spray Drying NMU with different alcoholic solvents with an inlet temperature fixed at 80 °C, also reveal a mixture of two phases by X-ray analysis: stable form and new phase: new peaks indicated by arrows and highlighted in grey at 2θ = 13.2°, 15.2° and 26.5°. These new peaks correspond to the same ones detected by X-Ray analyses after Spray Drying NMU in water (Fig.IV.2).

It remains important to optimize the parameters of Spray Drying in order to get this phase structurally pure. The inlet temperature has been modified for this purpose.

IV.3.2 Effect of the inlet temperature

The same protocol was repeated for the feedstock preparation. In this series of experiments, the inlet temperature was increased from 80 °C to 120 °C. The oulet temperature recorded was 70 °C.

What it is noticeable in the XRPD patterns shown in Figure IV.4, is that the new phase that was observed with the series of experiments carried out at 80 °C, disappeared by raising the

inlet temperature to 120 °C. Only peaks of the stable form are present in all the essays with different solvent. Right after this observation, two hypotheses were elaborated: the first hypothesis states that the new phase has a monotropic relationship with the stable form. In this case, the increase of the inlet temperature results in an increase of the outlet temperature from 50 °C to 70 °C which is considered as a kinetic factor for favouring the transition of the new metastable phase to the stable phase. The second hypothesis states that there is an enantiotropic relationship between the two forms and the solid-solid transition temperature is located at circa 70 °C.

Thus, to prove these hypotheses, it will be definitely important to find another way of crystallization that leads to the structurally pure metastable form.

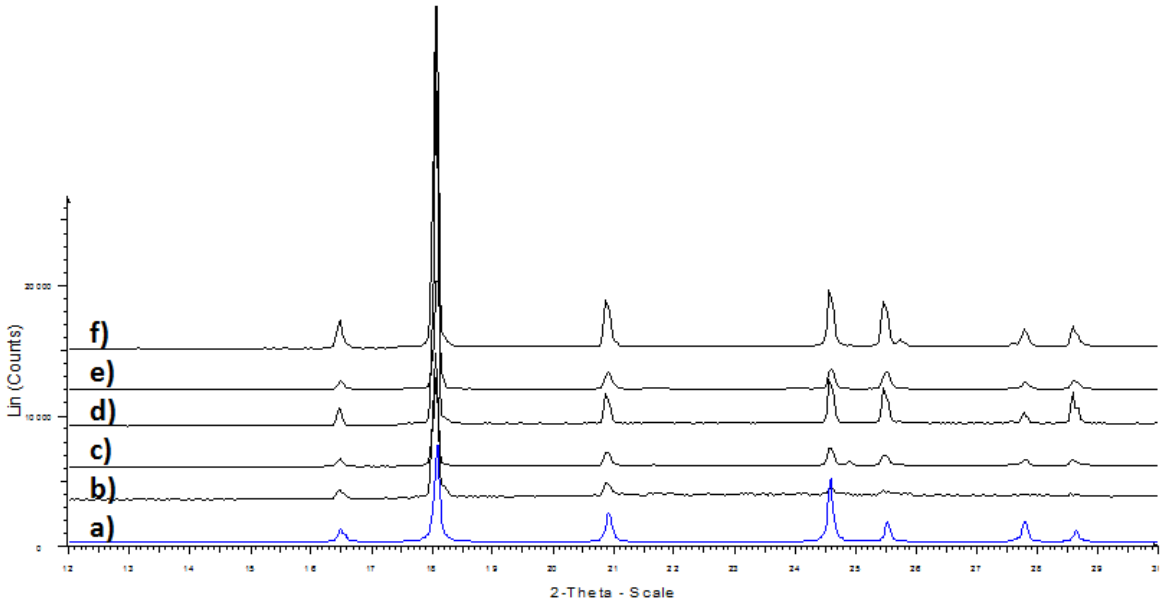

Figure IV.4 Superimposition of a) the calculated pattern of the stable form of NMU and the experimental XRPD patterns of spray-dried NMU obtained at T_{in}=120 °C with b) methanol c) ethanol d) n-propanol e) Isopropylalcohol f) n-butanol

IV.4 High Energy Milling of NMU

1g of the commercial NMU was ground in a jar with milling balls during 12 hours. Figure IV.5 illustrates the XRPD patterns on ground NMU. X-ray analyses show that the phases were intact after LAG and neat HEM.

Only characteristics peaks of the stable form are present after neat HEM and LAG processes of NMU. The peaks are broad after grinding probably because of the reduction of particle size and the drop of long range order (decrease of the crystallinity).

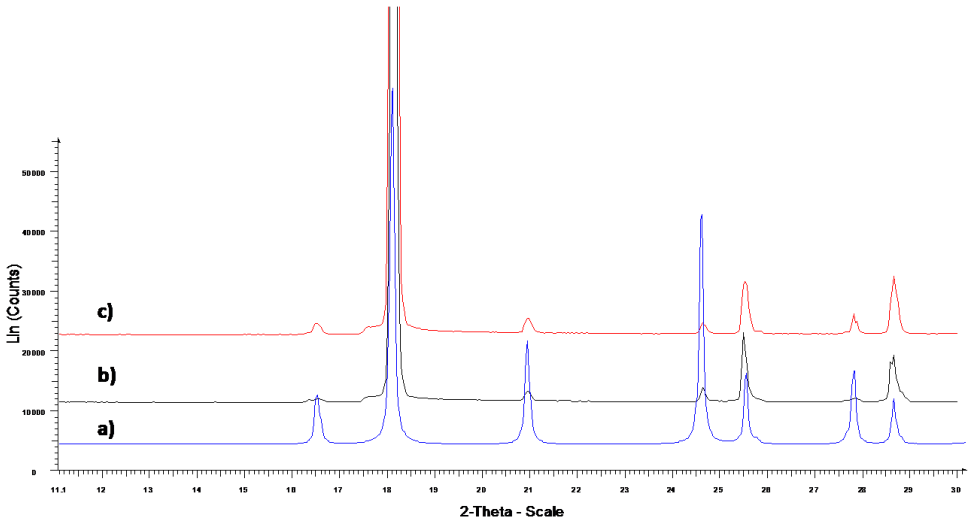

FigureIV.5 Superimposition of a) the calculated pattern of the stable form of NMU and XRPD patterns of NMU obtained after b) neat HEM c) LAG

IV.5 Melt-crystallization of NMU

Melt crystallization experiments were conducted in capillaries: commercial NMU was introduced in 0.5 mm diameter glass capillary tubes and heated up to fusion, then directly quenched at a predetermined temperature using a cryostat fed with liquid nitrogen (Oxford Cryosystems). X-ray diffraction measurements in transmission geometry (Inel CPS 120 diffractometer) were then performed on the quenched samples at different temperatures (Fig. IV.6). The comparison between the XRPD patterns of NMU obtained after melt quenching and the stable form reveals the crystallization of new forms at different temperatures.

The same polymorphic form is observed at -53 °C and 21 °C. In fact, the peak position shift observed between both diffractograms is definitely due to lattice expansion / contraction between the two temperatures. The XRPD pattern of this form exhibits new characteristic peaks different from the stable form. Hence, it will be assigned to as Form II whereas the stable form will be assigned to as Form I.

Starting from Form II, the diffractogram recorded at -173 °C also reveals new characteristic peaks different from Form II and Form I. Hence, this new phase will be assigned to as Form III.

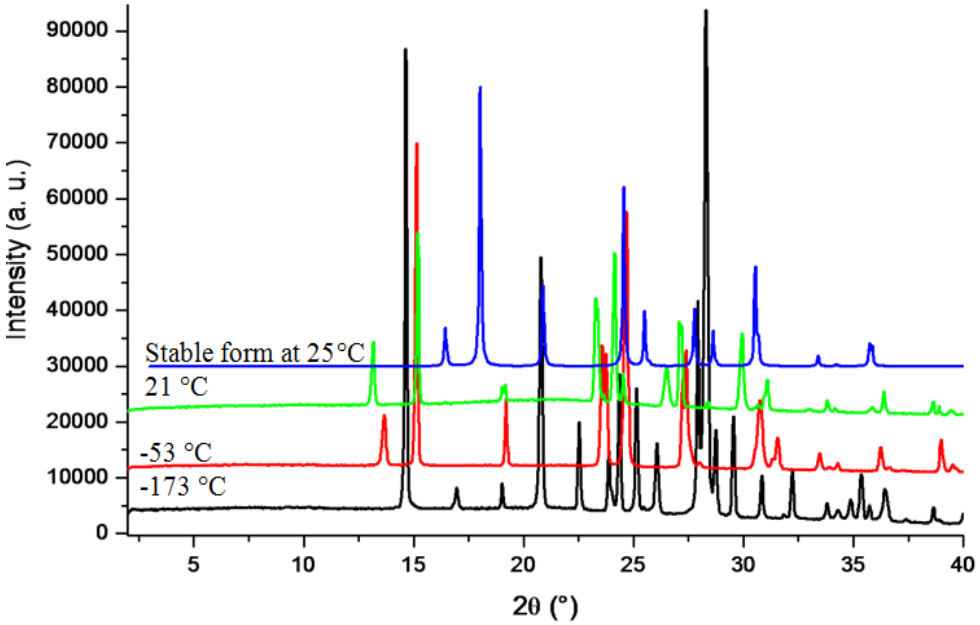

Figure IV.6 XRPD patterns of NMU stable form at 25 °C (blue) and after melt-quenching at different temperatures (red: -53 °C, black: -173 °C) and after heating the quench from -173 °C to 21°C (green)

2θ positions of characteristic reflections of Forms I, II and III are summarized in Table IV.1

Table IV.1 Characteristic peaks of Form I, II and III

Form I (25 °C) **2θ (°)**	**Form II (-50 °C)** **2θ (°)**	**Form III (-173 °C)** **2θ (°)**
16.6	**13.7**	**14.6**
18.1	**15.1**	**16.9**
20.8	**23.6**	**20.8**
24.5	**24.7**	**22.5**
25.5	**27.4**	**25.1**
27.8	**30.4**	**28.3**

IV.5.1 TR-X-ray analyses on NMU forms

TR-X-Ray analyses were performed between -163 °C and -113 °C with a heating rate of 1 K/min (Fig.IV.7). Each analysis lasts for 30 minutes at a defined temperature. Form III is obtained from melt crystallization at -163 °C.

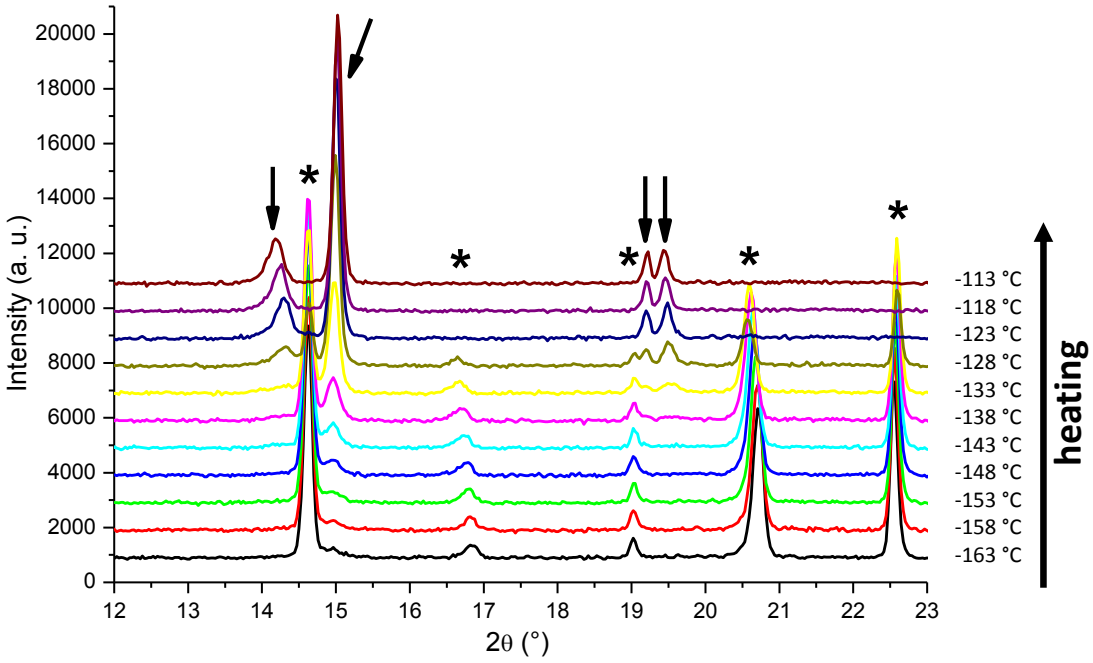

Figure IV.7 TR- X-ray diffraction patterns obtained upon heating Form III, represented in the [12°-23°] 2θ range. Characteristic peaks of Form II are marked with arrows while those of Form III are pointed with an "*".

Upon heating from -163 °C, the first characteristic peak of Form II (at 2θ = 15.1°) is detected between -143 °C and -138 °C. Peaks at 20.8° and 22.5° in 2θ referring to Form III decrease in intensity upon heating from -163 °C till -128 °C. These peaks completely disappear at -123 °C where the transition seems to be completed. At this temperature, characteristic peaks of Form II are only detected.

The transition between Form II and Form III was found to be reversible upon heating and cooling (data not shown upon cooling).

IV.5.2 Stability relationship between the three forms of NMU.

TR-X-Ray results were completed by thermal analysis with the support of a power-compensated DSC. Thus, the stability behavior and the thermodynamic relationships between forms I, II and III were investigated.

The melt quenching process was reproduced inside the crucible as following: starting from the commercial batch Form I, the sample was heated till melting at 5 K/min. The liquid melt was then rapidly cooled down till -150 °C with a cooling rate of 20 K/min (Fig.IV.8.a). The sample was heated again at 5 K/min up to 110 °C (Fig.IV.8.b).

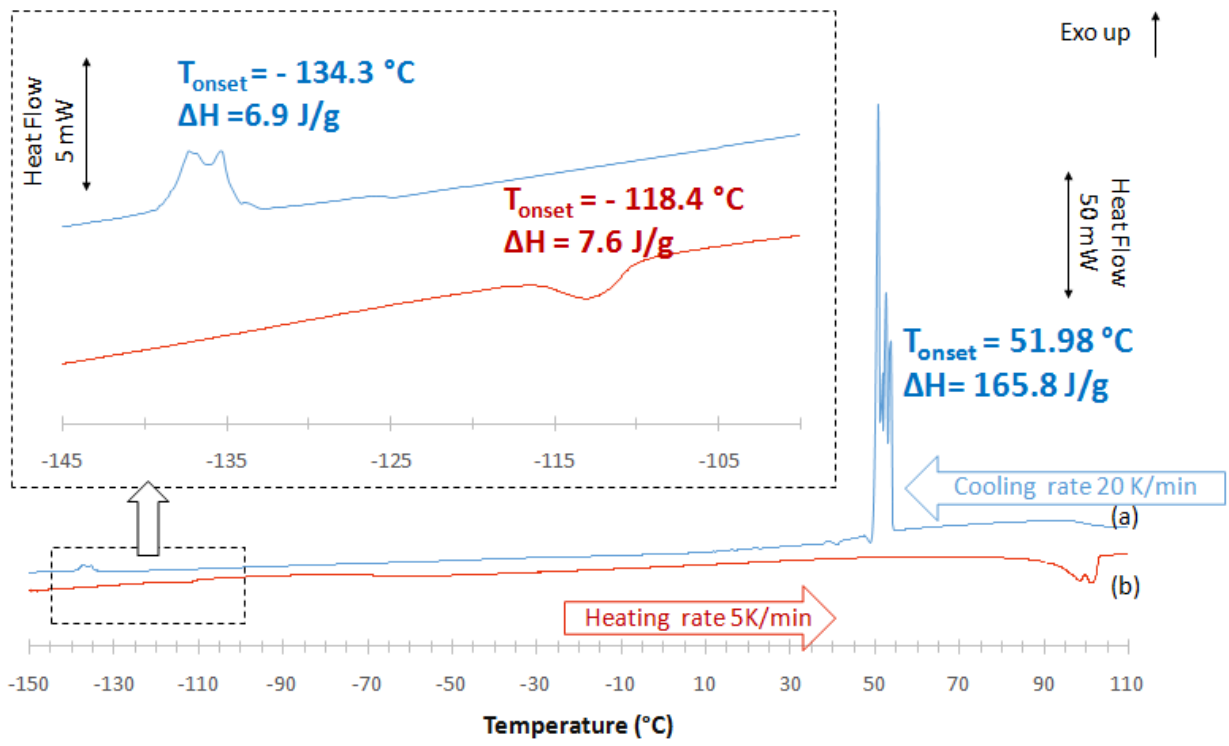

Figure IV.8 DSC curves of NMU upon a) cooling from the melt (cooling rate: 20 K/min) followed by b) heating up to the melt (heating rate: 5 K/min)

Different thermal events are detected by DSC analysis upon cooling from the melt and the second heating that starts at -150 °C.

The following observations can be noted:

Upon cooling, Form II is generated on solidification of the melt. This crystallization is illustrated by a sharp exothermic peak with an onset at circa 51 °C. Three additional exothermic peaks are observed just after this recrystallization. These events are likely to be the successive solidifications of scattered drops of the melt inside the crucible. Upon further cooling, another exothermic peak with an onset at circa -134 °C is detected. This peak would correspond to the reversible solid-solid transition Form II → Form III with hysteresis (Fig.IV.8.a).

Upon heating, an endothermic peak with an onset at -118 °C corresponding to solid-solid transition Form III → Form II is detected. It can be inferred from the hysteresis phenomenon and the detection of a (weak) enthalpy that this transition is of a first order. The mechanism of conversion from Form II to Form III should then proceed through a nucleation and growth.

Upon further heating, two endothermic peaks close to each other are observed. The first endothermic peak at circa 95.2 °C (ΔH_F^{II} = 166.6 J/g) is assigned to the fusion of Form II (see appendix C), whereas the second endothermic peak at 98 °C (ΔH_F^{I} = 188.5 J/g) is assigned to the fusion of Form I (Fig.IV.8.b). This strongly indicates that Form II has a

monotropic character because Form I has an enthalpy of fusion and temperature of fusion higher than that of Form II (this is in agreement with Burger and Ramberger rules [I.10]. Besides, an X-ray follow-up of Form II revealed a spontaneous return of Form II to Form I within few days of storage at room temperature.

A rough approximation of the enthalpy of fusion of Form III can be calculated as following:

$\Delta H_F^{III} = \Delta H_F^{II} + \Delta H_t^{III \rightarrow II}$

$= 166.6 + 7.6$

$= 174.2$ J/g

The comparison between the enthalpies of fusion of the three forms shows that

$\Delta H_F^{I} > \Delta H_F^{III} > \Delta H_F^{II}$.

All investigations presented above prove that Form I is the thermodynamically stable form whatever the temperature. Form II and III are monotropically related to Form I. A reversible solid-solid transition between Form II and III was found at -118 °C by using DSC. The discrepancy between the transition temperature found by DSC and TR- X Ray diffraction can be due to the weak thermal conductivity of the capillary in the latter measurements.

IV.5.3 Description of the crystal structures

In this section, we present a brief description of the molecular structures and packing features of the three polymorphs of NMU.

The lattice parameters of Form II and III were determined from a Rietveld fit of the experimental X-ray powder diffraction patterns shown in Figure IV.9 for Form II at -50 °C and in Figure IV.10 for Form III at -173 °C.

Rietvield refinement led to acceptable R_{wp} values of 7.3 % and 10.6 % for Form II and III respectively and R_p values of 5.2 % and 7.6 % for Form II and III respectively.

The atomic coordinates of Form I, II and III are reported in the appendix D.

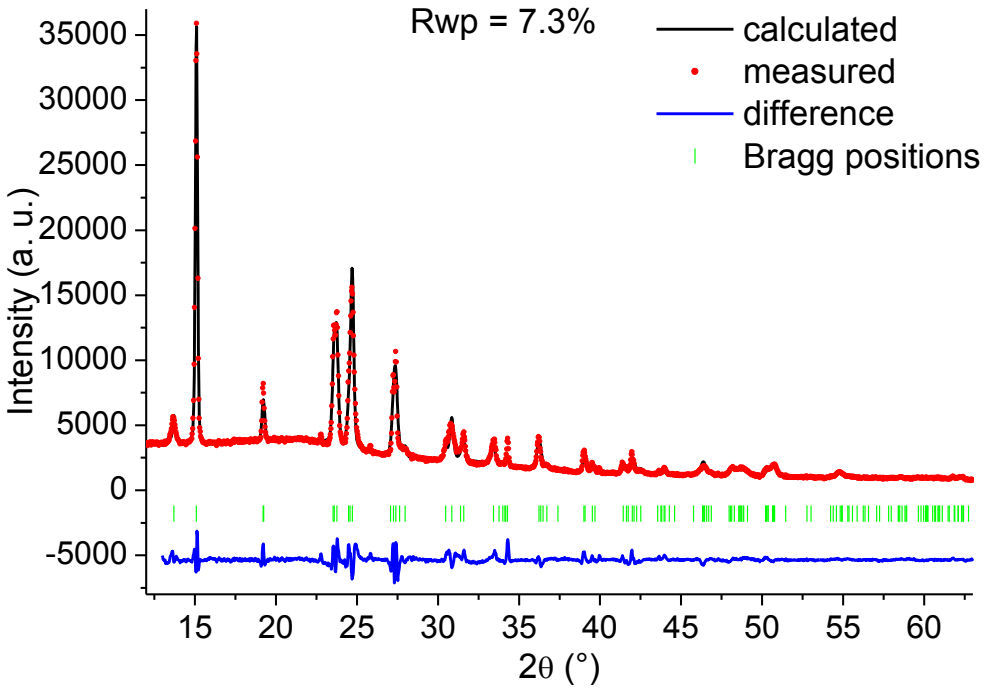

Figure IV.9 Experimental (red) and calculated (black) XRPD patterns for the structure of Form II at -50 °C. Systematic existences calculated from the monoclinic unit cell (green ticks), and difference between calculated and experimental XRPD patterns (blue).

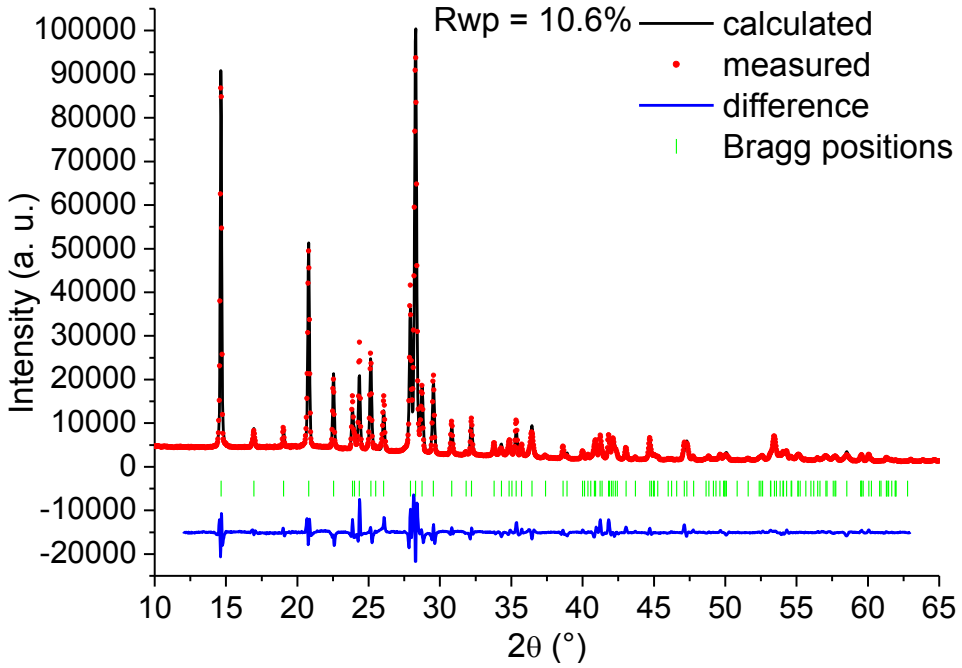

Figure IV.10 Experimental (red) and calculated (black) XRPD patterns for the structure of Form III at -173 °C. Systematic existences calculated from the monoclinic unit cell (green ticks), and difference between calculated and experimental XRPD patterns (blue).

The crystal data of Form I, II and III are summarized in Table IV.2.

Table IV.2 Crystal data for Forms I II and III.

Form	(I) at 25 °C	(II) at - 50 °C	(III) at -173 °C
Crystal system, space group	Orthorhombic $P2_12_12_1$	Monoclinic $P2_1/c$	Monoclinic $P2_1/c$
a (Å)	8.4767 (6)	4.6147 (6)	4.6604 (3)
b (Å)	6.9809 (5)	6.5781 (12)	7.4079 (7)
c (Å)	6.9227 (6)	12.9004 (16)	10.4566 (6)
β (°)	90	90.418 (5)	92.007 (4)
Z	4	4	4
Density (g/cm^3)	1.201 (1)	1.256 (1)	1.364 (1)
Volume ($Å^3$)	410 (1)	392 (1)	361 (1)

The packing of the three forms displayed a common feature based on the establishment of "V-shaped" (bifurcated) intermolecular hydrogen bonds (Table IV.3) that gives rise to molecular chains (Fig.IV.11), in the three structures they are spreading along *a* axis.

Table IV.3 Hydrogen bond distances of Forms I, II and III

Form	I d (Å)	II d (Å)	III d (Å)	
$O_1 \ldots H_1 - N_1$	2.08	2.075	2.259	Between molecular chains
$O_1 \ldots H_2 - N_1$	2.22	2.173	2.165	Establishment of 'V-shaped' intermolecular hydrogen bonds
$O_1 \ldots H_6 - N_2$	2.16	2.186	2.115	

As shown in Figure IV.11.a, the molecules within the chains of Form I present different orientations, the methyl moieties are on both sides of the central axis of the molecular chain. Furthermore, the chains have a ziz-zag shape in form I while they are fairly flat in forms II and III (Fig.IV.11.b-c).

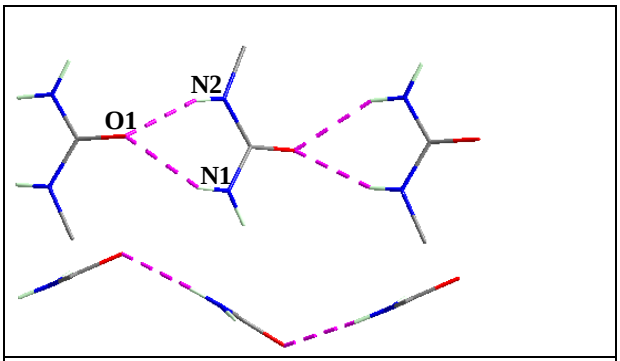

a) top and side view of molecular chains in Form I

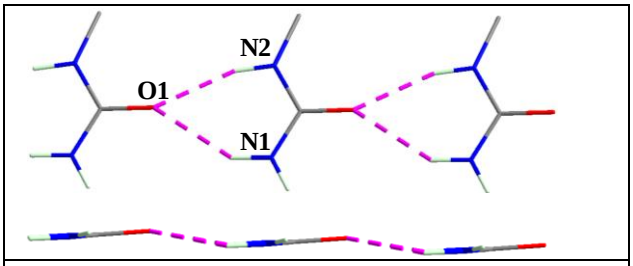

b) top and side view of molecular chains in Form II

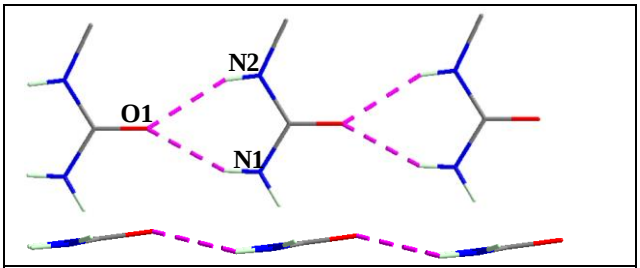

c) top and side view of molecular chains in Form III

Figure IV.11 Molecular chains built from hydrogen bonds (dashed pink lines) established between consecutive molecules along *a* axis in a) Form I b) Form II c) Form III

These chains are connected through another type of hydrogen bonds (Table IV.3). These lead to the final arrangement in a three dimensional network for Form I (Fig.IV.12) and in layers for the Forms II (Figures IV.13-14-15) and III (Figures IV.16-17-18). In the case of Form II and Form III, the differences are quite small. They are due to a slight shift between the packing of the layers, while the differences between Form I and the two others forms are obvious: the different orientation of the methyl moieties along the molecular chains, and the three dimensional framework that arises from this alternating orientation.

The molecular chains of Form I are depicted in different colors, the hydrogen bonds (dashed blue line) are connecting these molecular chains and give rise to a three dimensional network (Fig.IV.12.a).

The availability of hydrogen bonds involved in the connection of the molecular chains in Form I is increased due to the different orientation of the methyl moiety and the "brick-wall packing" of NMU along the axis of the molecular chains. Therefore, the density and the orientation of the hydrogen bonds network give rise to a three dimensional packing (Fig.IV.12.b).

a) ***b)***

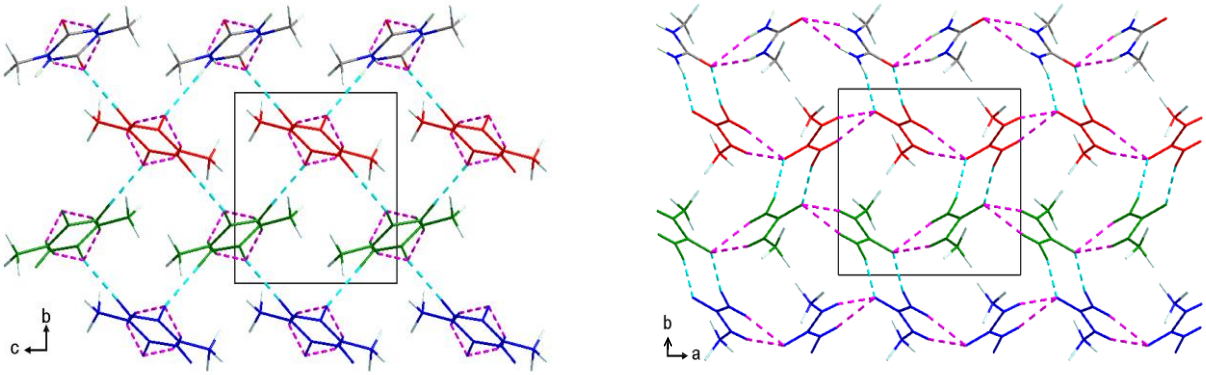

Figure IV.12 Molecular chains of Form I along a) *a* axis and b) *c* axis

The molecular chains in Form II are connected along *b* through a third type of hydrogen bonds (dashed blue lines). The molecular chains are oriented in an anti-parallel way and generate layers in *ab* (Fig.IV.13).

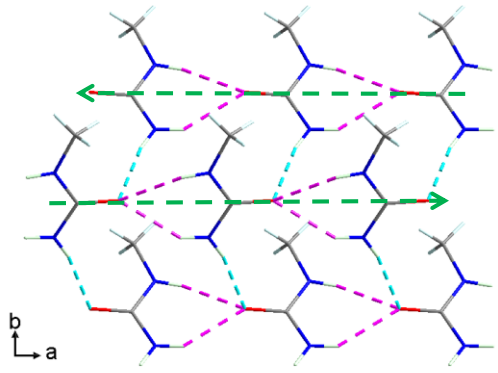

Figure IV.13 Molecular chains of Form II along *c* axis

The representation of Form II along *a* axis shows that the adjacent layers are stacked along *c* and that the methyl moieties are face to face from adjacent layers. (Fig.IV.14)

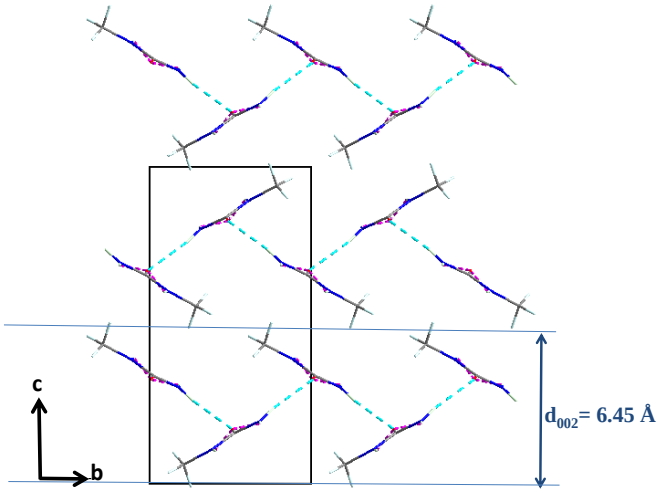

Figure IV.14 Form II along *a* axis showing methyl moieties face to face from adjacent layers.

Besides, the shift is not present between consecutive layers in Form II (Fig.IV.15 a-b).

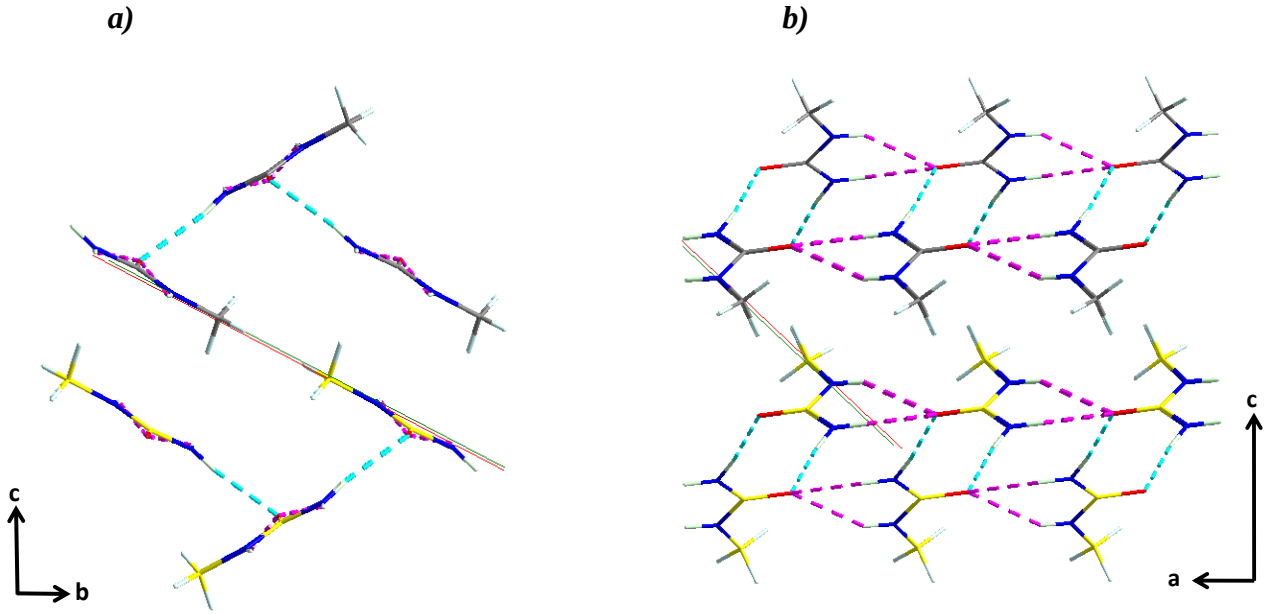

Figure IV.15 Form II along a) *a* axis and b) *b* axis
Carbon atoms colored in yellow correspond to the lower layer
The red segments show the alignment of methyl groups

The molecular chains in Form III are also connected along *b* through a third type of hydrogen bonds (dashed blue lines). The molecular chains are oriented in an anti-parallel way and generate layers in *ab* as in Form II (Fig.IV.16).

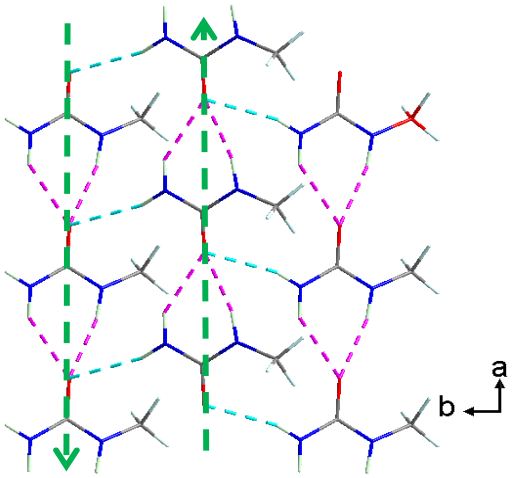

Figure IV.16 Molecular chains of Form III along *c* axis

The representation of Form III along *a* axis shows that the adjacent layers are stacked along *c* and that the methyl moieties are face to face from adjacent layers as in Form II. (Fig.IV.17)

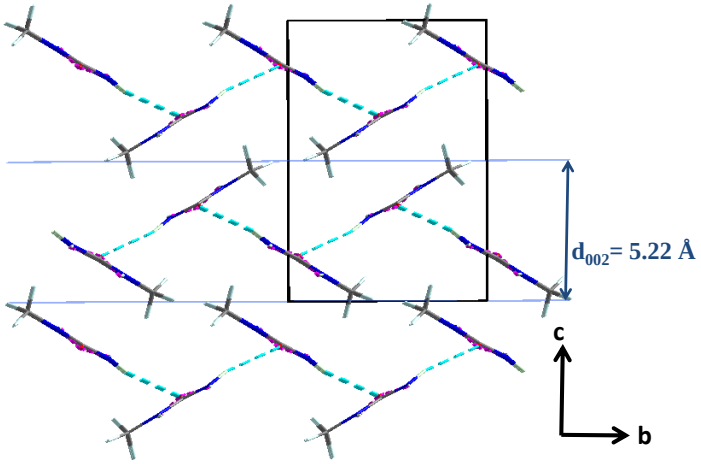

Figure IV.17 Form III along *a* axis

Hence, it can be noticed that the consecutive layers in Form III are shifted, so that the steric hindrance generated by the methyl moieties is limited (Fig.IV.18 a-b).

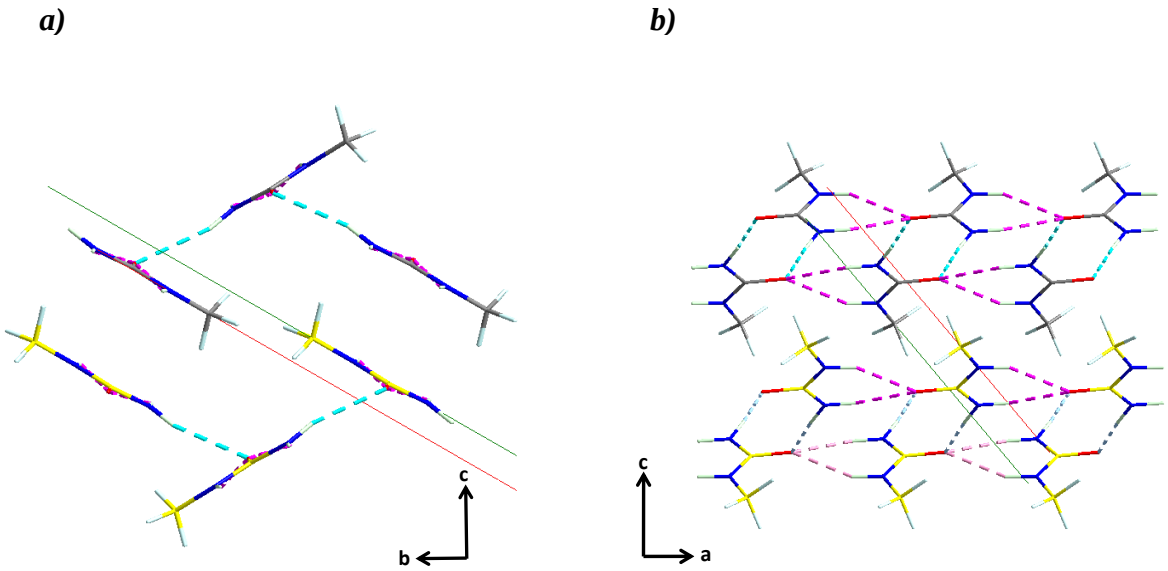

Figure IV.18 Form III along a) *a* axis and b) *b* axis illustrating a shift of methyl moieties
Carbon atoms colored in yellow correspond to the lower layer.
The green and red segments show the shift between methyl groups.

IV.5.4 Mechanism of transition from Form II to Form III

The distance between the layers in Form II was found at 3.18 Å (at -50 °C) and at 2.82 Å for Form III (at -173 °C) (Fig.IV.19).

Upon cooling the Form II, the crystal lattice is likely to get 'compressed'. The compression of the lattice of Form II upon cooling can generate steric hindrance by the methyl moieties. To overcome this issue, the layers shift to minimize the steric hindrance effect upon a slide along *c* and the diagonal *bc*. Hence, the methyl moieties will be shifted in Form III, contrary to Form II where methyl moieties are aligned (Fig.IV.20).

As shown previously, Form II and Form III present common features: they crystallize in the same space group ($P2_1/c$), they have the same asymmetric unit ($Z'=1$) and the same molecular hydrogen bonds.

Despite the poor diffusion at low temperature (-118 °C), the transition Form II → Form III (or vice versa) exhibits a good reversibility. Van der Waals contacts are different (mainly between methyl groups).

In the light of all the results, we can suggest that the transition from Form II to Form III is of first order and could be governed by cooperative shear movements. Conversely by taking into account thermodynamic data the postulated mechanism features a discontinuity proceeding through nucleation and growth.

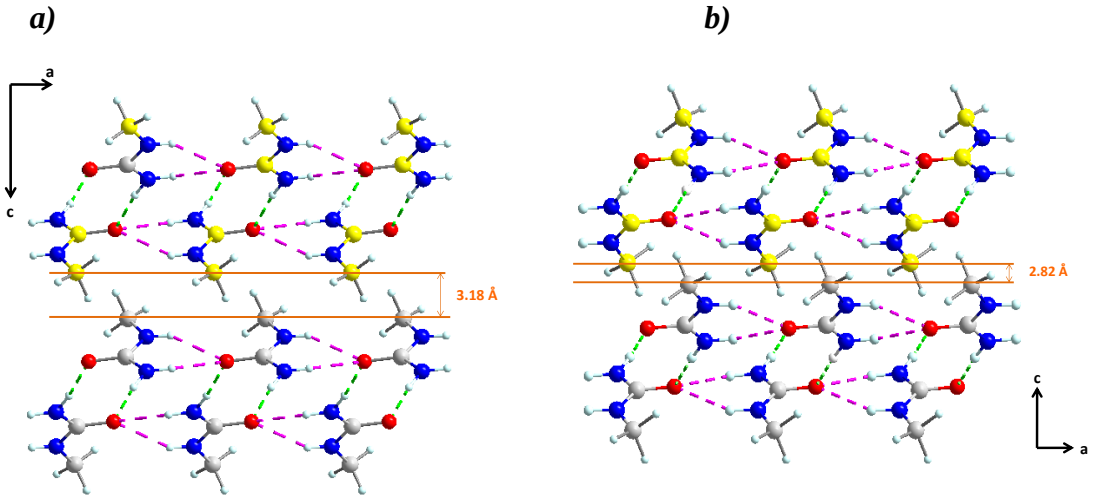

Figure IV.19 Projection along *b* of a) Form II with interplanar distance of 3.18 Å and b) Form III with interplanar distance of 2.82 Å
Carbon atoms colored in yellow correspond to the upper layer.

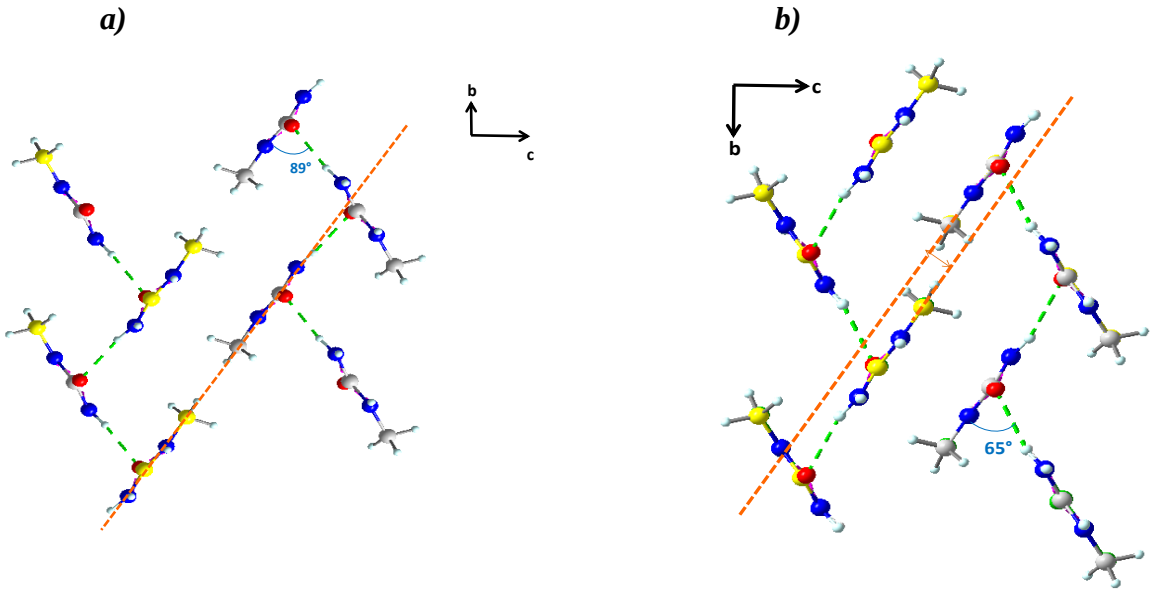

Figure IV.20 Projection along *a* of a) Form II and b) Form III illustrating a shift of methyl moieties
Carbon atoms colored in yellow correspond to the upper layer.

IV.5.5 Raman analyses

The use of Raman spectroscopy in polymorphism proved to be a useful complementary technique especially when hydrogen bonds interactions are involved and are rather to promote the difference among polymorphs. In this regard, Raman was used to provide information about the structure and conformation in the solid state by probing the vibrations of atoms where frequency shifts of the vibrational modes are detected.

Raman spectra of the commercial Form I and Form II recorded after the quenching at -50 °C and Form III recorded upon cooling at -150 °C at different zones are shown in Figure IV.21 and IV.22.The main differences observed between the three spectra are located in grey shaded areas.

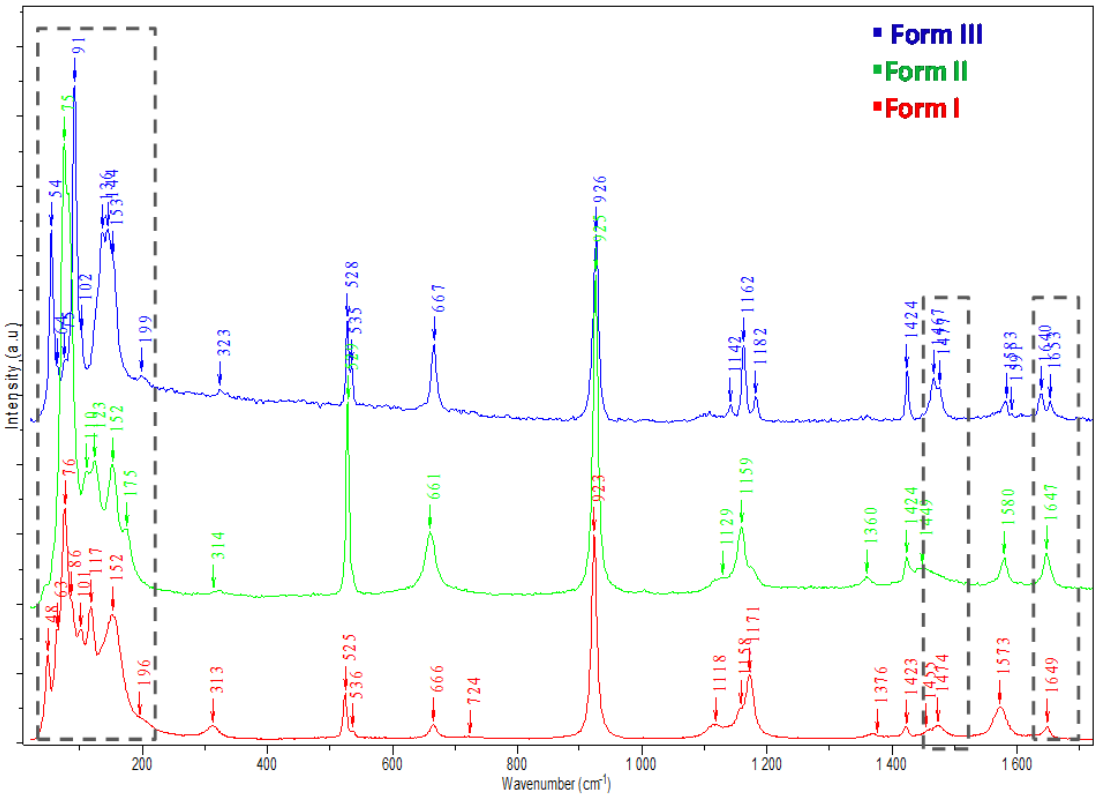

Figure IV.21 Raman spectra of Form I at 25°C (Red), Form II at -50 °C (green) and Form III at -150 °C for the zone extending from 20 to 1700 cm^{-1}

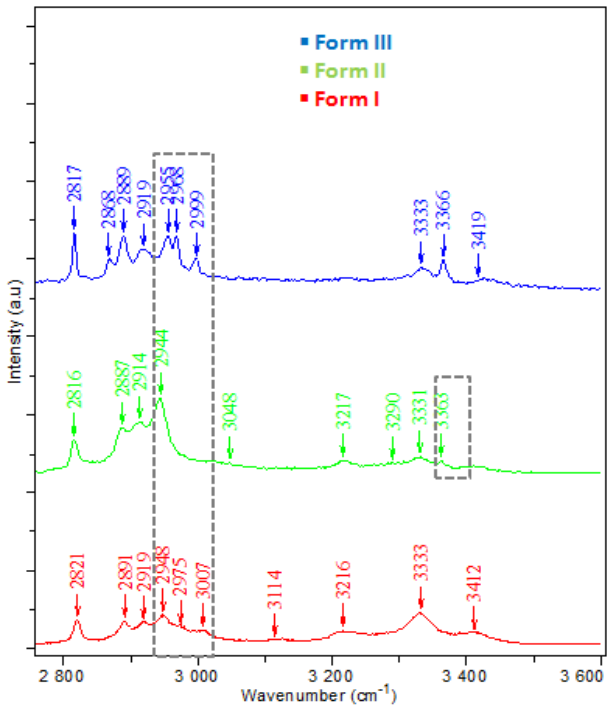

Figure IV.22 Raman spectra of Form I at 25 °C (red), Form II at -50 °C (green) and Form III at -150 °C (blue) for the zone extending from 2700 to 3600 cm^{-1}

By comparing spectra of Form I and Form II, bands located at 2975 cm^{-1}(shoulder) and 3007 cm^{-1} are not visible in Form II (Fig.IV.22). The band at 2975 cm^{-1} is assigned to an asymmetrical stretching of CH_3 group.

The spectrum of Form II shows clearly a band at 3363 cm^{-1} not present in the spectrum of Form I. This band was in the commercial form (Form I) and it is assigned to the stretching of NH (Fig.IV.22).

It seems that at -150 °C, there is formation of a new crystalline form. Changes in the appearance of crystals have been observed.

The spectrum of Form III reveals some modifications of Raman bands localized at:

1467 cm^{-1}	CH_3 asymmetric deformation
1653 and 1640 cm^{-1}	stretching C=O
2868 cm^{-1}	not assigned (appearance)
2968 cm^{-1}	CH_3 asymmetric stretching

In accordance with the structures refinement described previously, the deformation and stretching of CH_3 bonds are related to the packing change of methyl groups at -173 °C due to the compression of the lattice.

IV.5.6 Assessment of the activation energy

Two methods can be employed for the measurement of the activation energy of the conversion of Form II to Form I:

a) Non-isothermal method

The commonly theoretical model used for the determination of the activation energy E_a with the non-isothermal method is the Kissinger analysis. Kissinger's method is based on a first-order reaction [4]. In this method, the sample is heated at different heating rates and the heat flow variation is recorded as function of temperature or time. Thus, the apparent activation energy E_a can be determined. In this purpose, a melt-quenching of NMU was performed in DSC crucibles following the same heating and cooling program described in the part IV.5.2. DSC analyses were then recorded on Form II starting from - 50 °C at different heating rates ranging from 2 to 10 K/min (Fig.IV.23).

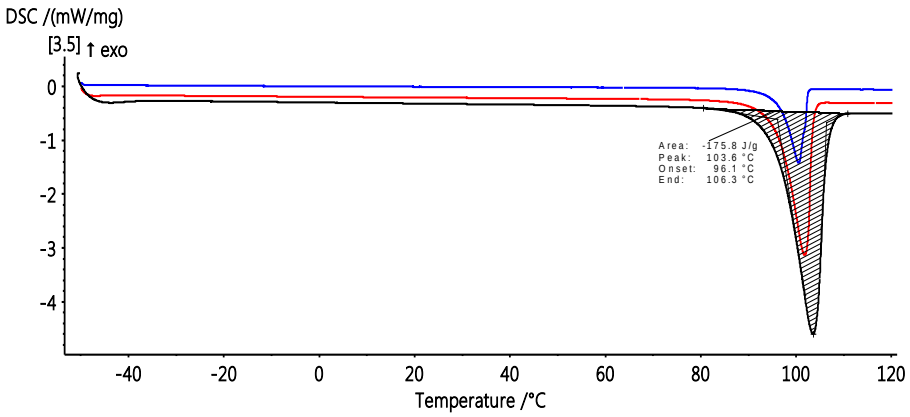

Figure IV.23 DSC heating scans of NMU form II at different heating rates 2 K/min (blue), 5 K/min (red), and 10 K/min (black)

In the three DSC curves presented in Figure IV.23, only the melting peak of Form II is observed which confirms the monotropic character of Form II. Thus, this method was not adaptable for energy activation measurement, since the transition is not detected by DSC at different heating rates.

b) Isothermal method

The activation energy E_a can be obtained under isothermal conditions from the evolution of the volume fraction $x(t)$ of the recrystallized material using the Johnson–Mehl–Avrami (JMA) transition equation [5,6] : $x(t) = 1 - e^{-k(t-t0)^n}$

with t the time of reaction, t_0 the induction time, n the Avrami exponent and k the Avrami constant.

Avrami constant depends on temperature and can be expressed with an Arrhenius law:

$$K(t) = A\, e^{-Ea/RT}$$

with A is a pre-exponential factor, E_a the activation energy of the transition, R the universal gas constant and T the temperature.

Second Harmonic Generation revealed to be an useful tool for the determination of the activation energy E_a especially when the transition is from a form that crystallizes in a centrosymmetric space group to a form that crystallizes in a non-centrosymmetric space group or vice versa[7,8]. Accordingly, the tracking of the conversion from the metastable Form II towards the stable Form I was proceeded by means of isothermal experiments with different annealing temperatures. The crystallization of Form II was achieved in the SHG crucible by following the same protocol as in DSC for the first heating up to melting and for the cooling up to - 50 °C. An annealing was then performed at 50 °C, 55 °C, 57 °C and 60 °C.

The transformed fraction x versus time was calculated as follow:

$$x = 100.\ (I_{SHG\,(T)} / I_{MAX\ SHG})$$

where:

x is the transformed fraction of the metastable Form II.

$I_{SHG\,(T)}$ is the SHG intensity measured at a given annealing temperature T.

$I_{MAX\ SHG}$ is the maximum intensity reached by SHG after total conversion of Form II to Form I at a given annealing temperature.

Figure IV.24 illustrating the evolution of the transformed fraction (x)of Form II versus time shows that the isothermal curves exhibit a classical “S” shape for transformation profile. Besides, annealings at 60 °C, 57 °C, 55 °C and 50 °C show that the total conversion from Form II to Form I (corresponding to x= 100%) is reached after 10 800s, 27600s, 33 000s and 37 200s respectively which is in agreement with kinetics.

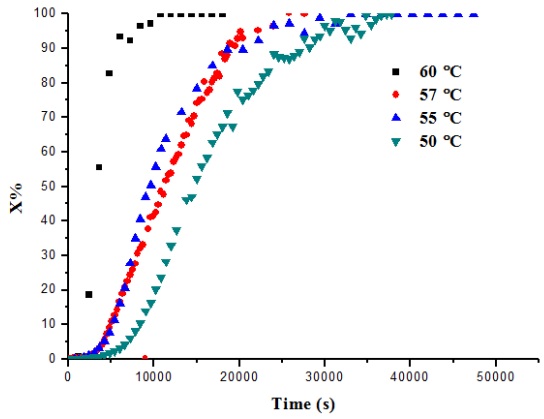

Figure IV.24 SHG results by plotting at different annealing temperatures

The first points and points of the slope are the most important parts in the fit because they have a strong influence on the Avrami parameters (n and k). Unfortunately, fluctuations of SHG signal are observed for these points (Figure IV.25). These fluctuations generate error during the fit and force the algorithm to choose bad parameters.

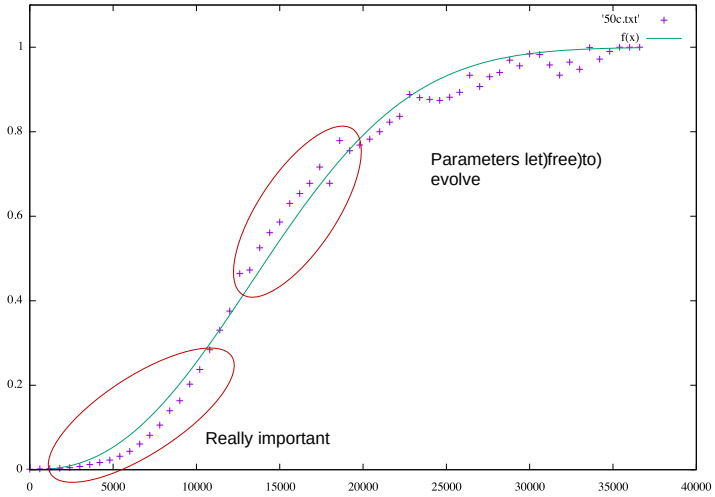

Figure IV.25 Fitting result for the 50 °C data set. All parameters are free to evolve. (k=6.30995.10^{-11} and n=2.41701)

For this reason, a manual fitting would result in a better fit for the first part of the curve but with a subsequent loss of consistency for the final part of the curve. An example of manual fit for the 50 °C data set is illustrated in Figure IV.26. It can be noticed that the fitting curve is closer for first part of the data and a lower consistency is observed for the last part of the data set.

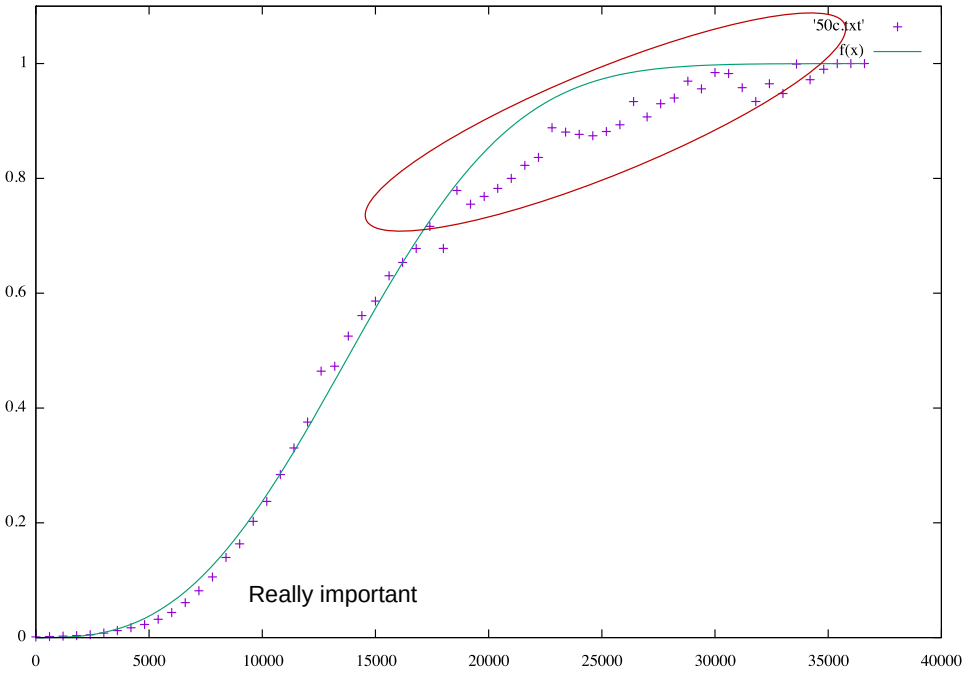

Figure IV.26 Result of the fitting for k=1.32.10^{-12} and n=2.82798.

A standard method to calculate the activation energy is to use the following equation:

$$Ln[- ln (1-x)] = ln [k (T)] + n ln (t)$$

A linear regression is then applied to plot *Ln[- ln (1-x)]* versus *ln(t)*to obtain *n* as the slope and *ln(k (T))* as the intercept.

A natural logarithm of ln (k (T)) leads to :

$$Ln [k (T)] = ln (A) - E_a / RT$$

The direct fit of experimental data for the annealing temperatures at 50 °C, 55 °C, 57 °C, and 60 °C are reported in Table IV.4. The kinetic changes are very important on a very small temperature range. Moreover, we can notice that the Avrami “n” parameter is not constant and exhibits an important variation from 1.65 to 2.82 for a small temperature range. The average n is estimated at 2.18.

Table IV.4 Direct fit of experimental data using least square method.

T (°C)	T (K)	1000/T (K^{-1})	Lnk	k	n
60	333	3.003003003	-13.17570614	1.90E-06	1.65661
57	330	3.03030303	-18.86730071	6.40E-09	1.96647
55	328	3.048780488	-20.86621977	8.67E-10	2.29148
50	323	3.095975232	-27.35114947	1.32E-12	2.82798

Finally, the activation energy E_a is obtained from the slope of the plot ln(K(T)) versus 1000/T and was found at 1234 KJ/mol with a regression coefficient $R^2 = 0.985$ (Fig.IV.27).

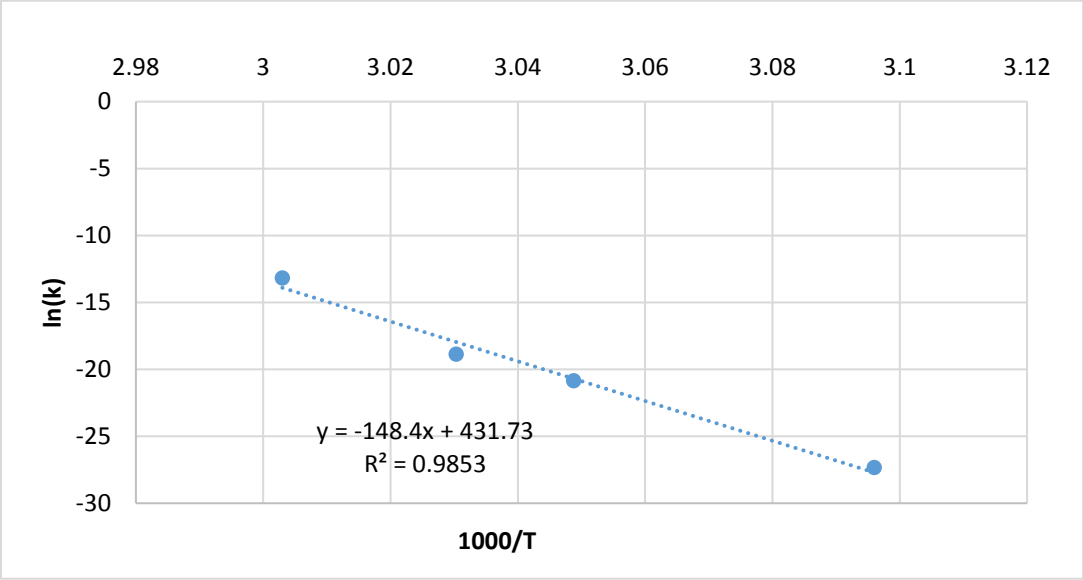

Figure IV.27 ln (k)versus 1000/T plots for isothermal transformation of Form II to Form I.

Although a mathematical fit is obtained, the activation energy is considered huge and not relevant. The relative humidity might be an additional factor which needs to be taken into account in the kinetics.

IV.6 Conclusion

The study of the behavior of NMU in Spray Drying with different alcoholic solvents showed that a mixture of two phases is obtained: stable and metastable forms. By increasing the inlet temperature, the metastable form disappeared: only characteristic peaks of the stable form I of NMU were detected. Melt crystallization was successfully applied to access to the metastable structurally pure Form II.

The conduction of experiments of NMU in capillaries at low temperature has generated new polymorphs of NMU which were detected by X-ray powder diffraction. The results were completed by DSC analyses and Raman spectroscopy. With the support of Rietvield refinements, it has been proven that Form II and III crystallize in the centrosymmetric space group $P2_1/c$. Besides, DSC analysis showed on the one hand that Form II and Form III interconvert reversibly at low temperature (circa -118 °C), and on the other hand that Form I and II are monotropically related with melting points at 98 °C and 95.2 °C respectively, with $\Delta H_F^I > \Delta H_F^{II}$.

Attempts to determine the activation energy with Avrami equation with the support of SHG analyses at different annealing temperatures show that Avrami model is not adaptable for this system since the value activation energy was found much too important.

REFERENCES

1. Shepherd, E. E. A., Sherwood, J. N., & Simpson, G. S. (1996). The growth and perfection of organic non-linear optical crystals: N-methyl urea (NMU) from methanol solution. III. The growth of large single crystals for optical examination. *Journal of crystal growth*, *167*(3), 709-715.

2. Corey, R. B., & Wyckoff, R. W. (1933). On the Structure of Methyl Urea.*ZeitschriftfürKristallographie-Crystalline Materials*, *85*(1), 132-142.

3. Huiszoon, C., &Tiemessen, G. W. M. (1976). Monomethylurea: a redetermination. *ActaCrystallographica Section B: Structural Crystallography and Crystal Chemistry*, *32*(5), 1604-1606.

4.H. Kissinger (1957), Reaction kinetics in differential thermal analysis Anal. Chem., 29 pp. 1702–1706.

5.M. Avrami (1939), Kinetics of phase change. I. General theory J. Chem. Phys, 7 pp. 1103–1112.

6.M. Avrami (1940), Kinetics of phase change: II. Transformation–time relations for random distribution of nuclei J. Chem. Phys., 8 pp. 212–224.

7.M. AvramiGranulation, phase change, and microstructure kinetics of phase change.III (1941), J. Chem. Phys., 9 pp. 177–184.

8.S. Clevers, F. Simon, M. Sanselme, V. Dupray, G. Coquerel (2013) Monotropic Transition Mechanism of *m*-Hydroxybenzoic Acid Investigated by Temperature-Resolved Second Harmonic Generation *Cryst. Growth Des.*, *13* (8), pp 3697–3704.

Chapter V

Olanzapine

V.1 Introduction

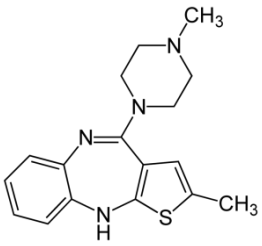

Figure V.1 Molecular structure of Olanzapine

Olanzapine (hereafter OLZ), 2-methyl-4-(4-methyl-1-piperazinyl)-10H thieno [2,3b] [1,5] benzodiazepine, is a psychotropic agent that belongs to the thienobenzodiapezine class[(1)]. It is indicated for the treatment of schizophrenia [(2)], bipolar disorder [(3)], mild anxiety and other psychoses. OLZ, with the molecular structure shown in Figure V.1, has a low solubility in water [(4)] (0.0942 mg/mL at 20 °C) and high solubility in organic solvents such as acetone and ethanol.

OLZ can crystallize in 64 solids including 3 anhydrates, 5 hydrates: dihydrates B, D, E & higher hydrate and 56 solvates and heterosolvates [(5)].

The following nomenclature will be adopted for the three anhydrates in reference to the patent EP 0733635 A1 [(6)]:

- form I referring to the metastable form of OLZ (CSD refcode: UNOGIN02)
- form II referring to the stable form of OLZ (CSD refcode: UNOGIN)
- form III will be assigned to a new metastable form in reference to a recent study [(7)].

Solubility is an important factor affecting the absorption of drugs and their therapeutic effectiveness. Poor bioavailability is a significant problem encountered in the pharmaceuticals containing an active ingredient that is poorly soluble in water like OLZ.

Processes to improve the solubility of a water poorly-soluble drug can include: crystallization of co-crystals, Spray Drying, High energy milling (HEM) processes. Spray Drying and HEM processes can result in amorphous materials or metastable phases with reduced particle size thus better solubility of drug substances. Besides, desolvation of solvates and using water-soluble carriers to form inclusion complexes can also be alternative methods to enhance the solubility of the drug [(8)].

One of the primary objectives of this study was to prepare the metastable form I of OLZ. Different processes have been adopted to reach that goal. The first method consisted in

preparing a new solvate as an intermediate step that should be valuable to get the form I after desolvation.

The second method consisted in performing Spray Drying experiments. The last method relied on grinding OLZ by High Energy Milling (HEM).

V.2 Characterization of the commercial batch of OLZ

The commercial batch of OLZ was subjected to several analyses including X-ray powder diffraction, TG-DSC and DVS.

V.2.1 X-ray powder diffraction of the commercial OLZ

The diffraction pattern confirms that the received batch contains a mixture of two phases: form II and a dihydrate. In fact, the comparison between the calculated pattern of the form II and the experimental shows additional peaks marked in black dots in the pattern of received batch (Fig.V.2).

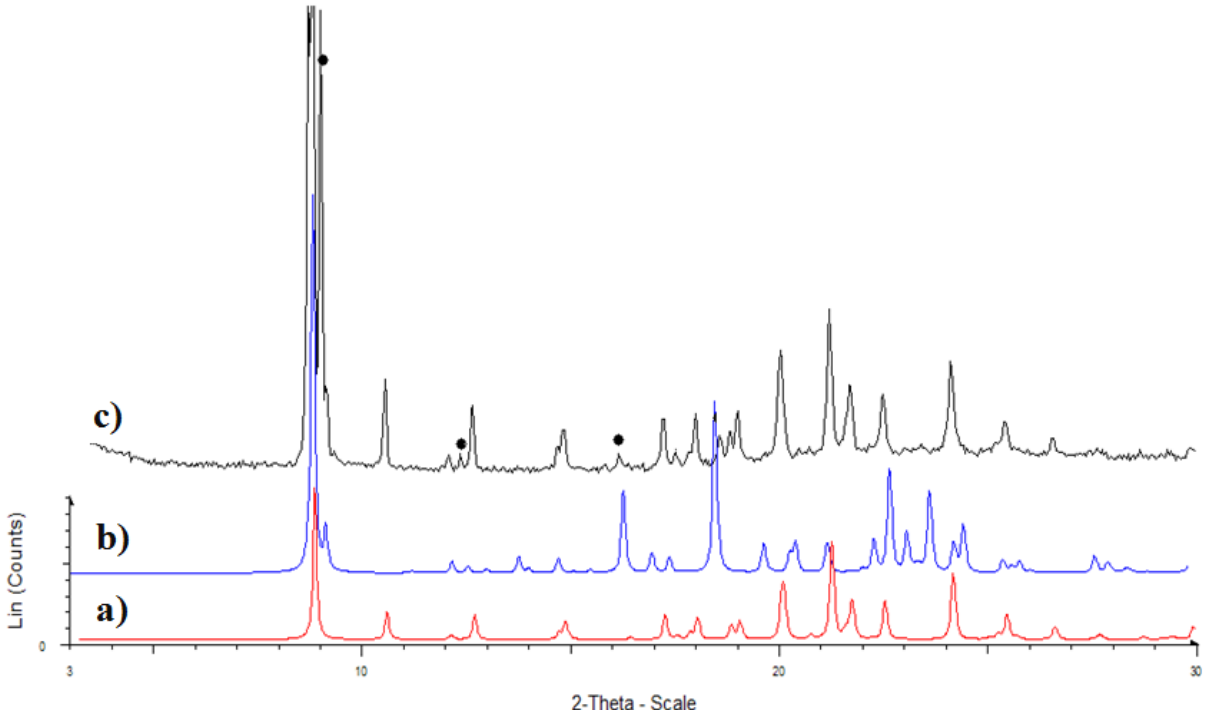

Figure V.2. Superimposition of calculated XRPD patterns of a) form II b) OLZ dihydrate and c) experimental XRPD pattern of the received batch with black dots referring to characteristic peaks of the dihydrate

V.2.2 Thermal analysis on the commercial OLZ

DSC analysis performed on the received batch shows an intense endothermic peak at 194.5 °C which corresponds to the melting point of Form II. Before this melting point, a slight deviation from the baseline is observed in the range temperature 60-100 °C. This deviation is depicted to the departure of a solvent (water).

On the other hand, the data collected on TG reveals a mass change of 2.41% which confirms that the batch is not anhydrous and contains water inside its structure (Fig.V.3)

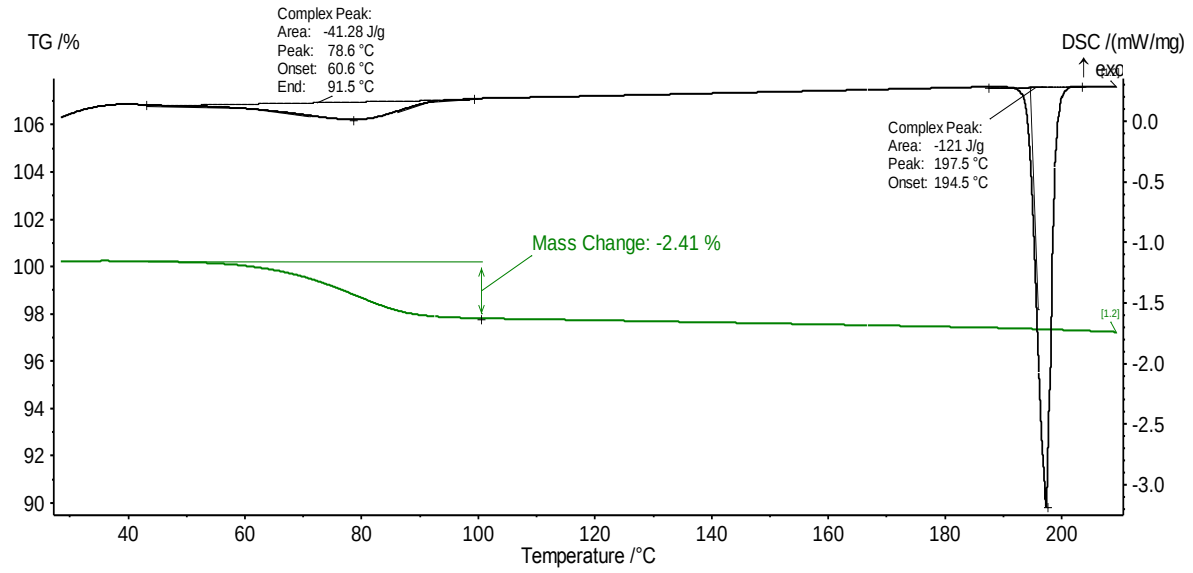

Figure V.3 TG-DSC curves of the commercial batch

V.2.3 Dynamic vapour sorption (DVS) on the commercial OLZ

Prior analysis, the commercial batch was dried under the pure nitrogen. The mass loss was estimated to 2.5 % in agreement with the value obtained in TG result.

By varying the vapour concentration around the anhydrous batch from 0 to 98% RH, an insignificant mass change (0.3 %) was detected.

The transformation from anhydrous OLZ into a hydrated phase seems to be pronounced with a RH value higher than 98 % where a mass increase (higher than 5 %) is detected.

Based on these results, it is concluded that OLZ is not a hygroscopic compound. Consequently, water found in the received batch was not due to air humidity contamination via the hygroscopicity of the compound. In fact, the water molecules are included in the crystal structure (Fig.V.4).

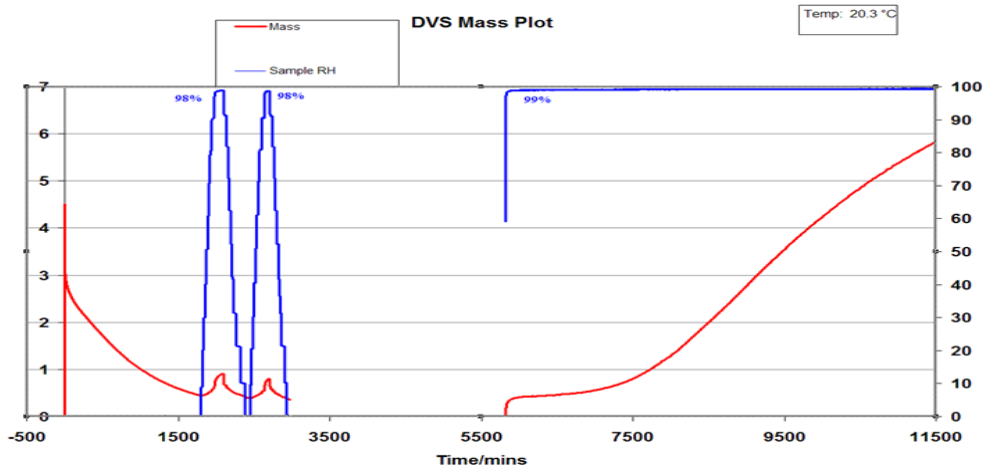

Figure V.4 DVS analysis of the commercial batch

V.3 Purification of the batch

Purifying the commercial batch consisted in mixing it with the solvent ethyl acetate (EA) and stirring the suspension overnight at room temperature. Thereafter the suspension is filtrated under vacuum and examined by X-ray powder diffraction and TG-DSC.

V.3.1 X-ray powder diffraction of the purified batch

X-ray pattern shows that the crystalline structure is similar to the calculated pattern of the form II which means that after slurrying the batch with ethyl acetate, anhydrous form II is obtained (Fig.V.5).

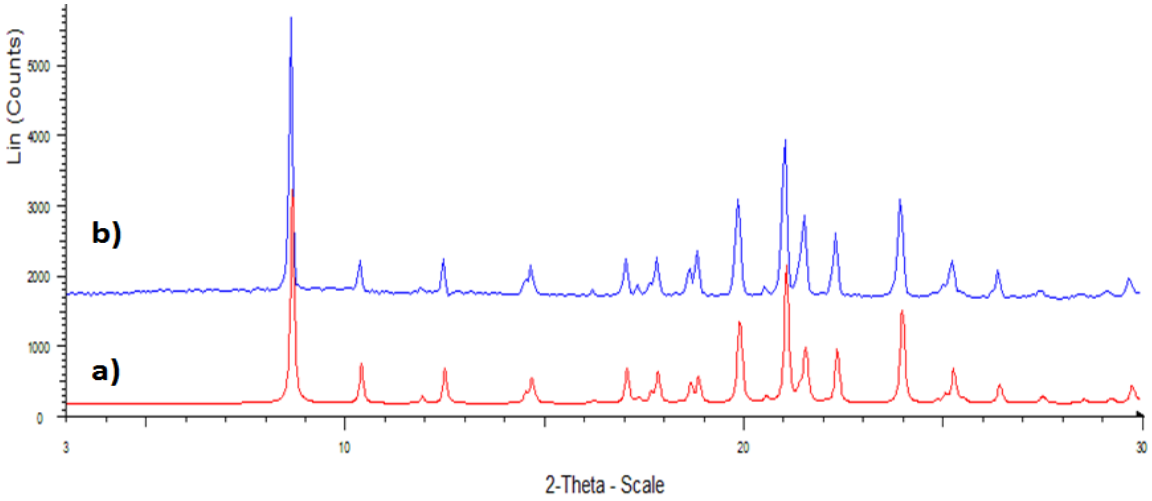

Figure V.5. Superimposition of a) calculated XRPD pattern of form II and b) experimental XRPD pattern of the purified batch

V.3.2 Thermal analysis of the purified batch

The DSC curve shows the melting point at 194.9 °C. Thus the melting point of the purified OLZ is 0.4 °C higher than the melting point of the as-received sample. After slurrying the

batch with ethyl acetate, no mass loss was detected by TGA analysis. Accordingly, the purified batch is considered as an anhydrous sample (Fig.V.6).

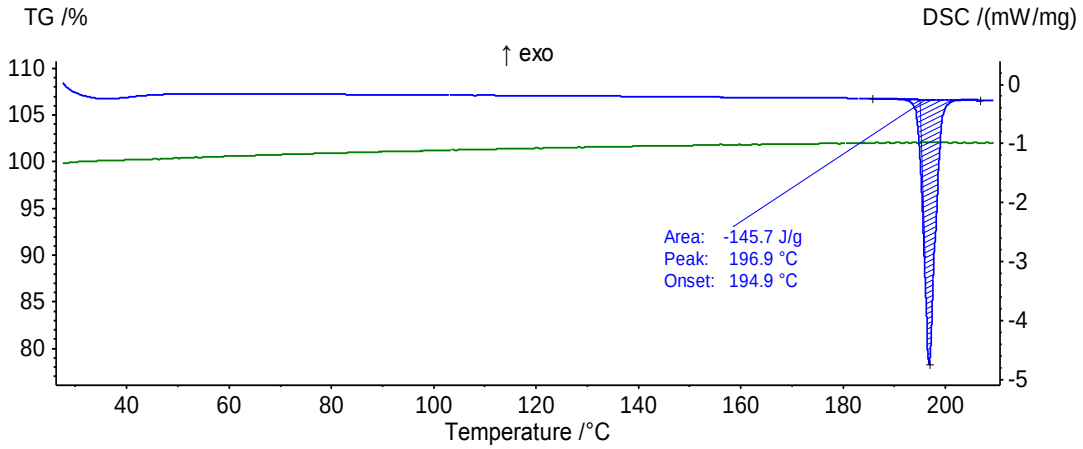

Figure V.6 TG-DSC curves of the purified batch

V.4 New solvate of Olanzapine

OLZ was crystallized from 16 solvents and mixtures of solvents with the aim of getting a new solvate. The experiments consisted in suspending the purified OLZ with new solvents and mixture of solvents then filtrating the suspension and analyzing by X-Ray to certify the formation of a solvate. The biggest challenge was to find a solvent free to access in respect with all the claims of the 30 registered patents on OLZ.

Table.V.1 resumes the results of the different tested solvents with OLZ.

Table V.1. Results of the suspensions with different solvents

Solvents	**Phase obtained**
2 Met THF	Form II
2 Met THF + Acetone	Form II
2 Met THF +Ethanol + Acetone	Ethanol solvate
2 Met THF + Ethanol + Water	Bisolansapine ethanolate dihydrate
2 Met THF + Acetone + Water	Bisolansapine ethanolate dihydrate
2 Met THF + Acetone + Ethanol+ Water	Bisolansapine ethanolate dihydrate
Dimethyl carbonate	Form II
Diethyl carbonate	Form II
Dimethyl carbonate + Diethyl carbonate	Form II

Solvents	**Phase obtained**
Dimethyl carbonate + Diethyl carbonate + Dichloromethane	Form II
Propiophenone	Form II
Butanone	Form II
Ethyl phenylacetate	Form II
Pinacolone	New phase
Pinacolone + THF + water	THF: water solvate
Pinacolone + Ethanol	Ethanol solvate
1,2-dichloroethane	Form II
Diethyl ether	Form II
Isopropyl acetate	Form II
Isobutyl acetate	Form II

A new phase was obtained by suspending the purified OLZ (form II) with pinacolone (hereafter pin) chemically known as Methyl tert-butyl ketone and was further characterized by X-Ray powder diffraction, TG-DSC and ^{1}H NMR.

V.4.1 X-ray powder diffraction on the new solvate

Figure V.7.b illustrates the X-ray powder diffraction pattern of the new phase. Thus, the appearance of new peaks compared to Form II raises the hypothesis of the formation of a new pinacolone solvate.

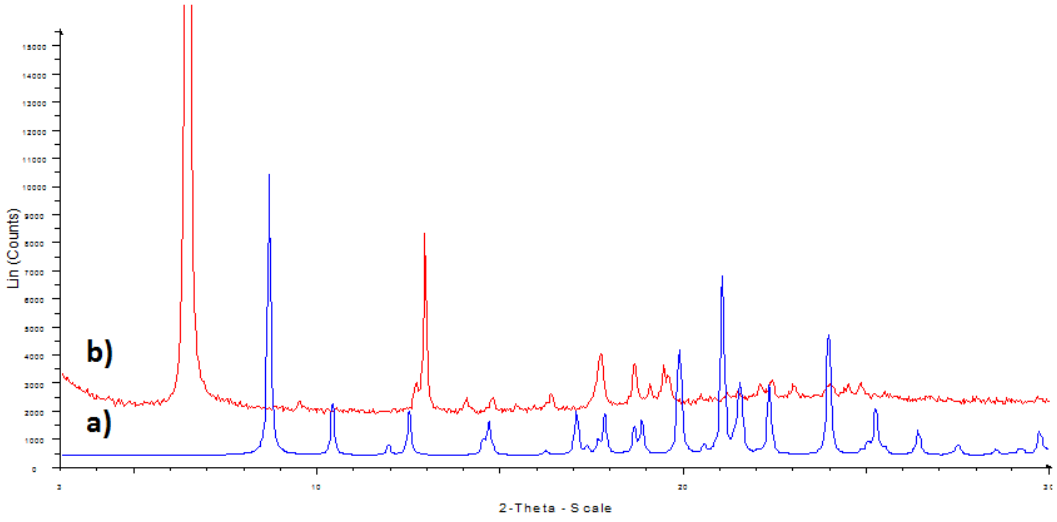

Figure V.7 Superimposition of a) calculated XRPD pattern of Form II and b) the experimental XRPD pattern of a new phase obtained with pinacolone

It was interesting to determine the crystal structure of the new phase. Attempts to get single crystals were carried out with pinacolone solvent. The poor quality of the single crystals was an obstacle for the crystal structure determination (see Appendix E). Hence, it can be deduced that the new phase is an heterosolvate OLZ:Pinacolone:water. It was difficult to determine the stoichiometry due to the efflorescence of the solvate.

V.4.2 Thermal analysis on the new heterosolvate OLZ: Pin:water

The thermal behaviour of this new phase was studied by TG-DSC.

The sample was introduced in a pierced crucible and heated at 5 K/min. The DSC curve (Fig.V.8) shows an intense endothermic peak at 194.7 °C corresponding to the melting point of the anhydrous phase and a significant deviation from the base line is noticed in the temperature range 40 -85 °C. This significant deviation is assigned to a desolvation peak.

The data obtained in TG shows that there is 24.6 % weight loss in the sample. This percentage of desolvation is assigned to the loss of pinacolone and water with reference to mass spectroscopy data coupled to the TG-DSC (data not shown).

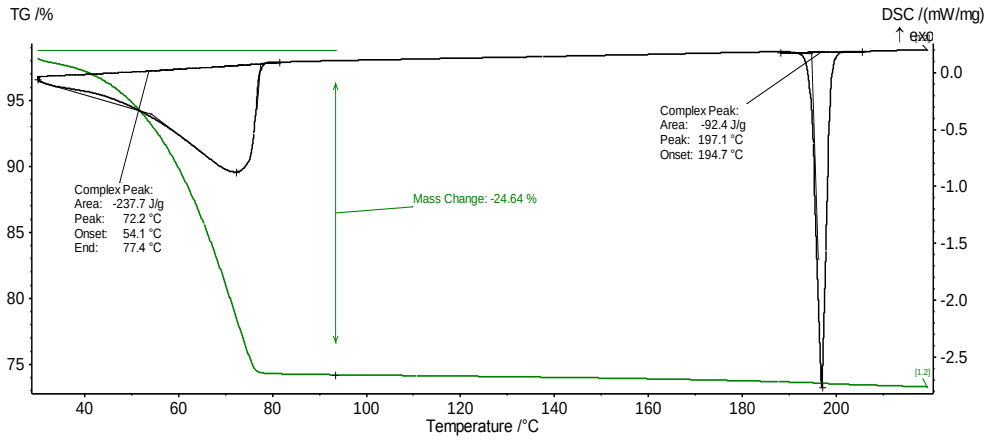

Figure V.8. TG-DSC curves of the heterosolvate OLZ:Pin:water

V.4.3 Proton NMR on the new solvate OLZ: Pin

^{1}H NMR was also used to characterize this new solvate. Integration of peak areas confirms the molar ratio OLZ: pinacolone 1:1 without any chemical degradation (Fig.V.9)

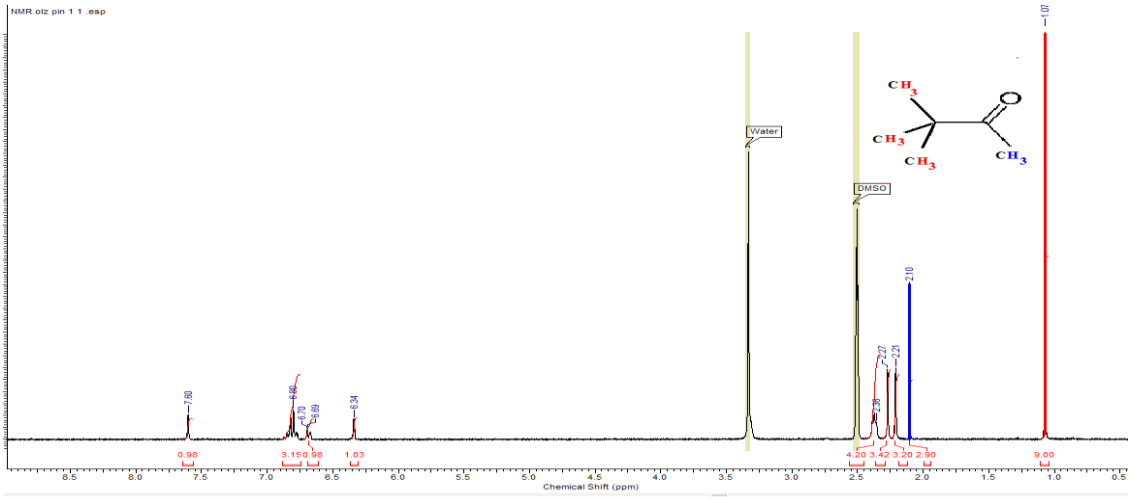

Figure V.9 ^{1}H NMR spectrum of the solvate OLZ:Pin in DMSO-d6

V.4.5 Desolvation of the new heterosolvate OLZ: Pin: water

Many processes were applied to remove the pinacolone and water including vacuum at room temperature, vacuum at 50 °C, Rotavap and solvents vapours.

Unfortunately, results obtained by X-ray analysis showed that in all the processes the desolvation led to the form II (Fig.V.10).

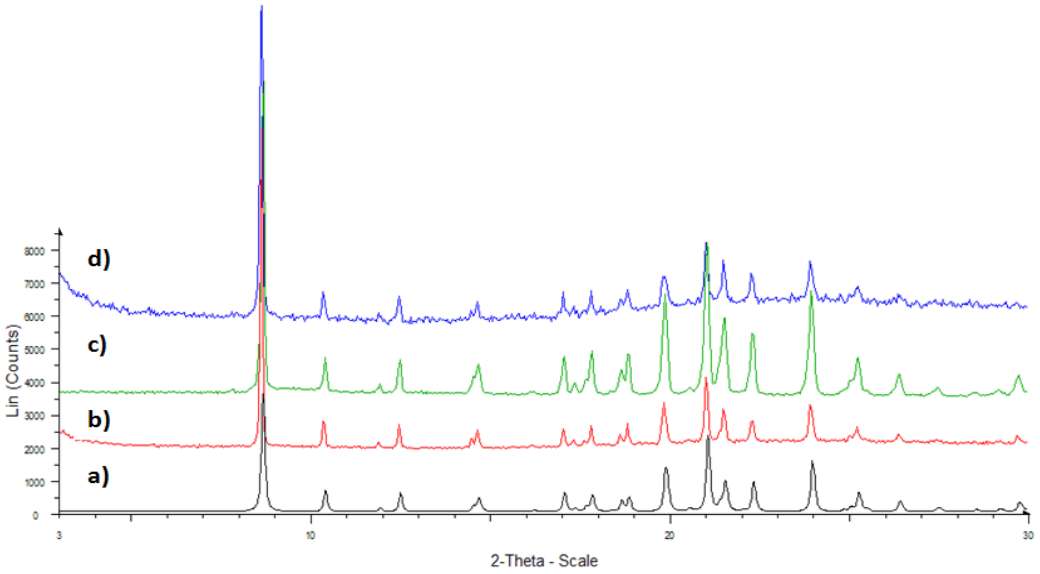

Figure V.10 Superimposition of a) calculated XRPD pattern of Form II and the experimental XRPD pattern after desolvation of OLZ: Pin:water by b) Rotavap c) Vacuum at room temperature d) Vacuum at 50 °C

Literature review on desolvation of OLZ solvates and heterosolvates shows that almost all the solvates and heterosolvates of OLZ will give rise to Form II upon desolvation, except

dichloromethane solvate was found by X-ray diffraction analysis to be amorphous and, on heating during DSC analysis, allowed the crystallization of both form I and III [9].

V.5 Spray Drying of OLZ

Spray Drying experiments were carried out by dissolving 0.5 g of OLZ in 100 mL of green solvents: Dimethylcarbonate (DMC) (b.p= 90 °C) and diethylcarbonate (DEC) (b.p 128 °C). The reason behind choosing these solvents is because they are free to access. In fact, a patent issued in 2007 discloses the access of Form I of OLZ by Spray Drying with a list of organic solvents including alcohols, ketones, esters and other organic solvents [10].

The first series of experiments were performed in a closed loop; the inlet temperature was fixed at 100 °C for the solution containing DMC and 130 °C for the solution containing DEC. The dried powders were directly analyzed by X-ray after being collected (Fig.V.11.b-c)

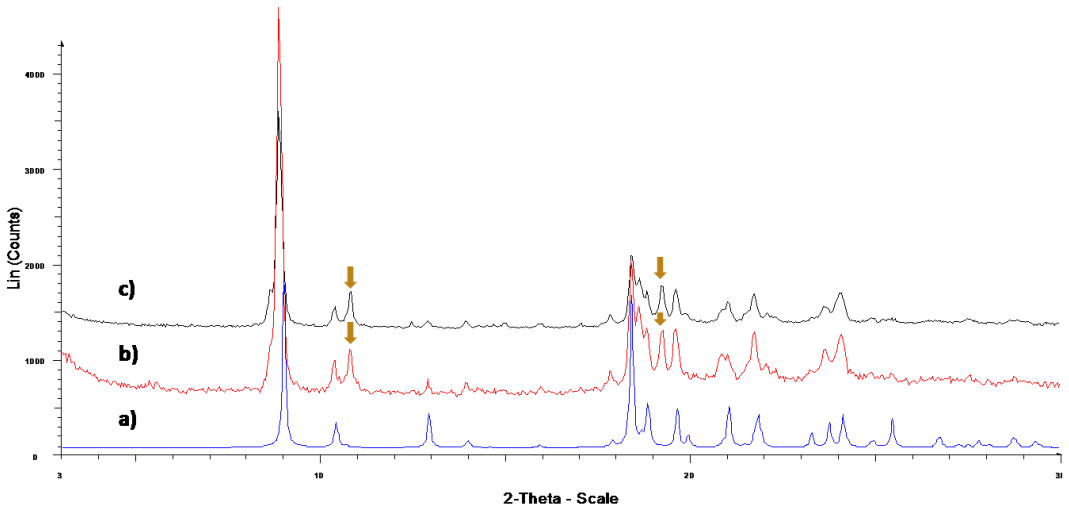

Figure V.11. Superimposition of a) calculated XRPD pattern of the form I and the experimental XRPD pattern of the spray-dried OLZ with b) diethylcarbonate T_{in} = 130 °C
c) dimethylcarbonate T_{in}= 100 °C with arrows referring to Form III

The spray-dried samples exhibit characteristic diffraction peaks corresponding to Form I, thus 2 peaks at 2θ = 10.8 ° and 19.5° (marked in arrows) are detected and they refer to Form III.

Spray drying parameters were tuned to access to the pure targeted form. For this reason, inlet temperature was increased to 180 °C for both solutions.

Figure V.12 b-c illustrates the experimental XRPD of spray-dried OLZ obtained with DMC and DEC at T_{in} = 180 °C. X-ray patterns of the powder show a mixture of two metastable forms: form I and form III (Fig.V.12 b-c).

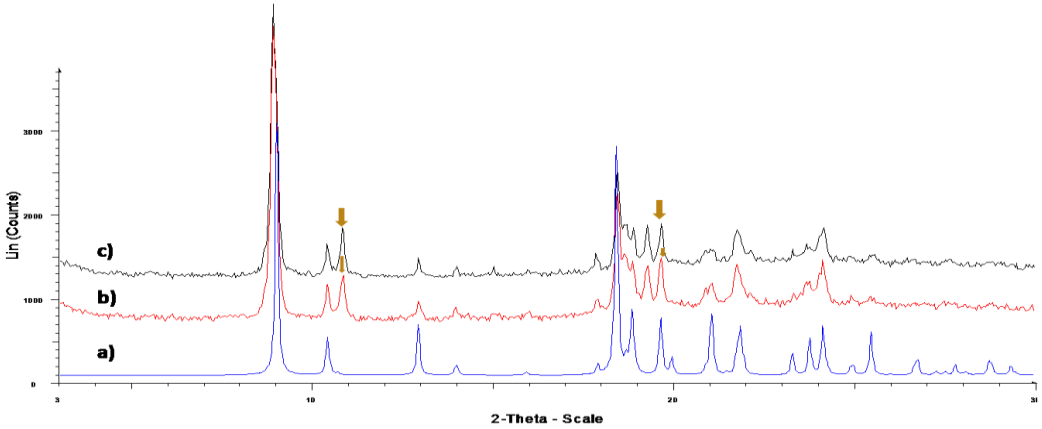

Figure V.12. Superimposition of a) calculated XRPD pattern of the form I and the experimental XRPD pattern of the spray-dried OLZ with T_{in} = 180 °C b) diethylcarbonate c) dimethylcarbonate with arrows referring to Form III

V.6 Neat milling and LAG on the purified batch

1g of purified OLZ were placed in a vial and subjected to HEM. Liquid assisted grinding (LAG) was carried out by adding few drops of ethanol in an another vial containing OLZ.

After 12 hours of milling at 4 °C with balls turning at 400 rpm, the powder was subjected to X-Ray analysis. Figure V.13 shows that a mixture of Form I and II is obtained by both neat milling and LAG milling. The peaks are noticed to be broader than the initial diffraction peaks which could be assigned the particle size reduction concomitant with a decrease in the quality of the long range order.

In reference to a patent [(11)], an amorphous form of OLZ is obtained by melt-quenching, thus the glass transition of OLZ was found at 66 °C. This value is agreement with studies showing that that the ratio T_g/T_m is usually close to 2/3 for organic and pharmaceutical compounds [(12)]. Hence, no amorphous form was obtained either by neat milling or by LAG. This can be due either to an overheating inside the vials during the milling process resulting in a local temperature above the glass transition or to the fast recrystallization of OLZ after milling.

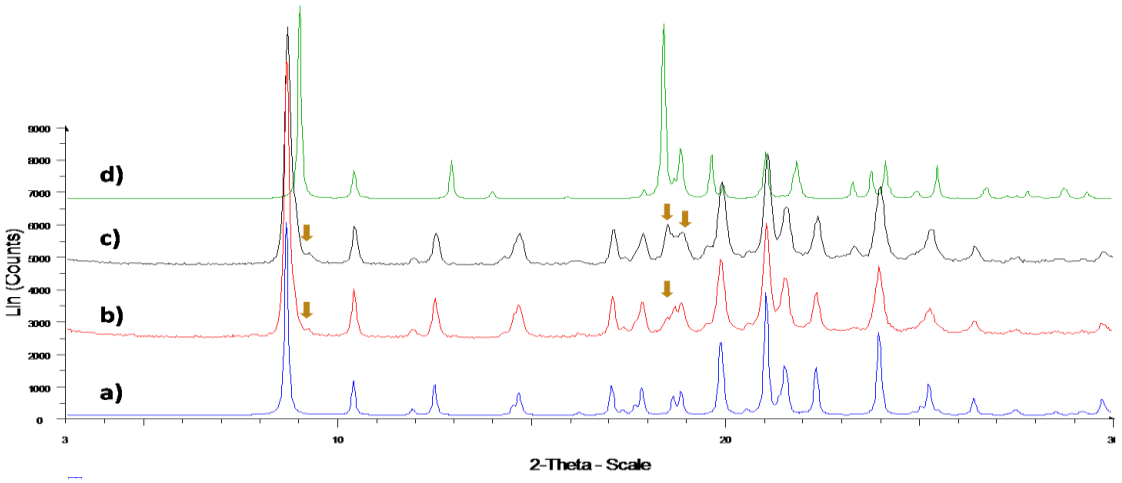

Figure V.13 Superimposition of a) calculated XRPD pattern of Form II b) the experimental XRPD pattern of OLZ b) after neat grinding c) after LAG with arrows referring to Form I d) calculated XRPD pattern of Form I

V.7 Conclusion

Several methods were applied to access to the pure metastable form I of OLZ. These methods included preparation of a solvate followed by a desolvation, spray drying and High Energy Milling.

The results obtained in the present study showed that the desolvation process of the heterosolvate Olz: pinacolone:water was unsuccessful for getting Form I. Hence, Form II was obtained by every desolvation method applied.

Neat milling and liquid assisted grinding of OLZ gave access to a mixture between Form I and Form II.

Spray drying is so far the only promising technique to obtain the metastable form of olanzapine. In fact, the green solvents used in spray drying experiments, are not protected in any claims.

However, even by adjusting Spray Drying parameters (inlet temperature of the drying gas) the final product consisted of a mixture of two metastable forms (Form I and form III).

REFERENCES

1.Beasley CM Jr, Tollefson GD, Tran PV, Efficacy of olanzapine: an overview of pivotal clinical trials The Journal of Clinical Psychiatry , 1997, 58 Suppl 10:7-12.

2.Susan L McElroy, Mark Frye, Kirk Denicoff, Lori Altshuler, Willem Nolen, Ralph Kupka, Trisha Suppes, Paul E Keck, Jr, Gabrielle S Leverich, Geri F. Kmetz, Robert M Post Olanzapine in treatment-resistant bipolar disorder Journal of Affective Disorders Volume 49, Issue 2, 1998, Pages 119–122.

3.Poyurovsky, Michael; Pashinian, Artashes[a]; Levi, Aya; Weizman, Ronit; Weizman, Abraham The effect of betahistine, a histamine H1 receptor agonist/H3 antagonist, on olanzapine-induced weight gain in first-episode schizophrenia patients International Clinical Psychopharmacology: 2005 - Volume 20 - Issue 2 - pp 101-103.

4. Adamo F, Cristina C, and Giancarlo C. Design of Olanzapine/Lutrol Solid Dispersions of Improved Stability and Performances. Pharmaceutics 2013; 5: 570-590.

5.Susan M. Reutzel-Edens , Julie K. Bush , Paula A. Magee , Greg A. Stephenson , and Stephen R. ByrnAnhydrates and Hydrates of Olanzapine: Crystallization, Solid-State Characterization, and Structural Relationships *Crystal Growth & Design*, 2003, *3* (6), pp 897–907.

6. EP 0733635 A1 Charles Arthur Bunnel *et al.* 1996

7. R. Bhardwaj , L. Price, S. Price , S. Reutzel-EdensG. Miller, I.Oswald, B. Johnston , and A. Florence Exploring the Experimental and Computed Crystal Energy Landsape of Olanzapine J. Crystal Growth & Design 2013

8. Mudit Dixit, R. Narayana Charyulu, Anupama Shetty, Narayana Charyalu, Meghana Rao, Pallavi Bengre, Sharin Thomas Department Enhancing Solubility and Dissolution of Olanzapine by Spray Drying Using β-Cyclodextrin Polymer Journal of Applied Pharmaceutical Science Vol. 4 (11), pp. 081-086, November, 2014

9. Cavallari C, Santos BP, Fini A. Olanzapine solvates.J Pharm Sci. 2013 Nov;102 (11)

10. IPCOM000158856D, 2007

11.EP 1633757 A1, 2006

12. Kerc, J., & Srcic, S. (1995). Thermal analysis of glassy pharmaceuticals.*Thermochimica acta*, *248*, 81-95.

General Conclusion

Experimental studies investigated in this thesis highlighted different cases of polymorphism that can be encountered in the field APIs and organic molecules. Each case revealed some aspects of the solid-state behaviour.

The use of the Spray drying appears a promising process to quantitatively access to a structurally pure metastable form API (γ form of Pyrazinamide (PZA)). Co-spray drying experiments of PZA with various excipients were carried out in order to block the return to thermodynamic equilibrium of this metastable γ form that normally undergoes a phase transformation during few days of storage at room temperature. Among all the tested excipients, 1,3-Dimethylurea (DMU) Form I (i.e. the high temperature form) has been shown to be the specific additive able to block this transition for, at least, two years. By using a phase diagram approach no detectable partial solid solution has been evidenced between PZA and DMU. Hence, the stabilization mechanism must proceed through a surface effect. Moreover, co-spray drying PZA with PVP resulted in the crystallization of δ PZA unchanged for 24 months of storage at room temperature.

The *in-situ* X-Ray analyses served to confirm the existence of a metatectic invariant in the DMU-water binary system with the presence of 0.15 % molar in water. This finding explains the discrepancy between the solid-solid phase transition found at 41 °C in literature and at 25 °C by using TR-X-Ray analysis. With the support of data obtained by several different techniques such as: *in-situ* X-Ray analyses, TR-SHG, DSC and refractometry, the whole binary phase diagram DMU-water has been investigated. A monohydrate has been identified with a non-congruent fusion at 8 °C.

The study of the polymorphism of N-Methylurea (NMU) by Spray Drying provided the first hint of the existence of a metastable form. Other crystallization processes including neat and liquid assisted grinding and melt-crystallization aimed at getting the metastable form structurally pure. Original results were obtained by melt crystallization of NMU: two new polymorphic forms (Form II and III) were obtained at different quenching temperatures with a reversible solid-solid transition at circa -118 °C. Comparisons between the crystal structures of Forms II and III, reveal extensive similarities between these two crystal structures. A mechanism is suggested to explain the reversible conversion at low temperatures: the transition seems to be of first-order phase transformation where there is a discontinuity change in entropy and enthalpy with a small but significant hysteresis effect. The

transformation could take place by nucleation and growth featuring limited shear movements and a self-templating effect.

Olanzapine (OLZ) was investigated by Spray Drying, HEM and LAG with the aim to improve its solubility by getting access to the metastable Form I. Attempts of solvates screening resulted in the identification of a new heterosolvate with: pinacolone and water. The desolvation gives rise to the stable form II. So far, Spray Drying was the only process giving access to mixtures of Form I and III with two green solvents: dimethylcarbonate and diethylcarbonate.

The perspectives following this thesis would be to determine the crystal structure of the monohydrate of DMU by X-Ray powder diffraction and the stable eutectic composition between the monohydrate and ice by TR-SHG.
Since many parameters (including the relative humidity) can affect the SHG signal, it would also be interesting to optimize the assessment of the activation energy of NMU Form II to Form I by controlling the water content that seems to impact on the kinetics of conversion during TR-SHG measurements. For this reason, coupling TR-SHG with a RH control device can be an alternative solution.
Finally, the epitaxial effect between PZA γ form and DMU Form I will be evaluated with adequate software taking into account two bidimensional lattices with the calculated interfacial energies.

Appendices

Analytical techniques description

In order to characterize polymorphs, amorphous, solvates and hydrates, traditional techniques such as X-ray diffraction, Differential Scanning Calorimetry, TG-DSC, Raman spectroscopy, Scanning Electron Microscopy and Second Harmonic Generation are commonly used. Part A of the appendices will be devoted to explain the principles of these techniques. Part B will be devoted to provide information about Nuclear Magnetic Resonance and Karl Fischer techniques. Parts C, D and E are supplementary results related to this thesis.

A.1 X-ray Diffraction (XRD)

X-rays are electromagnetic waves discovered in 1895 by the german physicist Röntgen who was awarded the Nobel Prize in Physics for this achievement. In 1912, Max von Laue discovered that a crystal diffracts the light if the wavelength is of the same order as the interatomic distance and if the arrangement of the atoms is in an ordered, periodic structure.

As described previously, crystals are long-range-ordered periodic structures, they can be considered as a series of planes spaced with an equal interreticular distance called « d_{hkl} ».

An x-ray's beam hits the surface of the crystal at an angle θ which is called the scattering angle or Bragg angle. Diffraction of an x-ray beam occurs when two waves interfere constructively. This condition is verified when the pathlength difference between two waves undergoing intereference given by $2d\sin\theta$is an integral number of the incident wavelength λ.

This leads to Bragg's law, which describes the condition on θ for the constructive interference:

$$\mathbf{2d_{hkl}\sin\theta = n\,\lambda}$$

where n is the diffraction order and λ is the wavelength of the X-Ray beam.

Since its discovery, X-ray technique is considered as an important technique because it deepens the understanding of the structure of matter in different areas of applications. Indeed, an X-ray powder diffractogram is considered as the fingerprint of a crystalline solid and is commonly used for the identification of polymorphic forms. Besides, a structural model can be refined from XRPD patterns.

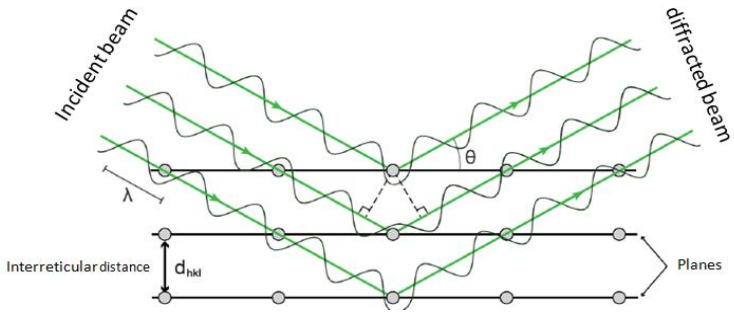

Figure A.1 Principle of X-Ray Diffraction

X-ray powder diffraction

X-ray powder diffraction measurements were carried out on D8-ADVANCE (BRUKER) X-ray diffractometer equipped with a copper anticathode. The diffraction patterns were collected by steps of 0,04° over the angular range 5-50° with a counting time of 0,5s per step. The characteristic powder diffraction peaks are expressed in degrees 2-theta.

The calculated patterns of the crystalline compounds presented in this study are obtained from the crystalline structures, fractional coordinates, crystallographic parameters and space group retrieved from the Cambridge Structure Data (CSD) by using Mercury software.

Temperature-Resolved X-ray Powder Diffraction (TR-XRPD)

TR-XRPD diffraction data were collected using a D5005 diffractometer (Siemens-Bruker). The instrument is equipped with an X-ray tube containing a copper anticathode, (40 kV, 40 mA), and a kβ filter (Ni) and a TTK 450 heating stage (Anton Paar). The scan step was fixed at 0.04° with a counting time of 4s/step over an angular range 10°- 30°. Low temperatures (below 20 °C) were reached with the support of a Lauda RP890 cryostat. Samples were heated at a rate of 2 K/min between the measurements, and remained 45 minutes at every analyzing temperature.

In-situ X-Ray

In-situ X-ray diffraction data were collected using a prototype of diffractometer developed in SMS laboratory. This apparatus has an original goniometer with a reverse geometry (-θ/-θ). Its association with a dedicated reactor, with a bottom transparent to X-ray, allows *in-situ* analyses (Fig.A.2). The detector is a lynx eyes^{TM} (Bruker, Germany) and the beam comes from an X-ray tube with a copper anticathode. X-ray diffraction analyses were performed

with a step of 0.04° (2θ), with 0.5 s/step from 14 to 30° (2θ). The temperature range for each analysis relies between 12 °C and 46 °C (Fig.A.3).

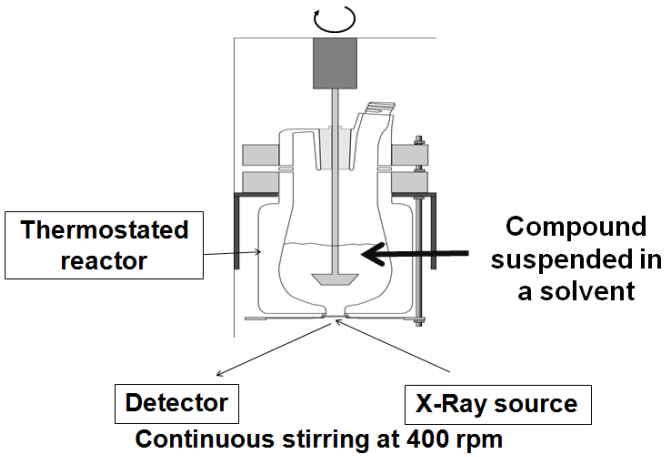

Figure.A.2 Principle of *in-situ* X-Ray

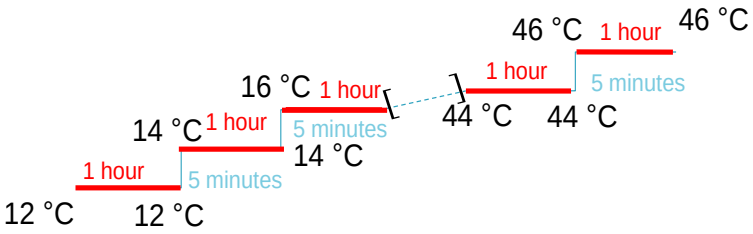

Figure.A.3 Temperature program for the *in-situ* X-Ray analyses

A.2 Differential Scanning Calorimetry (DSC)

DSC is a thermoanalytical technique used to measure characteristic properties of a sample such as fusion, glass transition, solid-solid transition and the enthalpies associated to these phenomena in function of temperature and time.

Two types of DSC exist:

a) Heat flux DSC: Two crucibles one containing the reference and the other the sample of known mass, are submitted to the same program of temperature variation under controlled atmosphere in the same furnace. The difference of thermal flux between both crucibles is measured with the support of thermocouples and it is proportional to the amount of heat absorbed or released by the sample per unit of time. These operations are monitored by a system that records the heat variations and thus allows

drawing the heat flux curve versus temperature and the enthalpies of the detected phenomena.

Heat flux DSC analyses were performed using a DSC 214 Polyma (Netzsch). Samples were weighed in 25 µL aluminum pans and a heating rate of 5 K/min was applied, under nitrogen atmosphere. Data treatment was performed by using Netzsch Proteus® software v6.1.

For the construction of binary phase diagrams, the onset temperatures were taken into account for the peaks of melting, transition, invariants. For the liquidus, the peak value was taken into account.

b) Power-compensated DSC: Sample and reference are placed in two independent identical furnaces where energy change of the sample is controlled, directly measured and reported. The temperature of the sample and reference are kept at the same value via independent heating. The amount of power required to maintain the system in equilibrium conditions is directly proportional to the energy changes occurring in the sample. Because of its direct measurement of the actual heat flow, the power-compensated DSC yields the most accurate and reproducible heat capacity measurements.

Thermal analyses were conducted in a power-compensated *Perkin Elmer PyrisDiamond DSC* equipped with a liquid nitrogen cooling system. Solid samples (mass of circa 4-6 mg) were placed in a 30µLpierced aluminum crucible. The atmosphere of the analyses was regulated by nitrogen flux (20 $mL.min^{-1}$), and heat runs were conducted at different constant heating rates. The data treatment was performed with Pyris-Thermal Analysis Software.

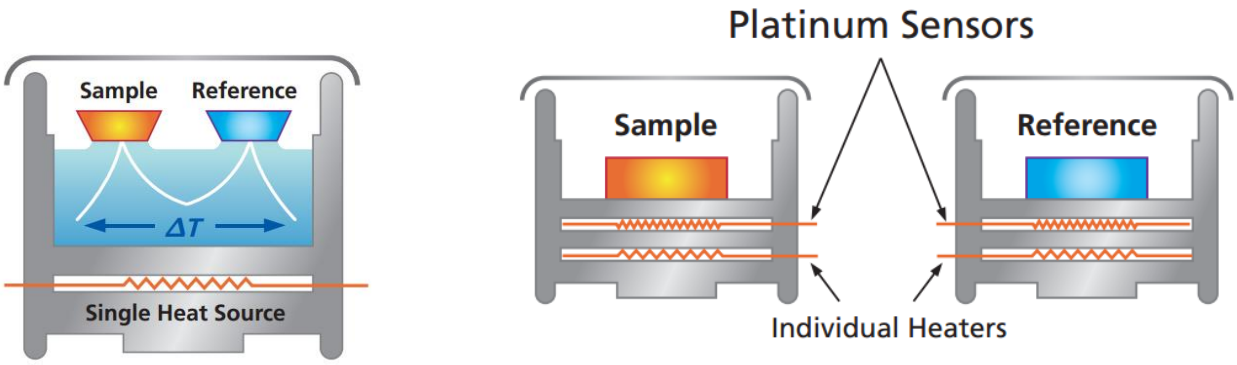

Figure.A.4 Schematic representation of a DSC flux (left) and power-compensated DSC(right)

A.3 Thermogravimetry

Thermogravimetric analysis (TGA) measures the mass evolution of a solid as function of the temperature. Desolvation phenomena were characterized by measuring the mass loss simultaneously with DSC analyses (TG-DSC) through a NETZSCH apparatus, STA 409 PC model.

A.4 Dynamic Vapour Sorption (DVS)

DVS apparatus is a device devoted to characterize the interactions between solids and surrounding vapor under isothermal conditions. This technique consists in varying the RH or solvent vapor surrounding the sample and following the change in mass of the sample with a microbalance at a fixed temperature. The partial vapor pressure is controlled by continuous gas flow containing pure nitrogen and solvent vapor in adequate proportions.

The mass versus RH exhibits a specific shape depending on phenomena such as: hygroscopicity, surface adsorption, deliquescence, crystallization of hydrate, etc.

The temperature and the partial vapor pressure are directly measured with a precision of +/- 0,5 °C and +/- 0,5% respectively. Mass variations are recorded continuously with a precision of 0.1 µg.

$$\frac{dm}{dt} \leq 2.10^{-4}\%.\min^{-1}$$

A range of $P_{solvent}/P_{sat}$ between 0% to 95% can be explored, step by step (for example: 10% RH steps) or in a continuous way (with a fixed rate for sorption or desorption). The mass variation and the partial pressure are measured automatically. In the stepped mode, the increment in $P_{solvent}/P_{sat}$ is driven by a mass evolution criterion (typically $dm/dt<5x10^{-4}\%.min^{-1}$during 10 minutes). Sorption/desorption isotherms could be plotted by taking into account the mass at the end of each step.

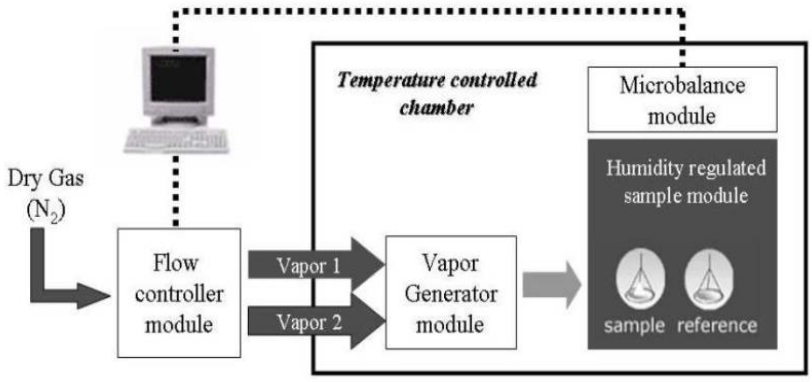

Figure.A.5 General scheme of a DVS apparatus.

A.5 Raman Spectroscopy

Raman is a spectroscopic technique used to observe vibrational, rotational, and other low-frequency modes in a system. The irradiation of a crystal by a monochromatic beam or laser, in the visible, near-infrared, or near ultraviolet range of the electromagnetic spectrum, results in scattering process that brings valuable information about the vibrational properties of the molecules. The fingerprint region of organic molecules is in the (wavenumber) range 500–2000 cm^{-1}. Raman spectroscopy yields important information related to the geometric structure of a molecule and its environment. Changes in crystal geometric structure will cause band shifts in the spectra. Besides, changes in symmetry with different crystal packing geometries will cause overall band splitting, coalescence, or relative intensity changes.

Raman analyses were carried out at ambient temperature by using a confocal Raman microscope (LabRam HR by Jobin-Yvon Horiba) coupled to an optical microscope (Model BX41, Olympus) *with xyz* mapping stage via optical fibers. The excitation of Raman scattering was operated by a He–Ne laser at a wavelength of 632.8nm. The laser beam was focused on the sample by a microscope objective X50 and the Raman signal was analyzed using a confocal pinhole of 300µm diameter and 600 lines per mm grating. The selected spectral lateral resolution was $4cm^{-1}$ for a spatial lateral resolution better than 2µm. The duration of the data collection was adjusted in order to minimize the background signal.

A.6 Scanning electron microscopy (SEM)

Scanning electron microscopy (SEM) pictures were obtained with a JEOL JCM-5000 NeoScope instrument (secondary scattering electron) at an accelerated voltage between 10 and 15 kV. Powder samples were stuck on an SEM stub with gloss carbon and coated with gold to reduce electric charges induced during analysis with a NeoCoater MP-19020NCTR.

A.7 Second Harmonic Generation (SHG)

When a high power laser interacts with a non-centrosymmetric material, it gives rise to a new wave at half the initial wavelength. This nonlinear optical process is called second harmonic generation (SHG). Note that SHG cannot occur in liquids, amorphous solids and centrosymmetric crystalline materials. Due to its high sensitivity to non-centrosymmetric crystalline materials, SHG has already been employed to monitor the formation of non-centrosymmetric crystals from an amorphous phase and from supersaturated solutions.Since several years,SMS laboratory has developed a versatile second harmonic generation set-up in order to monitor the intensity of the SHG signal versus temperature and humidity. The

temperature resolved set-up (TR-SHG) uses a heating/cooling stage coupled to the classical SHG set-up. This has been successfully used to track various types of solid-solid transitions. Figure A.6 shows the experimental setup used for TR-SHG measurements. A Nd:YAG Q-switched laser (Quantel) operating at 1.064μm was used to deliver up to 360 mJ pulses of 5 ns duration with a repetition rate of 10 Hz. An energy adjustment device made up of two polarizers (P) and a half-wave plate (λ/2) allowed the incident energy to be varied from 0 to ca. 200 mJ per pulse. A RG1000 filter was used after the energy adjustment device to remove light from laser flash lamps. The samples (in an open crucible) were placed in a computer-controlled heating−cooling stage (Linkam THMS-600) and were irradiated with the laser beam (4 mm in diameter). The signal generated by the sample (diffused green light 532 nm) was collected into an optical fiber (500 μm of core diameter) and directed onto the entrance slit of a spectrometer (Ocean Optics). A boxcar integrator allowed an average spectrum (spectral range 490−590 nm) with a resolution of 0.1 nm to be recorded over 3 s (30 pulses).

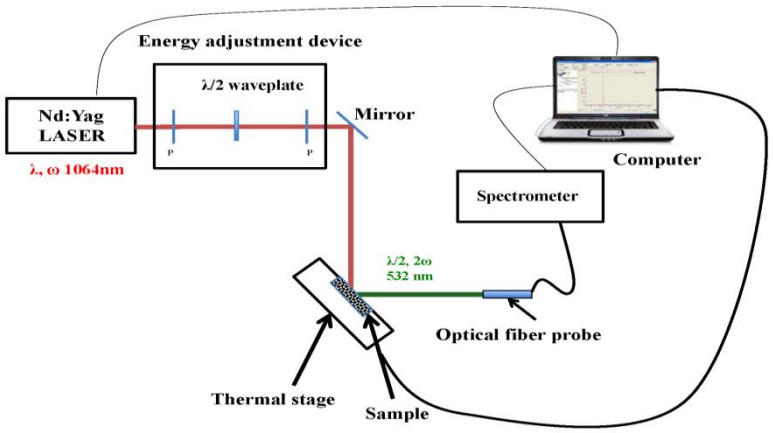

Figure A.6 Temperature-resolved second harmonic generation set-up.

Schematic evolution of the SHG signal vs. temperature in a binary eutectic system

The schematic evolution of the SHG signal in a binary eutectic mixture of two components (A and B) during the heating process is plotted in Figure A.7 (hypereutectic compositions) and Figure A.8 (hypoeutectic compositions). We assume that component A crystallizes in a centrosymmetric space group and that component B crystallizes in a non-centrosymmetric space group. In Figure A.7,during the heating process, the route1→2→3 is followed. From point 1 to point 2, the SHG signal remains stable. At point 2, a sharp decrease of the SHG signal occurs because of the appearance of the liquid phase (the scattering and/or the absorption which is due to the liquid phase, decreases the SHG signal), the corresponding temperature is the eutectic temperature (T_E). From point 2 to point 3, a progressive decrease of the SHG signal is observed, which is due to the progressive disappearance of crystals of

component B. Finally, at point3, the SHG signal vanishes, which means that there is no more non-centrosymmetric crystals. Thus, the liquidus temperature (T_L) is reached.

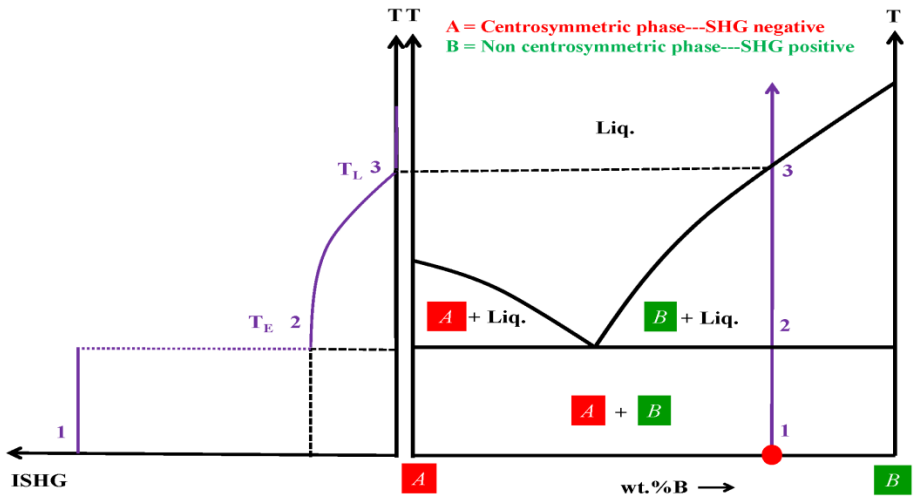

Figure A.7 Basic schematic of the SHG signal evolution for hypereutectic compositions.

The same assumptions are valid for hypoeutectic compositions (Fig. A.8). From point 1 to point 2, the SHG signal remains stable. After a sharp decrease of the SHG signal at the eutectic temperature (point 2), the signal totally vanishes, because the system is only composed of centrosymmetric phases (crystals of A) and liquid.

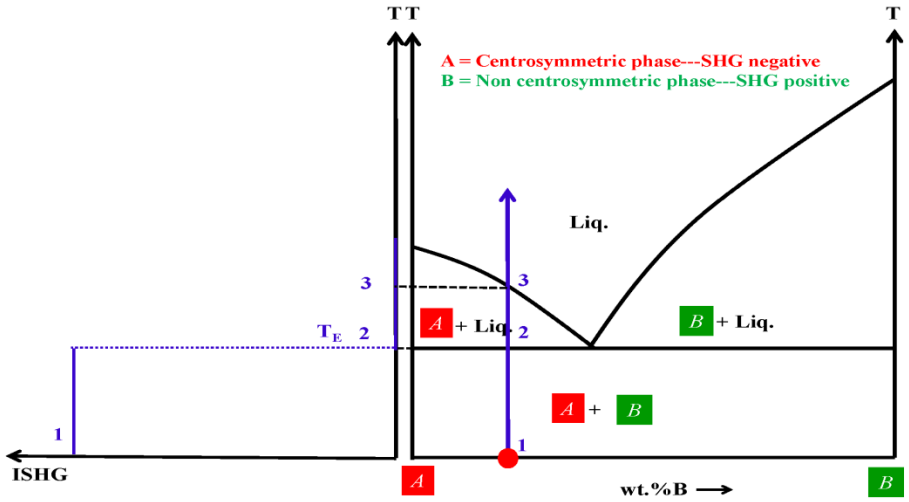

Fig.A.8 Basic schematic of the SHG signal evolution for the hypoeutectic compositions.

B.1 Nuclear Magnetic Resonance Spectroscopy

Solution ^{1}H NMR spectroscopy experiments were carried out with deuterated solvents d_6-DMSO on a Bruker spectrospin (300 MHz) apparatus. Data processing was performed with the ACD/NMR processor software.

B.2 Determination of water by Karl Fischer

Karl Fischer is designed to determine water content in substances, utilizing the quantitative reaction of water with iodine and sulfur dioxide in the presence of a lower alcohol such as methanol and an organic base such as pyridine, as shown in the following formulae:

$$H_2O + I_2 + SO_2 + 3\ C_5H_5N \rightarrow 2(C_5H_5N{+}H)I^- + C_5H_5N{\cdot}SO_3$$

$$C_5H_5N{\cdot}SO_3 + CH_3OH \rightarrow (C_5H_5N{+}H)OSO_2{\cdot}OCH_3.$$

In the coulometric titration method, iodine is produced by electrolysis of the reagent containing iodide ion, and then, the water content in a sample is determined by measuring the quantity of electricity which is required for the electrolysis (*e.g* for the production of iodine), based on the quantitative reaction of the generated iodine with water.

The popularity of the Karl Fischer titration is due in large part to several practical advantages that it holds over other methods of moisture determination, including: High accuracy and precision, small sample quantities required, easy sample preparation and short analysis duration.

Tests were performed with 899 coulometer Karl Fischer Metrohm able to measure 10 µg to 200 mg absolute water.

C. Determination of the fusion enthalpies of Form I and II of N-methylurea (NMU)

Melt-quenching of the commercial NMU was run inside a DSC crucible with the support of a flux-DSC apparatus.

During the first heating of the commercial batch, an endothermic peak at T_{onset} = 98 °C is detected and it is assigned to the fusion of the stable Form I with an enthalpy of fusion ΔH_F^I = 188.5 J/g .

The sample was then cooled down to -50 °C with a cooling rate at 20K/min. The cooling DSC thermogram is not reported in Figure C1.

Upon the second heating, the DSC thermogram illustrates an endothermic peak at T_{onset} = 95.2 °C corresponding to the fusion of Form II with an enthalpy of fusion ΔH_F^{II} = 166.6 J/g.

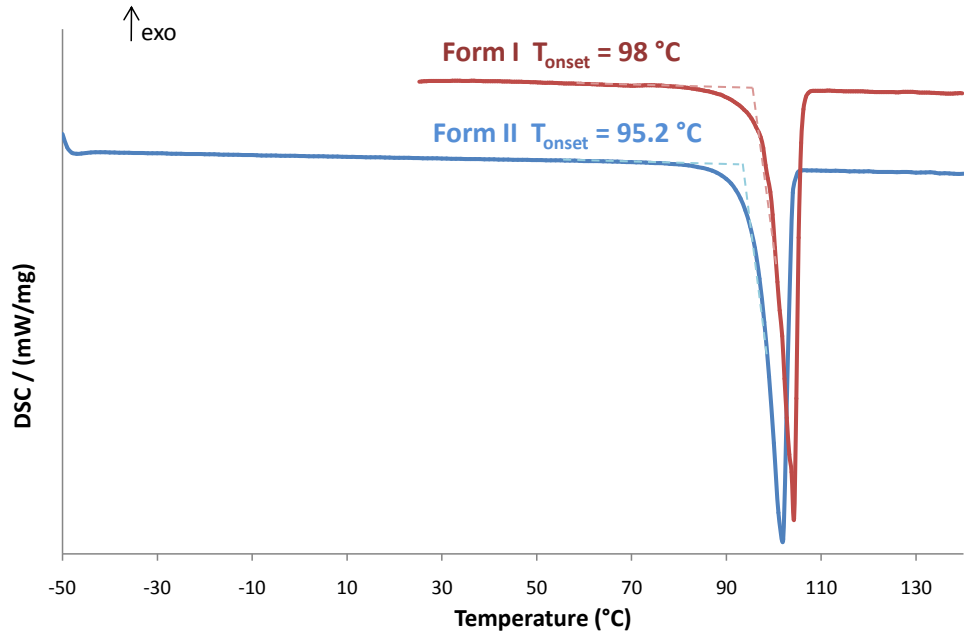

Figure.C1 Heat Flux DSC curves of the commercial NMU upon the first heating (upper curve in red) and the second heating (lower curve in blue)

D. Atomic coordinates and isotropic displacement parameters for Form I, II and III of NMU.

Note: The data reported representing the atomic coordinates of NMU Form I, are retrieved from the Crystallographic Information File (CIF) from the Cambridge Crystallographic Data Centre CCDC from the refcode: MEUREA.

Form I	x	y	z
C1	0.3305	-0.1949	0.4727
C2	0.3476	-0.3465	0.1571
N1	0.3982	-0.1704	0.6459
N2	0.4087	-0.3036	0.3460
O1	0.2000	-0.1216	0.4337
H1	0.3530	-0.0860	0.7270
H2	0.4890	-0.2180	0.6660
H3	0.4190	-0.4080	0.0790
H4	0.2690	-0.4530	0.1700
H5	0.2980	-0.2470	0.0920
H6	0.4940	-0.3440	0.3840

Form II	x	y	z	U iso
C1	0.6756(12)	0.5251(8)	0.1595(5)	0.05000
C2	0.6887(11)	0.2109(12)	0.0603(7)	0.05000
N1	0.8270(13)	0.6830(10)	0.1970(8)	0.05000
N2	0.8249(12)	0.3850(9)	0.1074(5)	0.05000
O1	0.4081(12)	0.5122(8)	0.1717(5)	0.05000
H1	0.7336(13)	0.7701(12)	0.2389(10)	0.05000
H2	1.0099(13)	0.6844(10)	0.1898(8)	0.05000
H3	0.8187(11)	0.1179(13)	0.0350(9)	0.05000
H4	0.6006(11)	0.2546(18)	-0.0074(6)	0.05000
H5	0.5438(11)	0.1477(10)	0.0981(8)	0.05000
H6	0.9997(12)	0.4055(8)	0.1042(4)	0.05000

Form III	x	y	z	U iso
C1	0.3213(9)	0.5415(4)	0.6525(2)	0.05000
C2	0.2859(13)	0.8151(5)	0.5330(5)	0.05000
N1	0.1859(12)	0.4059(5)	0.7012(4)	0.05000
N2	0.1762(9)	0.6709(5)	0.5934(3)	0.05000
O1	0.5885(8)	0.5506(5)	0.6629(3)	0.05000
H1	0.2803(15)	0.3191(6)	0.7508(5)	0.05000
H2	-0.0155(12)	0.4020(7)	0.6950(4)	0.05000
H3	0.1473(16)	0.9135(6)	0.5054(6)	0.05000
H4	0.3632(14)	0.7835(7)	0.4452(4)	0.05000
H5	0.4536(14)	0.8812(5)	0.5819(6)	0.05000
H6	-0.0236(9)	0.6520(7)	0.5921(3)	0.05000

E. Crystal data of the heterosolvate Olanzapine: Pinacolone:Water

Chemical formula	**[$C_{17}H_{20}N_4S$] 1.5H_2O and undefined residual electronic density**
Space group	***P*2₁/c**
System	**Monoclinic**
***a*/Å**	**14.48**
***b*/Å**	**12.57**
***c*/Å**	**14.65**
***β*/°**	**110.1**
Unit cell volume/Å³	**2506.8**
R (%)	**12**